BIOMEDICAL IMAGE RESOLUTION IMPROVEMENTS BY COMBINED USE OF FOCAL MODULATION, PUPIL ENGINEERING, AND SPARSITY PRIORS

DUAN YUBO

(B. Eng. & M. Eng., Tsinghua University, China)

A THESIS SUBMITTED

FOR THE DEGREE OF DOCTOR OF PHILOSIPHY
OF ENGINEER

DEPARTMENT OF BIOMEDICAL ENGINEERING

NATIONAL UNIVERSITY OF SINGAPORE

2014

Declaration

I hereby declare that the thesis is my original work and it has been written by me in its entirety. I have duly acknowledged all the sources of information which have been used in the thesis.

This thesis has also not been submitted for any degree in any university previously.

Duan Yubo.

Duan Yubo

20 August, 2014

Acknowledgement

I would like to express my heartfelt gratitude to my supervisor Assoc. Prof. Chen Nanguang for his supervision and guidance in my research work. He made me understand that achievement comes from rigorous attitude, appropriate methodology and hardworking. Without his invaluable suggestions, constant support and encouragement, the progress of my PhD research would not have been possible.

I would also like to express my sincere appreciation to my co-supervisor Prof. George Barbastathis for his generous support and professional guidance. I enjoyed every discussion with him and learned a lot from his challenging questions and invaluable advices. His passion in research and profound knowledge have left a lasting impression on me.

My special gratitude goes to Prof. Colin J. R. Sheppard for his precious guidance throughout my research and his supervision in first half of my postgraduate study. He is always willing to find time to discuss and solve problems with us, patiently and actively, with an amazing ability in answering the most primitive questions with clarity and simplicity. I benefited tremendously from the discussions with him. I believe and appreciate that Prof. Sheppard has an extraordinary impact on my research career.

Another mentor who played a significant role in my research is Dr. Zhang Baile. I acknowledge him for not only introducing me to the field and guiding me generously and professionally, but also for his enthusiasm and creativity that always inspires me along the research journey.

I am grateful to Dr. Shakil Rehman for helpful discussions on my research and professional guidance on optical experiments. Without his help, I could not perform the experiment of modulation depth measurement smoothly. I also acknowledge Dr. Diao Yingying for her useful suggestions and valuable help on the experiment of focal

modulation microscopy. I would like to appreciate Dr. Dipanjan Bhattacharya, Dr. Vijay Raj Singh and Dushan Wadduwage for helpful discussions on DSLM and HiLo microscopies and sharing experimental data for my algorithm verification.

I would like to acknowledge the members at the Optical Bioimaging Laboratory and the 3D Optical Systems Group for their help throughout my postgraduate life. I would like to thank Zhang Zhengyun and Chen Wensheng for their insightful discussions on compressive sensing; Chen Zhi for helpful suggestions on experiments; Gao Guangjun and Shilpa Pant for useful discussions on focal modulation microscopy; Luo Yuan for his helps in both research and career advices; Si Ke and Gong Wei for their helps on pupil engineering. I also enjoyed and feel grateful for the opportunities to learn other optical imaging techniques from Zhang Pengfei, Kalpesh Mehta, Zaineb Taqi, Ali Hasnain, Zhou Xiaowei, Zhang Qiang, Chen Ling, Koushik Nundy, Naveen Balla, Shalin Mehta, Gao Hanhong, Tian Lei, Liu Yi, Hoang Xuan, Huang Yuanhao, Xu Hongyi, Max Hsieh, Zhu Yunhui, Johnny Choi, Jeong-Gil Kim, Kelli Xu, Justin Lee, Jason Ku, Jon Petruccelli, Adam Pan and Nikhil Vadhavkar.

I would like to acknowledge the financial support from the National Research Foundation Singapore through the Singapore MIT Alliance for Research and Technology's BioSystems and Micromechanics Inter-Disciplinary Research.

Finally, I would like to express my deepest heartfelt gratitude to my parents. Without their support and sacrifice, I would not be able to pursue my doctoral degree and reach the place where I am now. My appreciation also goes to my parents-in-law and my brother who always support me in my life.

The thesis is dedicated to my beloved wife, who always stands with me and supports me whatever how tough the life is. Her love gives me endless energy to take on the endeavor of pursuing our dream.

Contents

Summary

It is challenging to acquire three-dimensional images of high resolution deep inside biological tissues, where the resolution is mainly restricted by out-of-focus background, multiple scattering and short noise. In this thesis, we apply focal modulation, computational imaging and hybrid schemes to develop new microscopic techniques to reject background, scattering and noise.

In the first part of the thesis, three new approaches of aperture optimization for focal modulation microscopy (FMM) are introduced to improve the modulation depth and hence to enhance scattering rejection. These approaches, based on the concept of pupil moment, are applicable to scalar and vector diffraction cases and nonuniform illumination. Among them, the analytical approach 'maximally-flat crater' (MFC) could achieve a modulation depth with a small difference less than 3% of the maximal value. MFC was then extended to design apertures for light of circular and radial polarizations, and azimuthal polarization encoded by spiral phase (AziSpi). With proper apodization on the aperture, the resolution and modulation depth for radial polarization and AziSpi were simultaneously improved.

Second, diverse imaging with sparsity priors was investigated in structured illumination microscopic imaging system. By rearranging photons to their emission origins, diverse imaging outperforms conventional image reconstruction approaches in background rejection and resolution improvement. The sparsity prior, total variation (TV) regularization, enhances its performance in axial sectioning and noise elimination. We found that the reconstruction fidelity degrades as the contrast or the spatial frequency of the structured illumination pattern decrease, because there are less high frequency components introduced as compensation for the 'missing cone'.

Third, to obtain high-speed image acquisition with sectioning capability, hybrid imaging modalities combining FMM and wide-field microscopy were introduced to implement in spatial domain, in Fourier domain and in sequence for different scenarios. The diverse scheme was borrowed to hybrid image reconstruction in spatial domain, in which the fast-scanning FMM provides sectioning information and wide-field imaging offers signal strength. Rather than iterative reconstruction, the Fourier hybrid modality directly recovers the image by combining Fourier components of undersampled FMM images with sectioning information and wide-field images with high resolution. The sequential hybrid scheme first explores the point spread function (PSF) from FMM and wide-field images in a small volume, and then reconstruct the whole volume of interest from wide-field images.

In addition, a theoretical model of direct imaging process through a micro-lens was established with vectorial electromagnetic analysis. The simulation results show that the resolution of a spherical micro-lens with visible light illumination is between 100nm and 150nm measured with two-point resolution criterion, which is beyond the diffraction limit. However, the significant side-lobes may cause poor contrast and even artifacts in wide-field imaging mode.

List of Publications

Journal Papers

1. **Y. Duan**, G. Barbastathis, and B. Zhang, "Classical imaging theory of a microlens with super-resolution," Opt. Lett. 38, 2988-2990 (2013).

2. Y. Luo, B. Zhang, T. Han, Z. Chen, **Y. Duan**, C.-W. Chu, G. Barbastathis, and C. W. Qiu, "Phase-preserved optical elevator," Opt. Express 21, 6650-6657 (2013).

3. **Y. Duan**, C. J. R. Sheppard, S. Rehman, and N. Chen, "Analytic method to optimize aperture design in focal modulation microscopy," Opt. Lett. 39, 1677-1680 (2014).

Conference Papers

1. **Y. Duan**, S. Rehman, G. Barbastathis, N. Chen, “Aperture Optimization to Improve Modulation Depth in Focal Modulation Microscopy”, Focus on Microscopy 2013, 24-27 March 2013, Maastricht, The Netherlands

2. **Y. Duan**, S. Rehman, G. Barbastathis, N. Chen, “An Analytic Method to Optimize Aperture Design in Focal Modulation Microscopy”, The 15th International Conference on Biomedical Engineering (ICBME 2013), 4-7 Dec 2013, Singapore

3. **Y. Duan**, S. Rehman, G. Barbastathis, N. Chen, "Aperture design in focal modulation microscopy to improve modulation depth", SPIE BiOS| SPIE Photonics West, 1-6 Feb 2014, San Francicso

4. **Y. Duan**, S. Rehman, G. Barbastathis, N. Chen, “FMM-guided 3D image reconstruction using compressive sensing”, Focus on Microscopy, FOM 2014, Sydney, Australia, 13-16 April 2014.

5. **Y. Duan**, C. Sheppard, S. Rehman, G. Barbastathis, N. Chen, “Performance of cylindrically polarized light in focal modulation microscopy”, Focus on Microscopy, FOM 2014, Sydney, Australia, 13-16 April 2014.

6. S. Rehman, **Y. Duan**, W. Chen, G. Barbastathis, “Compressive sensing approach to reconstruct HiLo images”, Focus on Microscopy, FOM 2014, Sydney, Australia, 13-16 April 2014.

List of Figures

List of Abbreviations

1D	One-dimensional
2D	Two-dimensional
3D	Three-dimensional
APSF	Amplitude point spread function
AziSpi	Azimuthally polarized light encoding by spiral phase
CGD	Conjugate gradient descent
CM	Confocal microscopy
CS	Compressive sensing / compressed sensing
DSLM	Digital scanned laser sheet microscopy
FMM	Focal modulation microscopy
GA	Genetic algorithm
LSFM	Light sheet fluorescence microscopy
MPM	Multi-photon microscopy
MSE	Mean square error
NA	Numerical aperture
OCM	Optical coherence microscopy
OTF	Optical transfer function
PALM	Photo-activated localization microscopy
PSF	Point spread function
SIM	Structured illumination microscopy
SLM	Spatial light modulator
SNR	Signal-to-noise ratio
SPIM	Selective plane illumination microscopy
STED	Stimulated emission depletion microscopy
STORM	Stochastic optical reconstruction microscopy
STPM	Spatiotemporal phase modulator
TPM	Two-photon microscopy
TV	Total variation
WF	Wide-field
ZPM	Zeroth pupil moment

Chapter 1

Introduction

1.1 Background

Optical imaging is a powerful technology in biomedical research, since it has the ability to capture cellular structural and functional information. Various concepts and techniques have been developed to improve the spatial resolution and/or penetration depth, e.g. confocal microscopy (CM) [1, 2], multi-photon microscopy (MPM) [3, 4], optical coherence microscopy (OCM) [5], and most recently, light sheet fluorescence microscopy (LSFM) [6, 7], structured illumination microscopy (SIM) [8, 9], stimulated emission depletion (STED) microscopy [10, 11], stochastic optical reconstruction microscopy (STORM) [12, 13] and Photo-activated localization microscopy (PALM) [14]. With these advanced techniques, image acquisition with subcellular resolution, or even molecular resolution by STED, STORM and PALM, can be acquired in biological tissues and cells.

However, it is still challenging to acquire dynamic three-dimensional (3D) images of high resolution deep inside biological tissues, where rather than diffraction limit the resolution is mainly restricted by out-of-focus background, multiple scattering and short noise [15-17]. Thus, to maintain a resolution in imaging thick specimen as high as in imaging thin samples in real-time, it is of significant importance to develop new dynamic microscopic techniques to reject background, scattering and noise.

Among various techniques mentioned before, CM is a well-established tool with background rejection, and has been widely used in biomedical research and diagnosis. However, CM becomes less effective when probing deeper inside scattering samples, i.e. beyond a few tens of microns, due to multiple scattering [16, 18]. By combining CM and angular gating mechanism, focal modulation microscopy (FMM) was recently introduced as a novel method for *in vivo* imaging of thick biological tissues [19, 20]. Pupil engineering technique is adopted in this thesis to further improve the performance of FMM, including both penetration depth and resolution.

CM and FMM generally require temporal and spatial scanning which will take a long time, so they are not very suitable for dynamic real-time imaging. Based on wide-field microscopy which only requires scanning in axial direction, SIM [9] and HiLo microscopy [21] apply structured illumination to obtain sectioning capability and thus reject out-of-focus and scattering background. To utilize the out-of-focus photons more effectively, diverse imaging [22] is studied in this thesis to reassign these photons to their origins. Since iterative reconstruction is used in diverse imaging, it is expected to reduce image noise by applying proper regularization. The regularization of sparsity priors, which has been successfully used in compressive sensing to reconstruct an optimal image from incomplete data [23], is investigated in this thesis.

On the other hand, advantages of different imaging systems may be extracted by hybrid imaging, where the sample is measured by more than one systems and then the image is reconstructed by combining different information from these measurements. For example, in medical imaging, MRI, CT, PET and SPECT can be combined to reveal multiple functional and structural information in a single image [24-26]. Hybrid imaging with FMM and wide-field microscopy is studied and presented in this thesis.

The subsequent sections provide an overview of relevant optical imaging techniques with sectioning capability, scattering reduction, and sparsity priors in image reconstruction. As most microscopies used in biomedical research are based on incoherent (e.g. fluorescence) imaging, this thesis focuses on incoherent imaging systems and all the discussions are under incoherent category if not specified.

1.2 Optical sectioning imaging

Conventional wide-field optical microscopy has no depth sectioning capability due to lack of axial high frequency components in the 3D optical transfer function (OTF). The wide-field OTF is given by autocorrelation of the 3D generalized pupil which is nonzero only on a spherical cap, so the OTF exhibits a ‘missing cone’ of spatial frequencies in axial direction (Figure 1.1 (a)) [1]. Thus, a stack of wide-field images is not real 3D image but every slice contains out-of-focus background.

CM applies selectivity ability of the pinhole to acquire sectioning capability. The pinhole before the detector allows the light from focus to transmit but blocks the light which comes from out-of-focus region. The OTF of CM is given by autocorrelation of the OTFs of illumination and collection [1], so it covers the whole 3D region within the bandwidth (Figure 1.1 (c)) and thus obtains sectioning capability. In principle, the resolution of CM is also improved because of extended bandwidth, but in practice the resolution is little improved due to finite size of pinhole [27]. The pinhole must be large enough to collect enough photons. Another advantage of pinhole is that it also rejects some scattered light, although the rejection ability becomes less effective for multiple scattering in imaging deeper inside scattering samples.

MPM acquires sectioning capability relying on nonlinear interaction in the sample, where the nonlinear multi-photon excitation is mostly confined in the focal region but decays rapidly out of focus [28, 29]. This nonlinear process results in sharper point spread function (PSF) of the emission light, e.g. the square of the incident PSF with scaled wavelength in two-photon microscopy (TPM), and thus an OTF occupies the complete region within the bandwidth [30]. Sheppard [31] discussed the general principle of this nonlinear interaction and proposed specific examples, including two-photon fluorescence, harmonic generation and coherent Raman scattering, that could be used in sectioning imaging. In addition, near infra-red light is usually used as excitation in MPM, which penetrates deeper inside biological samples than visible light. Moreover, nonlinear excitation caused by scattered photons is much weaker in out-of-focus region than linear excitation in single-photon microscopy. All these advantages make MPM superior to conventional CM in imaging depth. Nevertheless, the expensive pulse laser source required in MPM limits its widespread application.

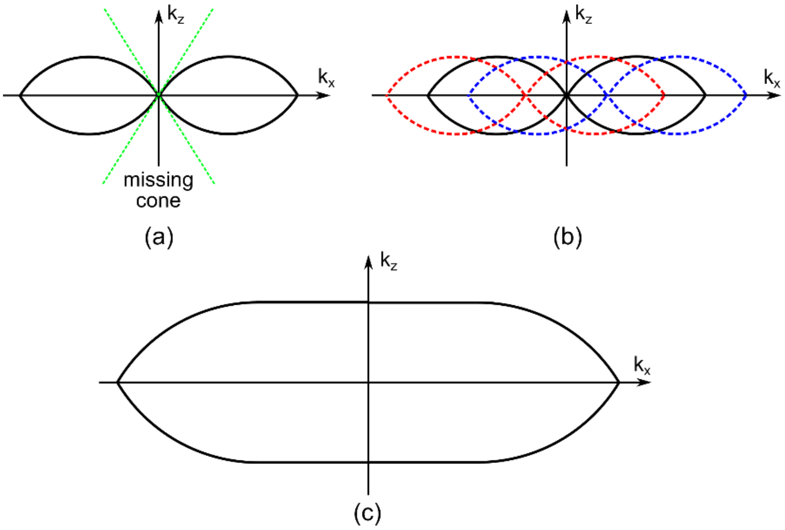

Figure 1.1 (a) OTF of wide-field imaging, where the green dashed lines show the region of ‘missing cone’. (b) OTF for SIM using two illumination beams. (c) OTF for CM.

From the point view of OTF in frequency domain, the sectioning capability can be obtained as long as the spatial frequency in the ‘missing cone’ is compensated. SIM employs spatially structured illumination light to shift the spatial frequency components of the sample away from its origin in image acquisition process, and then numerically shift it back in image reconstruction [9, 32]. As shown in Figure 1.1 (b), this manipulation not only compensates for the ‘missing cone’, but also extends the bandwidth of the final OTF and thus improves resolution. Various combinations of structured illumination have be implemented to improve the resolution in 2D or 3D [8, 9, 33-35], and commercial version of SIM, e.g. ZEISS ApoTome, is also available. SIM requires many images using different structured illumination patterns with precise phase shifts to extend the 3D OTF and thus to improve resolution. On the other hand, several groups developed simple approaches to apply less number of images using structured illumination to only obtain sectioning capability rather than resolution improvement. Wilson and associates applied structured illumination patterns with three different phases corresponding to relative phase shifts of 0 and $\pm\pi/3$ to extract the sectioning components by subtraction of the corresponding images in pair [36, 37]. Mertz and associates proposed a new approach using only one uniform and one structured illumination for each imaging plane [21, 38]. The image was reconstructed by extracting the in-focus high frequency components (named ‘Hi’) from the image with uniform illumination, and the in-focus low frequency components (named ‘Lo’) from the image with structured illumination. The principle of HiLo sectioning microscopy is also applicable to speckle illumination [39, 40], and speckle HiLo fluorescence endomicroscopy has also been developed [41]. However, rejection of out-of-focus light is not an efficient way to utilize collected photons, so we explored a new reconstruction approach to use these photons to enhance intensity and contrast.

LSFM, also termed as selective plane illumination microscopy (SPIM) [6] and digital scanned laser sheet microscopy (DSLM) [7, 42], is another promising wide-field sectioning microscopy for imaging over long time with high speed. Different from conventional microscopes, the camera in LSFM is oriented perpendicular to the illumination plane, which provides the optical sectioning capability because of finite thickness of the plane illumination. The sectioning of LSFM is an angular gating mechanism, which was first used in an ultramicroscope developed by Zsigmondy and Siedentopf in 1902 [43]. In angular gating scheme, the illumination light path is different from the collection light path, so only the particles located in the both paths (termed ‘confocal region’ in [44]) can be detected. Other geometric schemes of angular gating include divided aperture [44, 45], annular aperture [46, 47], tilted axes [48] and dual-axis [49-51]. Among all these techniques, LSFM has the highest output and remarkably reduced photobleaching and phototoxic effects. However, the sectioning capability of LSFM is limited by relatively thick light sheet illumination. Recently, the combination of LSFM and HiLo has been demonstrated to improve the sectioning capability [21, 42]. However, the out-of-focus photons are not efficiently used in this approach, the same as in conventional HiLo microscopy.

1.3 Focal modulation imaging

The concept of focal modulation can be considered as an extension of pupil engineering, where the effective focal intensity results from two corresponding pupils in focal modulation, while only one engineered pupil is used in conventional pupil engineering.

Pupil engineering has been extensively investigated in imaging to improve the resolution and/or focal depth. As Toraldo pointed out in 1952 [52], arbitrary sub-wavelength localization of light in the far-field could be achieved by a well-designed pupil filter, a phenomenon that was recently named as super-oscillation [53, 54]. Thus, the resolution could be improved with a narrower focal spot produced by a proper engineered pupil. Sheppard introduced the concept of pupil moment and series expansion method to relax the optimization process of both phase and amplitude pupil filters [55], thoroughly investigated the performance of two-zone and three-zone pupil filters [56, 57], and extended the method to linearly polarized and radially polarized illuminations [56, 58, 59]. Later, the expansion method was generalized to design complex pupil filters [60] for transverse super-resolution [61, 62], 3D super-resolution [63], and even generalized for the region out of the focal plane [64]. Dorn and colleagues adopted radially polarized illumination in an engineered pupil to create a focal spot sharper than that of a linear polarization [65, 66]. Azimuthal polarization encoded by a spiral phase pupil filter was also proposed to create a sharper focus [67]. Nevertheless, the focal spot is only moderately narrower as compared to the earlier mentioned pupil filters. To the best of our knowledge, these techniques cannot achieve a resolution as high as other super-resolution microscopies, e.g. STED. Most recently, Zheludev and associates applied super-oscillation and developed well-designed phase pupils [68] and amplitude pupils [69-71] to create a focal spot much smaller than diffraction limit, and achieved a resolution better than $\lambda/6$ [72], where λ is the wavelength of illumination. However, the inevitable giant side-lobes appeared in super-oscillation limits its application and even destroys the super-resolution [73]. On the other hand, engineered pupils can be employed to improve the depth of focus [74-76]. With well-designed binary phase pupil filters, both linearly polarized [77] and radially polarized [78] light can be used to create a long ‘needle beam’ with sub-diffraction beam size. Applications of pupil filters in microscopy to improve depth of field have been demonstrated [76, 79, 80].

Focal modulation usually applies subtraction of the focal intensities corresponding to two different pupils, normally one of which is free and the other is engineered. Depending on the specific design of the engineered pupil, the subtraction introduces several possible benefits: narrow PSF for resolution improvement, rejection of out-of-focus background for sectioning enhancement, and reduction of multiple scattering for deeper imaging depth.

In 1991, Hewlett and Wilson proposed and demonstrated the improvements of sectioning strength and resolution by subtracting two PSFs produced by different wavelengths or by different pinhole sizes [81]. Obviously the signal strength would be degraded by subtraction. To solve this drawback, the PSF to be subtracted could be specially engineered as a doughnut-shaped PSF which may be called a destructive PSF because of destructive interference occurring at the focus. A free pupil is usually used for the other PSF to obtain high signal strength (so called constructive PSF). Mertz and associates introduced wavefront aberration in the pupil to produce a destructive PSF in TPM [82, 83] in order to enhance background rejection. Isobe and associates applied two spatially scanned pulse beams to achieve constructive and destructive PSFs to reject background and improve resolution in nonlinear optical microscopy [84, 85].

This idea was later used by Sun to numerically implement on an oversampled image to improve resolution [86]. However, the scattering background in differential aberration or in spatial scanning cannot be completely eliminated because of inexactly equal scattering paths. Chen and Sheppard proposed focal modulation microscopy (FMM) to eliminate scattering background in CM, in which a temporal phase modulator was introduced to create constructive and destructive PSFs [19]. The modulation speed was remarkably enhanced by using acousto-optic modulators [87], or by the combination of electro-optic modulators and polarizers [20], which enables FMM for real-time image acquisition. In addition, the principle of PSF subtraction has been proposed to improve resolution of FMM [88] and CM [89, 90] by using properly engineered annular apertures.

Although the focal modulation technique enables resolution improvement and scattering rejection in FMM, the best performance of these two capabilities cannot be achieved at the same time in current FMM configuration. The side-lobes of the destructive PSF should be close to the focus to narrow the subtracted PSF in resolution improvement, while they should be far away from the focus to improve the modulation strength in scattering rejection. Thus, the effects must be properly balanced to meet the requirement of a specific application.

1.4 Sparsity priors in image reconstruction

Utility of sparsity priors has been well studied in compressive (or compressed) sensing (CS) to recover signals from incomplete dataset. In CS theory, the signals can be completely recovered from much fewer measurements than that required according to Nyquist-Shannon sampling theorem, if the signal has ‘sparse’ representation in a proper basis and the measurements are ‘incoherent’ [23, 91]. The sparse representation means only a few coefficients of the signal in a specific basis are nonzero. The incoherence requires that the information of the signal is evenly spread out in all measurements.

Thus, each measurement provides a sufficient mixture of modes of the signal. The nonzero modes of the signal mixed in the measurements can be retrieved by CS with sparsity priors, but not by conventional methods restricted under sampling theorem. Image reconstruction by CS has been successfully carried out in various imaging techniques, e.g. magnetic resonance imaging [92], single-pixel imaging [93], digital holography [94], phase tomography [95] and super-resolution microscopy [96].

Sparsity priors are also applicable to image reconstruction from plenty of measurements. The regularization of sparsity priors tends to explore the objective image in a way that restores the features represented sparsely. For example, total variation (TV) is significantly effective for recovering edges of images, which is widely used in images enhancement and noise suppression [97, 98]. TV was also applied in image deconvolution to reject the out-of-focus background in wide-field microscopy [99], CM [100] and the extended depth of field microscope [101]. TV reconstruction could recover 3D images from raw data with very low signal-to-noise ratio (SNR) [102], which is superior to other reconstruction methods. In this thesis, TV is applied in image reconstruction to improve the performance of diverse imaging.

1.5 Objective and structure of the thesis

The main goal of this thesis is to develop new dynamic microscopic techniques with capabilities of rejecting out-of-focus and scattering background and suppressing noise and thus enable 3D imaging deep inside biological samples with high resolution in real-time. Focal modulation microscopy (FMM), structured illumination imaging, wide-field microscopy and micro-lens are among the optical modalities for such studies, and image reconstruction with sparsity priors is the main computational modality explored in this research. This work includes the following specific objectives:

1) To develop novel optimization methods for phase aperture design in FMM to improve its background rejection and imaging depth.

2) To investigate the effects of different polarized illuminations in FMM to improve the imaging depth and resolution simultaneously.
3) To develop new image reconstruction approaches to enhance the sectioning and resolution of structured illumination imaging, and utilize the out-of-focus background photons more efficiently.
4) To study hybrid imaging by combining FMM and wide-field microscopy to obtain high-speed image acquisition without loss of optical sectioning.
5) To explore the mechanism of super-resolution phenomenon of a micro-lens for potential applications in biomedical imaging.

The structure of the thesis is given as follows.

With the concept of pupil moment, Chapter 2 introduces three methods to optimize design of annular apertures used in FMM. All the methods are demonstrated superior to previous approach, and are applicable to both scalar and vector diffraction cases and nonuniform illuminations. The effects of aberration on the modulation depth of FMM is also discussed.

Chapter 3 extends the illumination in FMM to cylindrically polarized light. First the expressions of field in focal region are derived. The application of circular polarization, radial polarization and azimuthal polarization with spiral phase are investigated in FMM. The effects of apodization for theses polarizations are studied.

Chapter 4 adopts diverse imaging approach with TV regularization to reconstruct structured illumination images. The effects of contrast and spatial frequency of the structured illumination pattern on the reconstruction fidelity are investigated. The resolution improvement of diverse imaging reconstruction is demonstrated.

To acquire advantages of FMM and wide-field microscopy simultaneously, Chapter 5 introduces hybrid imaging modalities manipulated in spatial domain, in Fourier domain and in sequence for different scenarios. Implementation methods and reconstruction fidelity of each approach are investigated.

Chapter 6 theoretically models the imaging process through a micro-lens with vectorial electromagnetic analysis, and then exclude the previously explanation of super-resolution that is based on the super-focusing effect.

Finally, conclusions and future work are summarized in Chapter 7.

Chapter 2

Aperture optimization in focal modulation microscopy

2.1 Introduction

Optical imaging into thick biological tissue with cellular or subcellular resolution is limited by scattering and absorption [103]. Besides light depletion, scattering also diffuses light, which distributes part of light out of focus and thus degrades image quality in the conventional wide-field microscopy. With the help of pinhole selectivity to block most of the out-of-focus photons, confocal microscopy (CM) has been successfully used in biological imaging, especially after the development of laser scanning CM. However, CM becomes less effective when probing deeper inside scattering samples, i.e. beyond a few tens of microns, as the multiple scattered photons leak through the pinhole, overwhelm the ballistic photons and thus deteriorate the imaging performance [16, 18]. On the other hand, multi-photon microscopy (MPM) has become a promising technique to image thick specimen at penetration depth of few hundreds microns with uncompromised spatial resolutions, since nonlinear multi-photon excitation is mostly confined in the focal region but decays rapidly out of focus [16, 28, 104]. Nevertheless, the expensive pulsed laser sources required in MPM limit its widespread application.

Combining CM with coherence gating mechanism, focal modulation microscopy (FMM) was recently developed as a novel method for *in vivo* imaging of thick biological tissues [19, 20]. FMM introduces a spatiotemporal phase modulator (STPM) into the illumination beam path to modulate part of the beam, which results in temporal oscillation of the interference pattern in the focal volume; whereas no oscillatory emission occurs in the out-of-focus region because of spatial separation between the modulated and unmodulated beams. Only the modulated emission light from the focal volume is retrieved to form FMM images, so out-of-focus and scattering background is effectively rejected. It has been demonstrated theoretically and experimentally that FMM can probe remarkably deeper than CM, especially when the imaging performance is restricted by strong multiple scattering [19, 105]. Moreover, FMM is compatible with two-photon microscopy to increase penetration depth further [106].

The most important component in FMM is the STPM, which determines the ability of background rejection and the efficiency of FMM signal generation. Although STPM may improve spatial resolution to some extent [88, 107, 108], modulation depth, which affects penetration depth and the threshold of excitation power, is of more concern in STPM design [109]. Gao *et al.* [109] compared modulation depth of annular, fan-shaped and stripe-shaped phase apertures in STPM, and found that annular phase aperture is superior to the others. The principle of equality of the areas for modulated and unmodulated sub-apertures was applied in their aperture design [109]. However, for an annular aperture in STPM, equal-area phase pattern cannot achieve totally destructive interference at the focal spot in imaging systems with high numerical aperture (NA) or non-uniform illumination. In fact, equal-area phase pattern is not the optimal design for uniform illumination. In this chapter, we propose new methods considering NA and illumination beam profile in the process of aperture design for STPM. Optimal apertures with both even and odd numbers of sub-apertures were obtained. In addition, the effect of aberrations on the performance of FMM was studied.

2.2 Principle of focal modulation microscopy

Based on a confocal microscope, FMM introduces a STPM to periodically modulate the phase of a spatial fraction of the excitation beam (Figure 2.1 (a)). Thus, the excitation field can be expressed as [110]

$$E(\mathbf{r},t) = E_1(\mathbf{r}) + E_2(\mathbf{r})\,\mathrm{e}^{i\varphi_f(t)}, \tag{2-1}$$

where **r** is the spatial coordinates, and the term $E_2(\mathbf{r})\,\mathrm{e}^{i\varphi_f(t)}$ describes the fraction of the beam with phase modulation at the frequency *f*. In a typical FMM system, the modulated and unmodulated beams are spatially separated in out-of-focus region by the STPM, so the excitation intensity is constant except in the focal region. The two beams overlap and interfere with one another at the focal point, and generate an oscillating intensity which is given by

$$\begin{aligned} I(\mathbf{r},t) &= \left|E(\mathbf{r},t)\right|^2 = E(\mathbf{r},t)\times E^*(\mathbf{r},t) \\ &= \left|E_1\right|^2 + \left|E_2\right|^2 + 2\left|E_1E_2^*\right|\cos\left[\varphi_f\left(t\right) + \arg(E_1E_2^*)\right], \end{aligned} \tag{2-2}$$

where the spatial coordinates **r** is omitted in the last equation. The first two terms in the last line of Eq. (2-2) are the portion of constant excitation intensity, while the last term corresponds to the periodically oscillated intensity at the modulation frequency *f*. The term $\varphi_f\left(t\right)$ describes the instantaneous relative phase shift of the two beams. When they are in phase, the maximal excitation intensity is reached,

$$I_{in-phase} = \left|E_1\right|^2 + \left|E_2\right|^2 + 2\left|E_1E_2^*\right|, \tag{2-3}$$

which is equivalent to the confocal excitation. The minimal excitation intensity is approximately reached when the two beams are in anti-phase,

$$I_{anti-phase} = \left|E_1\right|^2 + \left|E_2\right|^2 - 2\left|E_1E_2^*\right|. \tag{2-4}$$

The difference between the in-phase and anti-phase intensities is retrieved as the effective FMM excitation intensity. Note that modulation and demodulation are often used in experiments to retrieve FMM image [19, 20, 87, 111].

The STPM can be implemented by discrete mirrors controlled by piezoelectric actuators [19], acoustic-optical phase modulators [87] or a combination of electro-optic modulator and polarizer [20]. No matter what schematic is used in practice, we can model the STPM as a tunable phase aperture for simplicity as shown in Figure 2.1, where the modulated and unmodulated phase pattern of the aperture is of importance. For every tunable phase aperture considered in this thesis, all the phase-modulated sub-apertures have the same instantaneous phase. In other words, the phase-modulated sub-apertures are modulated simultaneously from the same initial phase. Theoretically, the phase of sub-apertures could be modulated in various ways. However, a complicated modulation mode is difficult to implement accurately and quickly in spite of possibly improved background rejection. To investigate the optimal configuration of the tunable phase aperture considered here, we can focus on only the in-phase and anti-phase status of the aperture because the effective FMM excitation intensity is determined by the difference between the two.

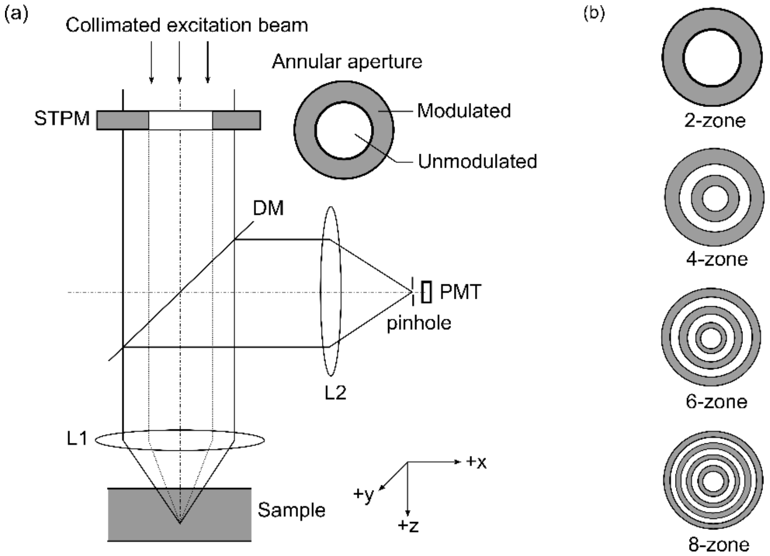

Figure 2.1 Schematic of FMM setup [110]. The annular phase aperture of 2 sub-apertures with (shaded region) and without (white region) phase modulation is applied. L1 and L2 are lenses with the same focal length. DM is dichroic mirror and PMT is photomultiplier tube. (b) Configuration of annular apertures with 2, 4, 6 and 8 sub-apertures. The shaded and white rings represent the sub-apertures with phase modulation and that without phase modulation.

2.3 Modulation depth

The modulation depth of FMM is defined as the ratio of the intensity of the modulated fluorescence signal (i.e., AC component) with respect to the average intensity (i.e., DC component) collected by the pinhole detector when exciting a uniformly fluorescence-stained sample [109]:

$$M = \frac{S_{AC}}{S_{DC}} = \frac{S_{\max} - S_{\min}}{S_{\max} + S_{\min}}. \tag{2-5}$$

Here S denotes the signal intensity at the pinhole detector, which can be expressed as:

$$S(t) = \iiint I(x,y,z,t) \times \left[\left| h_D(x,y,z) \right|^2 \otimes_2 D(x,y) \right] dxdydz, \tag{2-6}$$

where $I(x,y,z,t)$ is the excitation intensity, i.e. $I(\mathbf{r},t)$ in Eq. (2-2), $h_D(x,y,z)$ is the amplitude point spread function (APSF) of the detection optics, $D(x,y)$ is the sensitivity function for the detector and is restricted within the area of the pinhole, and $\otimes_2$ denotes the 2D convolution operation. In most cases, the signals $S_{\max}$ and $S_{\min}$ are reached corresponding to in-phase (Eq. (2-3)) and anti-phase (Eq. (2-4)) excitation intensities, respectively. To avoid the influence of sample structure in evaluating modulation depth, here the sample is assumed as uniform fluorescence material in the whole volume, and with equal emission and excitation wavelengths (if not specified) for simplicity.

Modulation depth is an essential parameter in designing FMM system as it determines the signal-to-noise ratio (SNR) and the efficiency of FMM signal generation. Here we mainly consider shot noise, the most important source of noise, which results from the statistical variation in the number of detected photons and is given by the square root of the variance [112]. Shot noise obeys a Poisson distribution, which has the property that its variance is equal to its mean. Thus, the importance of the modulation depth can be observed from the following relationship:

$$SNR \propto \frac{S_{AC}}{\sqrt{S_{DC}}} = M\sqrt{S_{DC}} \propto M\sqrt{IQ}, \tag{2-7}$$

where $\propto$ denotes that the former is proportional to the latter, I is the illumination intensity and Q is quantum efficiency. To maintain a certain level of SNR, the illumination intensity could be reduced to a quarter of the original intensity if the modulation depth doubles. Thus, we can decrease the illumination power if sufficient FMM signal is already obtained to form images of good quality, which is beneficial for avoiding photobleaching and phototoxicity in imaging living biological specimens.

According to Eqs. (2-5) and (2-6), the modulation depth is determined by the excitation intensity, detection optics and pinhole size. The detection optics is fixed for given excitation wavelength and NA. Normally the modulation depth decreases as the pinhole size increases [19], because the selectivity of pinhole degrades. However, the pinhole size must be big enough to collect enough emission photons. Usually the pinhole size is chosen comparable to the size of Airy disk. For given detection optics and pinhole size, the maximum and minimum signal intensities are approximately reached when the excitation intensities are maximum and minimum, respectively, where the later extreme values are obtained when the modulated and unmodulated beams are in-phase and anti-phase (also known as binary phase), respectively. Thus, we can substitute $S_{in-phase}$ and $S_{anti-phase}$ for $S_{\max}$ and $S_{\min}$, respectively, in Eq. (2-5). The modulation depth can be improved by optimizing the in-phase and anti-phase excitation intensities, which is relevant to aperture design of STPM in FMM. Theoretically, the aperture pattern can be designed complicated to improve the modulation depth. However, a complex pattern is difficult to manufacture accurately given that the aperture is so small (i.e. a diameter around a few millimeters) [109]. Therefore, in the following content, we focus on optimization of annular aperture with the number of sub-apertures from 2 to 8, where the aperture is phase-only if not specified.

In practical fluorescence imaging, the emission wavelength is normally longer than the excitation wavelength, so the APSF of the detection optics in Eq. (2-6) becomes broader than the assumption of equal emission and excitation wavelengths. The relative strength of the minimal signal $S_{\min}$ to the maximal signal $S_{\max}$ will increase since more energy in the side-lobes of the anti-phase excitation intensity are collected by the detection optics. Thus, the modulation depth will decrease, according to Eq. (2-5). One the other hand, the absolute signal strength will reduce as a broad detection optics makes more emission energy rejected by a given pinhole. Therefore, the SNR will also decrease. Nevertheless, the assumption of equal emission and excitation wavelengths will not affect the conclusions in this thesis as here we improve the aperture design to optimize the illumination (excitation) rather than the emission.

2.4 Annular aperture designed by zeroth pupil moment

It is apparent that the in-phase signal $S_{in-phase}$ is equivalent to the CM signal, which is the maximum detected signal for given illumination power. Thus, we need to minimize the anti-phase signal $S_{anti-phase}$ to improve the modulation depth (Eq. (2-5)). Although the equality of sub-apertures, that is, all the sub-apertures have equivalent areas and the numbers of modulated and unmodulated sub-apertures are the same (Figure 2.1 (b)), introduces destructive interference at the focal point for uniform illumination in low NA system [109], it does not guarantee destructive interference either for non-uniform illumination, e.g. Gaussian beam, or in high NA system. Here we introduce two methods, based on the concept of pupil moment, to achieve destructive interference at the focal point.

2.4.1 Equal zeroth pupil moment

Based on scalar diffraction theory, the field in the focal region can be described as [44]

$$E\left(v_x, v_y, u\right) = \frac{1}{\pi} \iint P\left(\rho_x, \rho_y\right) \exp\left[i\left(v_x\rho_x + v_y\rho_y\right) - iu\left(\rho_x^2 + \rho_y^2\right)/2\right] d\rho_x d\rho_y, \quad (2\text{-}8)$$

where $P\left(\rho_x, \rho_y\right)$ is the pupil function of the objective lens. The optical coordinates are defined through $v_x = kx\sin\alpha$, $v_y = ky\sin\alpha$, $u = 4kz\sin^2(\alpha/2)$, with *k* the wave number, *α* the angular semi-aperture of the objective lens, and *x*, *y*, *z* are Cartesian coordinates of the focal region. The coordinates ρ_x, ρ_y are normalized by the pupil radius on the pupil plane.

For an annular aperture with circularly symmetric pupil function, Eq. (2-8) can be written as [55]

$$\begin{aligned} E(v,u) &= 2\int_0^1 P(\rho) J_0(v\rho)\exp\left(-\frac{iu\rho^2}{2}\right)\rho d\rho \\ &= \int_0^1 P\left(\sqrt{m}\right) J_0\left(v\sqrt{m}\right)\exp\left(-\frac{ium}{2}\right)dm, \end{aligned} \tag{2-9}$$

where $\rho = \sqrt{\rho_x^2 + \rho_y^2}$, $v = \sqrt{v_x^2 + v_y^2}$, $m = \rho^2$, and J_0 is zeroth Bessel function of the first kind. The pupil function $P(\rho)$ includes the effects of the phase aperture and illumination beam profile $Q(\rho)$, e.g. Gaussian beam, and can be written as

$$P(\rho) = Q(\rho)T(\rho), \tag{2-10}$$

with $T(\rho)$ the transmission function of the phase aperture which can be described as

$$T(\rho) = \begin{cases} 1 & \text{in the unmodulated sub-apertures} \\ \exp\left[i\varphi_f(t)\right] & \text{in the modulated sub-apertures} \end{cases} \tag{2-11}$$

Obviously $T(\rho) = -1$ for binary phase status in the modulated sub-apertures.

The intensity at focal point is given by

$$I(0,0) = \left|E(0,0)\right|^2 = \left|\int_0^1 P\left(\sqrt{m}\right)dm\right|^2 = q_0^2, \tag{2-12}$$

where q_0 is the zeroth pupil moment. For a binary phase aperture with *n* sub-apertures ($n \geq 2$) and $n-1$ boundaries at m_1, m_2 ,…, m_{n-1}, the *p*-th pupil moment can be depicted as [55]

$$\begin{aligned} q_p &= \int_0^1 P(m) m^p dm \\ &= \frac{1}{p+1}\left[-2m_1^{p+1} + \ldots + 2(-1)^{n-1} m_{n-1}^{p+1} + (-1)^n\right], \end{aligned} \tag{2-13}$$

where uniform illumination is assumed. The pupil moment was introduced by Sheppard to describe the field as a series expansion for convenience [55]. For nonuniform illumination, e.g. Gaussian beam given by $Q(\rho) = \exp\left(-\rho^2/\sigma^2\right) = \exp\left(-m/\sigma^2\right)$, a modified pupil moment t_p can be defined as $t_p = \int_0^1 T(m) m^p dm$. Thus, the field can be expressed by the modified pupil moment through expanding the Bessel function and exponential function in Eq. (2-9) and the function of the Gaussian beam.

Eq. (2-12) shows that the destructive interference at the focal point can be achieved if the modulated and unmodulated sub-apertures have equal zeroth pupil moment (equal-ZPM) and the same number of sub-apertures. Since illumination beam profile has been considered in pupil moment, equal-ZPM is applicable for non-uniform illuminations, e.g. Gaussian beam. Furthermore, the principle of equal-ZPM can be extended to FMM systems with wavefront aberration by including the aberration in the pupil function, where the definition of the *p*-th pupil moment may be extended to 2D integral as

$$q_{p_x,p_y} = \iint P\left(\rho_x, \rho_y\right) \rho_x^{p_x} \rho_y^{p_y} d\rho_x d\rho_y. \tag{2-14}$$

The principle of equal-ZPM can be simplified to equal areas as in [109] for uniform illumination without aberration, i.e. $P\left(\rho_x, \rho_y\right) = 1$ for in-phase illumination.

Now we extend the principle of equal-ZPM to the FMM imaging system with a high NA objective lens. Considering a high NA system illuminated by a linearly polarized light in the Debye approximation, the electric field in the focal region at the point ρ, φ, z in cylindrical coordinates can be written as [59, 113]

$$\begin{aligned} E_x &= -iA\left(I_0 + I_2\cos 2\varphi\right) \\ E_y &= -iAI_2 \sin 2\varphi \\ E_z &= -2AI_1 \cos\varphi, \end{aligned} \tag{2-15}$$

$$I_n = \int_{-\infty}^{+\infty} P(c)\left(\frac{1-c}{1+c}\right)^{n/2} J_n\left(kr\sqrt{1-c^2}\right)\exp(ikzc)\mathrm{d}c,\ n = 0,1,2. \tag{2-16}$$

Here *A* is a constant coefficient related to wavelength and focal length. *P(c)* is the pupil function expressed as a function of $c = \cos\theta$, with θ the angle between the direction of the propagation of the illumination wave and the axis. *P(c)* includes the effects of the phase aperture and illumination beam profile *Q(c)*, and can be written as

$$P(c) = \sqrt{c}(1+c)Q(c)T(c), \tag{2-17}$$

where *T(c)* is the transmission function of the phase aperture which can be described as

$$T(c) = \begin{cases} 1 & \text{in the unmodulated sub-apertures} \\ \exp\left[i\varphi_f(t)\right] & \text{in the modulated sub-apertures} \end{cases} \tag{2-18}$$

From Eqs. (2-15) and (2-16), the field at the focal point is proportional to the zeroth pupil moment $I_0 = \int P(c)\mathrm{d}c$. Similar to the scalar diffraction case, here the *p*-th pupil moment is defined as [59]

$$q_p = \int P(c)\mathrm{c}^p \mathrm{d}c. \tag{2-19}$$

For a binary phase aperture with n sub-apertures ($n \geq 2$) and $n-1$ boundaries depicted by $c_1, c_2, \ldots, c_{n-1}$, the *p*-th pupil moment can be expressed explicitly as

$$q_p = \sum_{j=1}^{n}(-1)^j\left[\frac{1}{p+3/2}\left(c_j^{p+3/2} - c_{j-1}^{p+3/2}\right) + \frac{1}{p+5/2}\left(c_j^{p+5/2} - c_{j-1}^{p+5/2}\right)\right], \tag{2-20}$$

where a uniform illumination is assumed. The nonuniform illumination can be treated similar to scalar case by defining a modified pupil moment. Therefore, the destructive interference at the focal point can be achieved by the principle of equal-ZPM in the high NA FMM systems.

2.4.2 Zero-sum zeroth pupil moment

The equal-ZPM of each sub-aperture is a sufficient but not necessary condition to achieve destructive interference at the focal point. The destructive interference occurs when the summation of ZPM in the modulated sub-apertures is equal to that in the unmodulated regions. Considering the plus-minus sign in the calculation of pupil moment, the total ZPM vanishes in this case. Thus, this principle is called zero-sum ZPM. There are various radius configurations to achieve zero-sum ZPM for a given number of sub-apertures, so genetic algorithm (GA) and conjugate gradient descent (CGD) are employed to explore the optimal aperture configuration to maximize modulation depth.

Another advantage of the zero-sum ZPM is that the phase aperture with an odd number of sub-apertures can be designed, while only that with even number of sub-apertures is compatible based on the principles of equal-ZPM or equal areas.

2.4.3 Simulation results

Typical system parameters used in our simulation are the same as [109] for low NA optical system. The wavelength of the emission beam is 0.633 μm and is assumed the same as the excitation beam for simplicity. The illumination objective lens and the collection lens are identical and with the same NA of 0.55. The pinhole diameter is 0.8 μm, about 0.6 times of the diameter of the Airy disk. For high NA optical system, the NA and pinhole diameter are changed to 0.95 and 0.46μm, respectively. The pinhole diameter keeps the same ratio with respect to the Airy disk. Note that the APSF of the detection optics used in the low NA system is the same as Eq. (2-9), whereas in the high NA optical system the detection optics is determined by averaging all polarization directions [114, 115]:

$$\begin{aligned}\left|h_D(x,y,z)\right|^2 &= \frac{1}{2\pi}\int_0^{2\pi}\left(E_x^2+E_y^2+E_z^2\right)d\varphi \\ &= A^2\left(I_0^2+2I_1^2+I_2^2\right),\end{aligned} \qquad (2\text{-}21)$$

where the terms A, I_0, I_1 and I_2 are the same as in Eqs. (2-15) and (2-16). The Gaussian beam was chosen that the intensity at the edge is $1/e^2$ times of the peak intensity.

Figure 2.2 shows simulation results of the modulation depth of annular apertures designed by different methods, where the illumination is uniform if not specified. In the case of scalar diffraction (Figure 2.2 (a)), the apertures designed by equal-ZPM are superior to those designed by equal-area when the illumination is nonuniform. The modulation depth of equal-ZPM under Gaussian illumination is a little greater than that under uniform illumination, since the slightly broader illumination PSF under Gaussian illumination makes a little more energy in side-lobes rejected by the pinhole. Similar trends can be concluded in the case of vector diffraction (Figure 2.2 (b)). Obviously the method of equal-area is not suitable as its modulation depth is much less than the other design methods. Among all the methods, the zero-sum ZPM gives the maximal modulation depth, as expected.

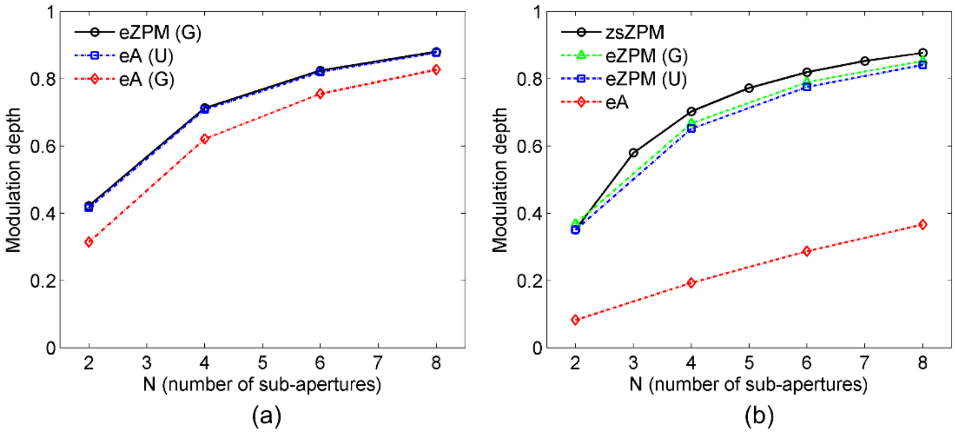

Figure 2.2 Modulation depth of apertures designed by equal-area (eA), equal-ZPM (eZPM) and zero-sum ZPM (zsZPM) using different numbers of sub-apertures with uniform (U) and Gaussian (G) illumination beams based on scalar (a) and vector (b) diffraction theories.

2.5 Aperture designed by maximally-flat crater (MFC)

For a given set of parameters, e.g. the number of sub-apertures, wavelength and NA, the maximum modulation depth can be obtained by the principle of zero-sum ZPM. However, the optimization algorithms, GA or CGD for example, are required and they are usually complicated and time consuming. Here, we propose a simple analytical method for aperture design to optimize the modulation depth. By direct algebraic manipulation, this approach is applicable to both scalar (low NA) and vector (high NA) diffraction optics.

Thanks to the selectivity of pinhole, the minimum signal $S_{\min}$ decreases if the intensity of the excitation beam $I\left(x, y, z, t_{anti-phase}\right)$ is pushed far away from the focal region of the detection optics $\left|h_D\left(x, y, z\right)\right|^2$ (Eq. (2-6)). This phenomenon is named as maximally-flat crater (MFC) because an extended flat intensity profile with minimum value in the focal volume is obtained. It seems similar to the maximally-flat response (MFR) introduced in [74], but the latter is broad and flat brightness only in axial axis and sharp in transverse axes; whereas the proposed MFC introduces a broad darkness in 3D focal volume.

2.5.1 MFC for scalar diffraction

We consider an annular aperture $P(\rho)$, $0 < \rho < 1$, containing n sub-apertures each with alternating transmissions of 1 and -1 in a low NA imaging system, which is the binary phase status of the pupil function in Eq. (2-10). The field in the focal region is expressed as in Eq. (2-9). For a aperture with n sub-apertures ($n \geq 2$) and $n-1$ boundaries at $m_1, m_2, \ldots, m_{n-1}$, the field can be expanded into a Taylor series with coefficients given by the pupil moment defined in Eq. (2-13). Thus, the excitation intensity in radial and axial axes can be expressed as Eqs. (2-22) and (2-23), respectively,

$$I(v) = \left|E(v,0)\right|^2 = \left|\sum_{p=0}^{\infty} \frac{(-1)^p}{(p!)^2 2^{2p}} q_p v^{2p}\right|^2 , \tag{2-22}$$

$$I(u) = \left|E(0,u)\right|^2 = \left|\sum_{p=0}^{\infty} \frac{(-i/2)^p}{p!} q_p u^p\right|^2 . \tag{2-23}$$

To determine the $n-1$ unknowns, m_1 , m_2 ,…, m_{n-1} , we equate to zero the coefficients of the first $n-2$ even-order terms, including the zeroth-order term, in either Eq. (2-22) or Eq. (2-23), and solve the resultant $n-1$ equations. The binary phase apertures based on these solutions would result in MFC in radial axis (by Eq. (2-22)) or axial axis (by Eq. (2-23)). To achieve MFC in both radial and axial axes simultaneously, we equate to zero the first $(n-2)$ pupil moments,

$$q_p = 0, \quad p = 0,1,2,...n-2, \tag{2-24}$$

whose solution set is the shared solution of the resultant equations from Eq. (2-22) and Eq. (2-23). The equations in Eq. (2-24) can be transformed and considered as a Vandermonde matrix [116], which has a solution of uniformly distributed points on a circle in the complex plane. Thus, one solution of Eq. (2-24) is obtained,

$$m_j = \left[1 - \cos(j\pi/n)\right]/2, \; j = 1,2,...,n-1 \tag{2-25}$$

Different from MFR in [74] where more than one solution sets with mirror images of each pair are found, there is only one solution set of Eq. (2-24) found for each aperture with the numbers of sub-apertures from 2 to 8. The normalized intensity profiles of binary phase apertures designed by the above solutions effectively achieve MFCs in the focal region of the detection optics (Figure 2.3). The MFC region extends in both radial and axial axes as increasing the number of sub-apertures (Figure 2.3 (a) and (b)). Although only the intensity profiles in radial and axial axes are considered in Eqs. (2-22) and (2-23), the MFC in 3D focal volume is successfully obtained (Figure 2.3 (c)).

Actually we can directly expand Eq. (2-9) by Taylor series and take square modulus to obtain the intensity distribution in 3D focal volume, and then following the same steps we will find that the solution set of Eq. (2-24) satisfies the resultant equations. Note that this method is suitable for both cases of even and odd numbers of sub-apertures, while the equal-ZPM aperture design is only applicable to the cases of even numbers.

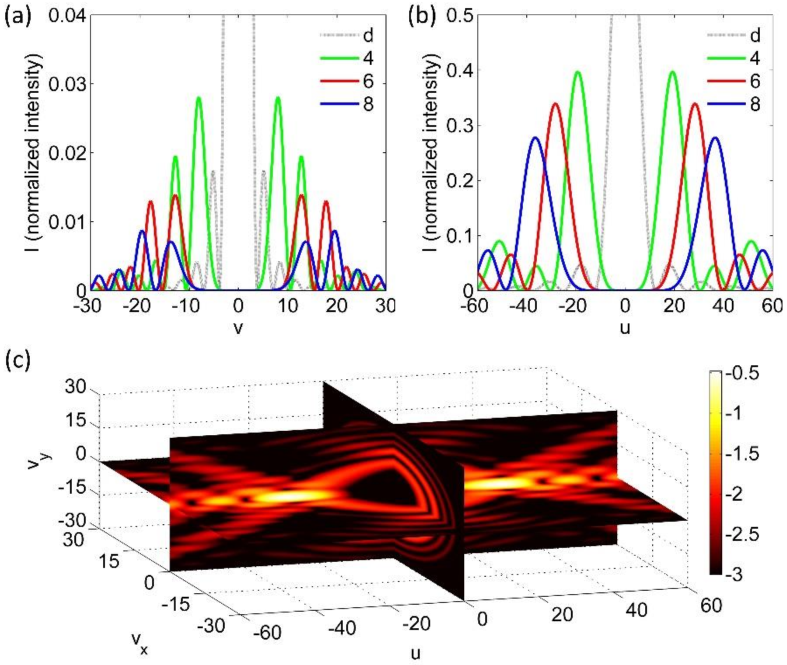

Figure 2.3 Normalized intensity profiles of binary phase apertures with 4 (green line), 6 (red line), 8 (blue line) sub-apertures and detection optics (d, dashed black line) in (a) radial and (b) axial axes. (c) Normalized intensity distribution of the binary phase aperture with 6 sub-apertures (colorbar in logarithmic scale).

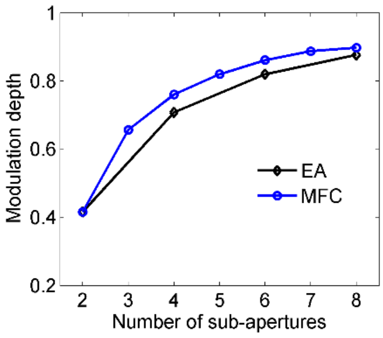

Figure 2.4 Modulation depth of FMM using apertures designed by equal-area (EA, black diamond) and MFC (blue circle).

Figure 2.4 compares the modulation depth of FMM with apertures designed by

MFC and equal-area (equivalent to equal-ZPM in scalar diffraction). The parameters are the same as in section 2.4.3. Except for the identical design for the case of 2 sub-apertures, MFC always leads to a larger modulation depth than equal-area for the same number of sub-apertures. Furthermore, the MFC aperture of 5 (or 6) sub-apertures has almost the same modulation depth compared with the equal-area aperture of 6 (or 8) sub-apertures, which is important to ease the fabrication of the aperture.

2.5.2 MFC for vector diffraction

Now we extend this analytic method to the FMM imaging system with a high NA objective lens. The excitation intensity in the focal region at the point r,ϕ,z in cylindrical coordinates is

$$I\left(r,\phi,z\right)=\left|E_x\right|^2+\left|E_y\right|^2+\left|E_z\right|^2, \tag{2-26}$$

where the field $E_{x,y,z}$ can be calculated through Eq. (2-15). By converting cylindrical coordinates to Cartesian coordinates, the intensity profiles in x,y,z axes can be obtained. Alternatively, we can specify particular values for r,ϕ,z to represent the intensity profiles in x,y,z axes. By substituting $r=0$ in Eqs. (2-15) and (2-26), the excitation intensity in z axis can be expressed with coefficients given by the pupil moment explicitly as

$$I\left(z\right)=A^2\left|\sum_{j=0}^{\infty}\frac{\left(ik\right)^j}{j!}q_j z^j\right|^2 . \tag{2-27}$$

To obtain the intensity expressions in the transverse axes, we specify $z=0$ in Eq. (2-16), which makes the exponential term in the equation omitted. Now we expand I_0, I_1 and I_2 in Eq. (2-16) as a power series with coefficients given by the pupil moment,

$$
\begin{aligned}
I_0 &= \sum_{j=0}^{\infty}\left[\frac{(-1)^j}{j!}\left(\frac{kr}{2}\right)^{2j}\sum_{m=0}^{j}\alpha_{j,m}q_{2m}\right] \\
I_1 &= \sum_{j=0}^{\infty}\left[\frac{(-1)^j}{(j+1)!}\left(\frac{kr}{2}\right)^{2j+1}\sum_{m=0}^{j}\alpha_{j,m}\left(q_{2m}-q_{2m+1}\right)\right] \\
I_2 &= \sum_{j=0}^{\infty}\left[\frac{(-1)^j}{(j+2)!}\left(\frac{kr}{2}\right)^{2j+2}\sum_{m=0}^{j}\alpha_{j,m}\left(q_{2m}-2q_{2m+1}+q_{2m+2}\right)\right],
\end{aligned}
\tag{2-28}
$$

where

$$
\alpha_{j,m} = \frac{(-1)^m}{m!(j-m)!}. \tag{2-29}
$$

Thus, the excitation intensity in x, y axes can be explicitly expressed by substituting Eq. (2-28) for I_0, I_1 and I_2 in Eq. (2-15).

Following the same steps as before, we equate to zero the coefficients of the first $(n-2)$ even-order terms, including the zeroth-order term, in any expressions of the intensity profiles in x, y, z axes, and solve the resultant $n-1$ equations to achieve MFC in the corresponding axis. Again the three sets of resultant equations share the same solution set, which is obtained by solving Eq. (2-24). It allows us to obtain MFC in x, y, z axes simultaneously. Note that here the pupil moment is defined by Eq. (2-19) based on vector diffraction theory.

To demonstrate MFC in high NA imaging system, the NA of 0.95 is chosen in the numerical simulation. The wavelength is the same as before. The pinhole diameter is 0.46 μm, also about 0.6 times of the diameter of the Airy disk. Figure 2.5 (a)~(c) show that the normalized intensity profiles of the binary phase apertures designed by these solutions effectively achieve MFCs in all x, y, z axes in the focal region of the detection optics. Note that here the detection optics is given by Eq. (2-21) based on vector diffraction. Figure 2.5 (d) shows the modulation depth of FMM with the apertures designed by equal-area (EA), equal-ZPM and MFC in the high NA imaging system.

Clearly the latter is remarkably superior to the equal-area aperture, and also better than the equal-ZPM aperture. The region of 'flat crater' extends in x, y, z axes as increasing the number of sub-apertures, so the modulation depth increases consequently.

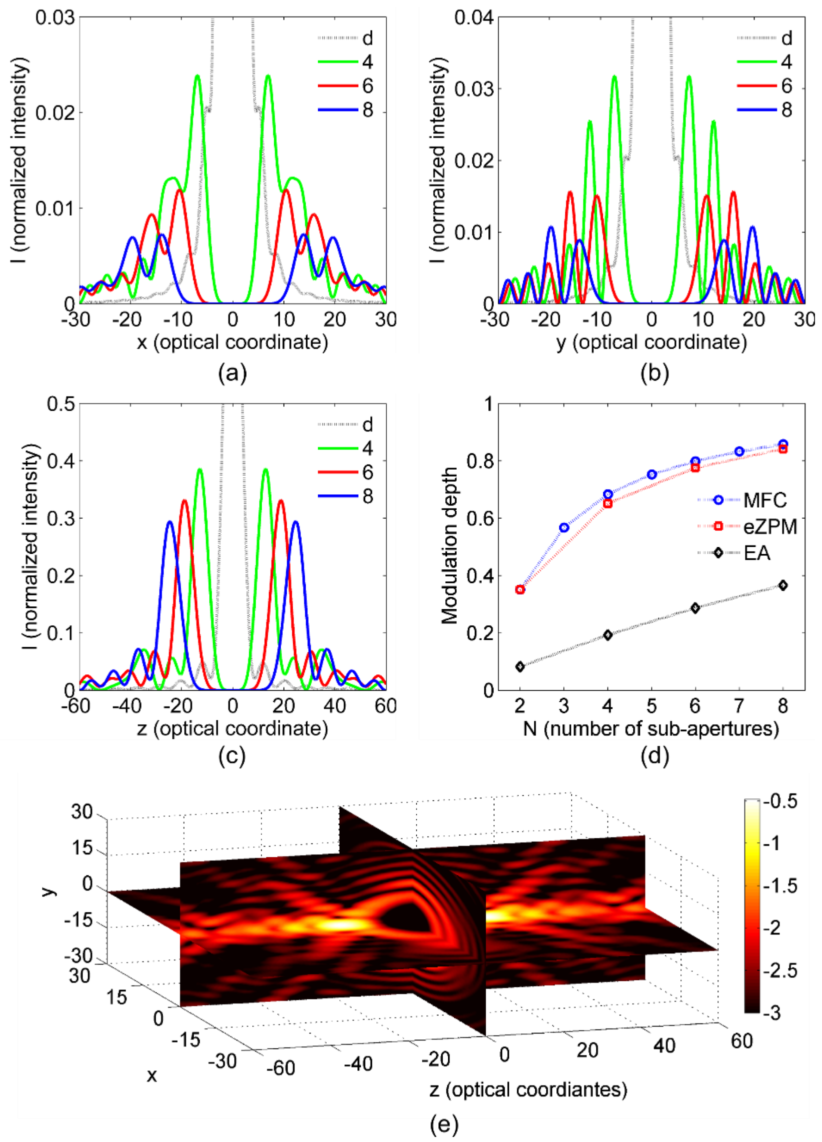

Figure 2.5 Normalized intensity profiles of binary phase apertures with 4 (green line), 6 (red line), 8 (blue line) sub-apertures and detection optics (d, dashed black line) in (a) x-, (b) y- and (c) z-axes. (d) Modulation depth of FMM with STPM apertures designed by EA (black diamond) and MFC (blue circle). (e) Normalized intensity distribution of the binary phase aperture with 6 sub-apertures (colorbar in logarithmic scale).

Figure 2.5 (e) indicates that the MFC in 3D focal region is also obtained in vector diffraction optics. One can directly expand Eq. (2-16) to demonstrate the solution set of Eq. (2-24) is the solution of the resultant MFC equations in 3D space, although it is more complicated.

To evaluate the performance of MFC apertures, we investigate the modulation depth of all possible annular designs for the aperture containing 3 sub-apertures (Figure 2.6 (a)), where the simulation parameters are the same as Figure 2.5 (d). The modulation depth of the MFC aperture is 0.57, which is very close to the maximum value 0.59; whereas the quasi equal-area (Quasi-EA in Figure 2.6 (a)) aperture shows a modulation depth of only 0.20. Here the Quasi-EA means the middle sub-aperture has the same area as the sum of inner and outer sub-apertures, while the areas of the inner and outer sub-apertures are equal. Furthermore, we compare the modulation depth of MFC apertures with the maximum modulation depth for the apertures containing 2~8 sub-apertures with the same simulation parameters in Figure 2.5 (d), where the maximum values are evaluated by genetic algorithm (GA). The results show that the difference of the modulation depth is less than 3% for the apertures containing the same number of sub-apertures (Figure 2.6 (b)).

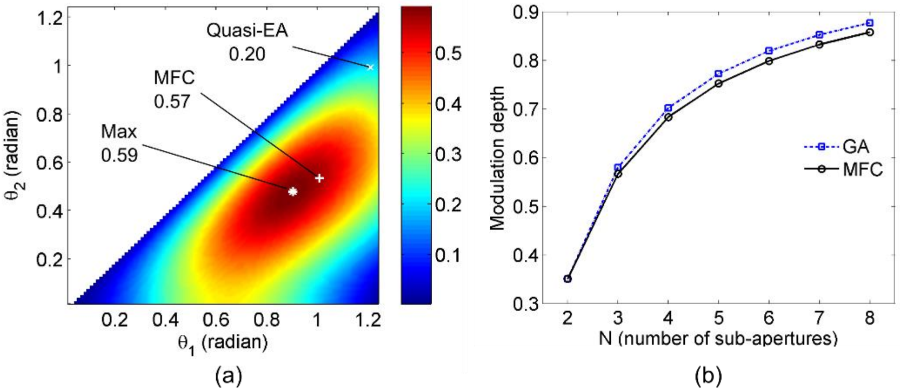

(a) (b)

Figure 2.6 (a) Modulation depth of FMM with the aperture containing 3 sub-apertures. (b) Modulation depth of FMM apertures designed by genetic algorithm (GA) and MFC with different number of sub-apertures.

Obviously the calculation based on scalar diffraction theory is much simpler than vector diffraction theory. The former is an approximation of the latter for a small angular aperture, i.e. a small NA [113]. It has been suggested that the scalar theory yields good results for $NA \leq 0.5$ [117], though the NA of 0.55 is chosen in our simulation for comparison with the result in [109]. Thus, a proper theory must be chosen to balance the calculation complexity and accuracy.

Besides the property of 3D darkness in focal volume, MFC apertures produce two focal points simultaneously along the optical axis without any ripples between the foci (Figure 2.3 (c) and Figure 2.5 (e)). The actual distance between the two focuses can be tuned by the number of sub-apertures and other imaging parameters, e.g. wavelength and the NA of objective lens. This bifocal property has potential applications, for instance, in readout of dual-layer disks, multiple optical traps, bifocal microscopy and optical lithography [56, 57, 118, 119].

2.5.3 Experiment results

A spatial light modulator (SLM) was employed to implement the phase pattern in the measurement of the modulation depth (Figure 2.7). An oil immersion objective lens with NA of 1.4 was used as illumination and collection objective. A wavefront sensor (WFS) was applied to monitor the phase pattern.

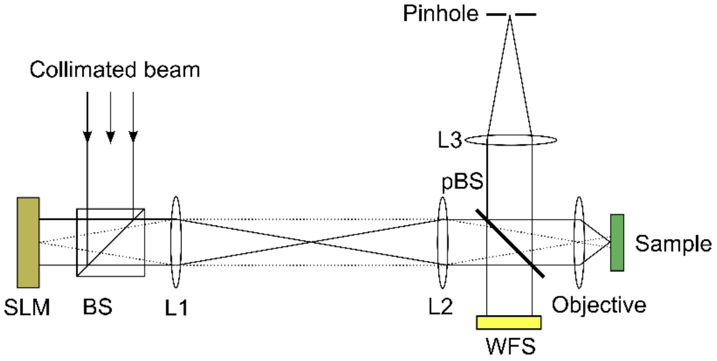

Figure 2.7 Schematic diagram of the modulation depth measurement. SLM is spatial light modulator, BS is beam splitter, pBS is pellicle beam splitter, WFS is wavefront sensor, The pinhole size is 25μm, and the focal lengths of L1, L2 and L3 are 125mm, 100mm and 175mm, respectively.

Figure 2.8 shows the simulation and experimental results of modulation depth for apertures designed by equal-ZPM and MFC, which verifies our proposed methods. The difference of the experiment and simulation results are mainly attributed to two reasons. The first is that the sample is assumed as uniform material with uniform emission in the whole 3D volume, which may not be satisfied in practice. For example, if only one emission particle is located at the focal spot, the modulation depth would always be unity as long as destructive interference occurs at the focus. The other reason is the unavoidable wavefront aberration in the experiment, although we tried our best to compensate for the aberrations with the SLM. In general, the measured modulation depth is consistent with the simulation results.

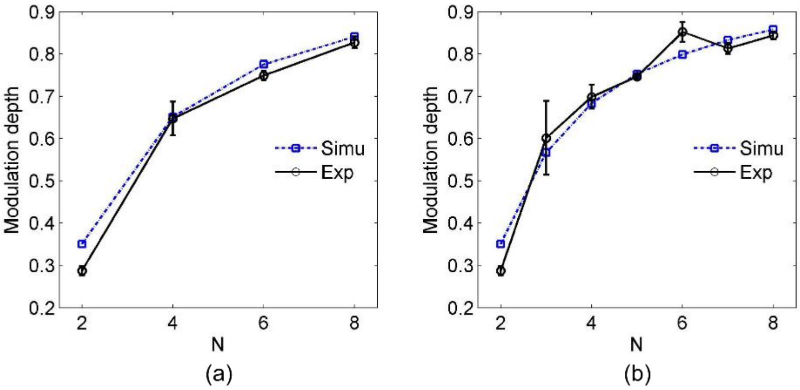

Figure 2.8 Simulation (Simu) and experimental (Exp) results of modulation depth for apertures designed by equal-ZPM (a) and MFC (b).

2.6 Effects of aberrations on the modulation depth

To investigate the effects of aberrations on the modulation depth, we added three types of Zernike aberrations (astigmatism, coma and trefoil) on the pupil function. The aberrations like tip/tilt and defocus are excluded, because they just lead to shift of focus position and can be easily corrected in practice. Here the apertures are designed by equal-ZPM without aberration, and the parameters are the same as in the scalar simulation for simplicity. Note that the field must be calculated by Eq. (2-8) rather than Eq. (2-9) since the pupil function is no longer rotationally symmetric due to aberration. We adopted fast Fourier transform (FFT) to implement the field calculation [120].

Figure 2.9 shows the modulation depth using different number of sub-apertures for astigmatism, coma and trefoil. The aberration degrades the modulation depth, because it can decrease the in-phase intensity and increase the anti-phase intensity. In general, the modulation depth decays as the root mean square (RMS) of the aberration increases. For coma, the modulation depth rises a little when the RMS of aberration increases beyond one wavelength, which is attributed to aberration compensation due to 2π ambiguity.

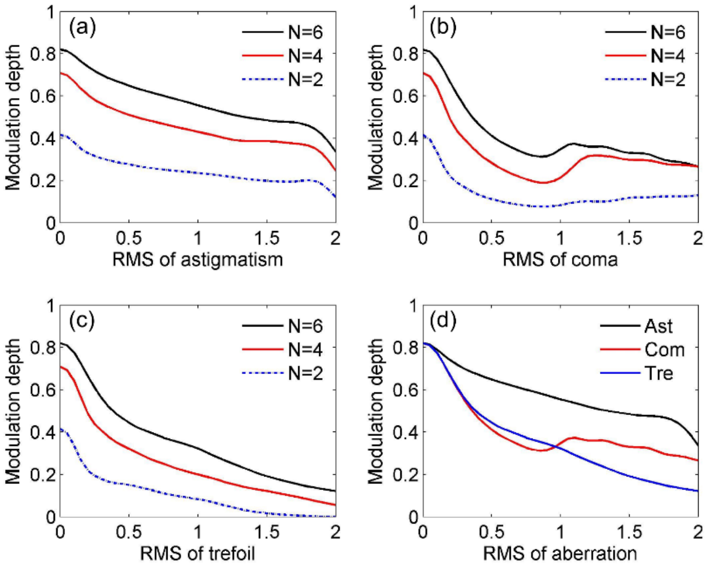

Figure 2.9 The modulation depth using different number of sub-apertures for (a) astigmatism (Ast), (b) coma (Com) and (c) trefoil (Tre). (d) Comparison of effects of different kinds of aberrations. The unit of RMS is in wavelength.

The aperture with more number of sub-apertures is more resistant to the degradation of aberration. For example, the modulation depth of the aperture with 6 sub-apertures decreases to 0.2 at $RMS = 1.5$ in presence of trefoil aberration, whereas the modulation depth that with 2 sub-apertures decreases to the same level at $RMS = 0.2$. Thus, a balance of aberration resistance and manufacture complexity must be carefully considered in practice.

As shown in Figure 2.9 (d), different aberrations have different degradation effects on the modulation depth. Coma degrades the modulation depth more than astigmatism and trefoil when the RMS of aberration is less than unity, while trefoil becomes the worst because of aberration compensation in coma. Even for astigmatism, the modulation depth drops to one-half at $RMS = 1.9$ compared to the value without aberration. Thus, adaptive optics, which is used to compensate for wavefront aberration, is expected to improve the performance of FMM in practice.

2.7 Conclusion

In this chapter, we introduced three methods based on pupil moment to optimize the aperture design in FMM. The equal-ZPM is a straightforward extension of the previously proposed method of equal-areas, but suitable for nonuniform illumination and high NA system. The zero-sum ZPM provides the optimal aperture design for given conditions, however, it requires optimization algorithms which are usually complicated and time consuming. The MFC method, which takes advantages of series expansion and pupil moment, offers a simple analytic approach to optimize annular phase apertures. The modulation depth from MFC is very close to the maximum value, with a small difference of less than 3% for the same number of sub-apertures. In addition, the apertures with more sub-apertures are more resistant to wavefront aberrations, although aberration degrades modulation depth in general.

Chapter 3

Cylindrical polarization in focal modulation microscopy

3.1 Introduction

Cylindrically polarized light is known to produce a tight focusing spot by applying proper apodization [66] or phase encoding [67]. Most recently, subtraction imaging in CM with radially and azimuthally polarized light was verified for lateral resolution improvement [121]. Here we investigate the performance of circularly polarized light, radially polarized light, and azimuthally polarized light encoding by spiral phase (abbreviated to 'AziSpi') used in focal modulation microscopy (FMM). Firstly we derive the representation of field in the focal region for different polarizations. Then the annular phase apertures in FMM for the cylindrical polarization are optimized by the MFC method which was introduced in section 2.5. The effects of apodization on FMM for radial polarization and AziSpi are investigated by evaluation of resolution, modulation depth, Strehl ratio and focusing efficiency.

3.2 Field in focal region

Consider a non-paraxial perfect focusing system as illustrated in Figure 3.1, the incident monochromatic wave propagates through the reference surface and transforms to a perfect converging wave. According to Debye-Wolf integral, the field $\mathbf{E}^f$ in the focal region of the system is expressed as [113]

$$\mathbf{E}^f\left(P\right)=-iAk\iint_{\Omega}\mathbf{E}^r\left(S\right)\exp\left(ik\mathbf{q}\cdot\mathbf{R}\right)d\Omega, \tag{3-1}$$

where P denotes the position in the focal region, k is the wave number, A is a constant for normalization, $\mathbf{E}^r$ depicts the refractive wave just after the reference surface, S denotes the position on the reference surface which is restricted by the numeric aperture (NA) of the system, $\boldsymbol{\Omega}$ is the solid angle subtended by the aperture as seen from the focal point, $d\Omega = \sin\theta d\theta d\varphi$, $\mathbf{q}$ is the unit vector in the direction of the converging refractive ray and is given by

$$\mathbf{q} = \left(\sin\theta\cos\varphi,\ \sin\theta\sin\varphi,\ \cos\theta\right), \tag{3-2}$$

and $\mathbf{R}$ is the position vector depicting the point P in the focal region and is given by

$$\mathbf{R} = \left(r_P\cos\varphi_P,\ r_P\sin\varphi_P,\ z_P\right), \tag{3-3}$$

with the cylindrical coordinates $\left(r_P,\ \varphi_P,\ z_P\right)$. The relationship between the cylindrical coordinates and the Cartesian coordinates in Figure 3.1 is simply as $x = r_P\cos\varphi_P$, $y = r_P\sin\varphi_P$, $z = z_P$. Therefore, the term in the exponent of the integral Eq. (3-1) becomes

$$\mathbf{q}\cdot\mathbf{R} = r_P\sin\theta\cos\left(\varphi - \varphi_P\right) + z_P\cos\theta. \tag{3-4}$$

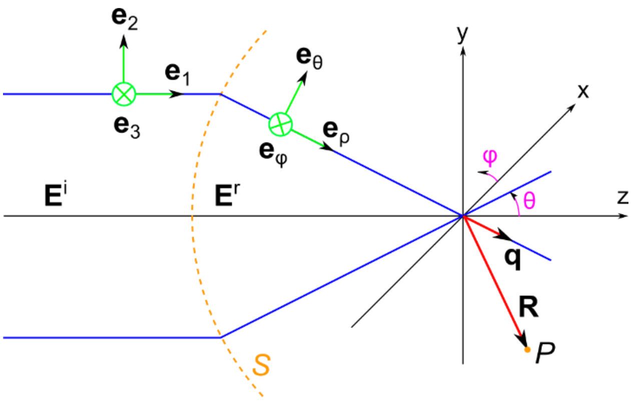

Figure 3.1 The focusing geometry.

To calculate the integral Eq. (3-1), the relationship between the incident wave $\mathbf{E}^i$ and the refractive wave $\mathbf{E}^r$ is required. The polarization of the incident wave changes due to refraction occurring at the reference surface. We depict the orthogonal local polarization components of the incident wave by the unit vector $\left(\mathbf{e}_1, \mathbf{e}_2, \mathbf{e}_3\right)$, and that of the refractive wave by $\left(\mathbf{e}_\rho, \mathbf{e}_\theta, \mathbf{e}_\varphi\right)$. The transformation of the polarization can be described as

$$\begin{bmatrix} \mathbf{e}_\rho \\ \mathbf{e}_\theta \\ \mathbf{e}_\varphi \end{bmatrix} = \begin{bmatrix} \mathbf{e}_1 \\ \mathbf{e}_2 \\ \mathbf{e}_3 \end{bmatrix} = \overline{\overline{\mathbf{M}}}_1 \mathbf{e}^i = \begin{bmatrix} \cos\varphi & \sin\varphi & 0 \\ -\sin\varphi & \cos\varphi & 0 \\ 0 & 0 & 1 \end{bmatrix} \begin{bmatrix} \mathbf{e}_x^i \\ \mathbf{e}_y^i \\ \mathbf{e}_z^i \end{bmatrix}, \tag{3-5}$$

$$\begin{bmatrix} \mathbf{e}_x^r \\ \mathbf{e}_y^r \\ \mathbf{e}_z^r \end{bmatrix} = \overline{\overline{\mathbf{M}}}_2 \begin{bmatrix} \mathbf{e}_\rho \\ \mathbf{e}_\theta \\ \mathbf{e}_\varphi \end{bmatrix} = \begin{bmatrix} \cos\theta\cos\varphi & -\sin\varphi & -\sin\theta\cos\varphi \\ \cos\theta\sin\varphi & \cos\varphi & -\sin\theta\sin\varphi \\ \sin\theta & 0 & \cos\theta \end{bmatrix} \begin{bmatrix} \mathbf{e}_\rho \\ \mathbf{e}_\theta \\ \mathbf{e}_\varphi \end{bmatrix}, \tag{3-6}$$

where $\mathbf{e}^i$ and $\mathbf{e}^r$ denote the polarization components of incident wave and refractive wave, respectively, with the universal coordinates x, y, z defined in Figure 3.1. Thus, the transformation of the incident wave $\mathbf{E}^i$ and refractive wave $\mathbf{E}^r$ is described as

$$\mathbf{E}^r = \sqrt{\cos\theta}\,\overline{\overline{\mathbf{M}}}\mathbf{E}^i, \tag{3-7}$$

$$\begin{aligned} \overline{\overline{\mathbf{M}}} &= \overline{\overline{\mathbf{M}}}_2 \overline{\overline{\mathbf{M}}}_1 \\ &= \frac{1}{2} \begin{bmatrix} (\cos\theta+1)+(\cos\theta-1)\cos2\varphi & (\cos\theta-1)\sin2\varphi & -2\sin\theta\cos\varphi \\ (\cos\theta-1)\sin2\varphi & (\cos\theta+1)-(\cos\theta-1)\cos2\varphi & -2\sin\theta\sin\varphi \\ 2\sin\theta\cos\varphi & 2\sin\theta\sin\varphi & 2\cos\theta \end{bmatrix}, \end{aligned} \tag{3-8}$$

where the factor $\sqrt{\cos\theta}$ comes from energy conservation [113].

Therefore, for a given incident field, the field in the focal region can be derived through Eqs. (3-1) ~ (3-8). The equations are applicable for incident wave with any polarization and any phase as long as the Debye approximation is satisfied. In the optical system considered here, the field of interest is near the focus and the focal length is much greater than the wavelength, so the Debye approximation is applicable.

Although there are efficient numerical integration algorithms to evaluate two-dimensional (2D) integral, it is still time-consuming to calculate the whole field in three-dimensional (3D) focal volume through direct implementation of Eq. (3-1). The fast Fourier transform (FFT) and chirp z transform (CZT) in 2D and 3D were proposed to speed up the integral calculation [120, 122, 123]. Nevertheless, for the circularly symmetric incident waves considered here, the 2D integral can convert to one-dimensional (1D) integral by the integral representation of the Bessel function of the first kind:

$$\int_0^{2\pi} \exp\left[i\left(n\varphi+\rho\cos\varphi\right)\right]d\varphi = 2\pi i^n J_n\left(\rho\right). \tag{3-9}$$

3.3 Phase aperture designed by maximally-flat crater (MFC)

The MFC method proposed in section 2.5 was employed to design annular phase apertures for different polarized illuminations in FMM. To implement MFC, the pupil moment must be defined properly for different polarizations, then the apertures can be designed by following the steps in section 2.5. Here the expressions of the field for different polarizations in the focal region are derived, and then the definition of the pupil moment are given. By applying Eq. (3-9) and corresponding series expansion Eq. (3-10), the field and intensity in the focal region can be expanded with coefficients given by the pupil moment, which can be used to verify the consistence of MFC implementation based on pupil moment and that based on intensity expansion.

$$J_n\left(x\right) = \sum_{l=0}^{\infty} \frac{\left(-1\right)^l}{2^{2l+n} l!\left(l+n\right)!} x^{2l+n} \tag{3-10}$$

3.3.1 Linear polarization

For an incident wave linearly polarized in *x*-direction, given by $\mathbf{E}^i = \left(1,\ 0,\ 0\right)$, the refractive wave is derived as

$$\mathbf{E}^r = \frac{1}{2}\sqrt{\cos\theta}\begin{bmatrix} \left(\cos\theta+1\right)+\left(\cos\theta-1\right)\cos 2\varphi \\ \left(\cos\theta-1\right)\sin 2\varphi \\ 2\sin\theta\cos\varphi \end{bmatrix}, \tag{3-11}$$

which is equivalent to the strength factor as defined in [113].

The field in the focal region is derived by Eqs. (3-1) ~ (3-8), and expressed as

$$\mathbf{E}^f(P) = -iAk\begin{bmatrix} I_0^l + I_2^l\cos 2\varphi_P \\ I_2^l \sin 2\varphi_P \\ 2iI_1^l\cos\varphi_P \end{bmatrix}, \tag{3-12}$$

where

$$\begin{aligned} I_0^l &= \int_0^\alpha \sqrt{\cos\theta}\sin\theta(1+\cos\theta)J_0(kr_P\sin\theta)\exp(ikz_P\cos\theta)\mathrm{d}\theta \\ I_1^l &= \int_0^\alpha \sqrt{\cos\theta}\sin^2\theta J_1(kr_P\sin\theta)\exp(ikz_P\cos\theta)\mathrm{d}\theta \\ I_2^l &= \int_0^\alpha \sqrt{\cos\theta}\sin\theta(1-\cos\theta)J_2(kr_P\sin\theta)\exp(ikz_P\cos\theta)\mathrm{d}\theta, \end{aligned} \tag{3-13}$$

with α the semi-angular aperture determined by numerical aperture ($NA = \sin\alpha$). The result is the same as in [113] and can be rewritten as Eq. (2-16) for the convenience of defining pupil moment. The aperture design is illustrated in section 2.5.2.

3.3.2 Circular polarization

The wave of circular polarization can be described as $\mathbf{E}^i = (1,\ \pm i,\ 0)$, where the plus-minus sign denotes the left and right circular polarizations. Without loss of generality, either circular polarization considered is enough since they have the same intensity distribution in the focal volume. For the left circular polarization, the field in the focal region is derived as

$$\mathbf{E}^f(P) = Ak\begin{bmatrix} -i\left(I_0^c + I_2^c e^{i2\varphi_P}\right) \\ I_0^c - I_2^c e^{i2\varphi_P} \\ 2I_1^c e^{i\varphi_P} \end{bmatrix}, \tag{3-14}$$

where the terms $I_0^c,\ I_1^c,\ I_2^c$ are equivalent to $I_0^l,\ I_1^l,\ I_2^l$ as in Eq. (3-13), respectively. Thus, the pupil moment can be defined and calculated the same as that of linear polarization, i.e. Eqs. (2-19) and (2-20).

Although the terms I_n^c ($n = 0,1,2$) in the circular polarization share the same expression as the linear polarization, the fields in the focal region have different symmetry properties. The transverse field in Eq. (3-14) can be decomposed into two circular waves: one with constant phase (I_0^c) and the other with spiral phase ($I_2^c e^{i2\varphi_p}$). Therefore, the intensity distribution is rotationally symmetric, described as

$$I\left(P\right)=\left|E_x\right|^2+\left|E_y\right|^2+\left|E_z\right|^2=2A^2k^2\left(\left|I_0^c\right|^2+2\left|I_1^c\right|^2+\left|I_2^c\right|^2\right). \qquad (3\text{-}15)$$

3.3.3 Radial polarization

For a radially polarized incident wave, given by $\mathbf{E}^i=\left(\cos\varphi,\ \sin\varphi,\ 0\right)$, the field in the focal region is derived as

$$\mathbf{E}^f\left(P\right)=Ak\begin{bmatrix} I_1^r\cos\varphi_P \\ I_1^r\sin\varphi_P \\ 2iI_0^r \end{bmatrix}, \qquad (3\text{-}16)$$

where I_0^r and I_1^r are given by

$$\begin{aligned} I_0^r &=\int_0^\alpha\sqrt{\cos\theta}\sin^2\theta J_0\left(kr_P\sin\theta\right)\exp\left(ikz_P\cos\theta\right)\mathrm{d}\theta \\ I_1^r &=\int_0^\alpha\sqrt{\cos\theta}\sin2\theta J_1\left(kr_P\sin\theta\right)\exp\left(ikz_P\cos\theta\right)\mathrm{d}\theta. \end{aligned} \qquad (3\text{-}17)$$

Obviously the transverse field in Eq. (3-16) is radially symmetric, so the intensity distribution deserves the same symmetry property, which is given by

$$I\left(P\right)=\left|E_x\right|^2+\left|E_y\right|^2+\left|E_z\right|^2=2A^2k^2\left(2\left|I_0^r\right|^2+\left|I_1^c\right|^2\right). \qquad (3\text{-}18)$$

To define the pupil moment used in MFC, Eq. (3-17) can be rewritten as

$$\begin{aligned} I_0^r &=\int_{-\infty}^{+\infty}Q\left(c\right)J_0\left(kr_P\sqrt{1-c^2}\right)\exp\left(ikz_Pc\right)\mathrm{d}c \\ I_1^r &=\int_{-\infty}^{+\infty}Q\left(c\right)\frac{c}{\sqrt{1-c^2}}J_0\left(kr_P\sqrt{1-c^2}\right)\exp\left(ikz_Pc\right)\mathrm{d}c, \end{aligned} \qquad (3\text{-}19)$$

with the pupil function *Q(c)* expressed as a function of $c=\cos\theta$. *Q(c)* includes the effects of the phase aperture and illumination beam profile *P(c)*, and can be written as

$$Q(c)=\sqrt{c\left(1-c^2\right)}P(c)T(c), \tag{3-20}$$

where *T(c)* is the transmission function of the phase aperture which is described by Eq. (2-18). Therefore, the pupil moment is depicted as

$$\begin{aligned} q_p &= \int Q(c)\mathrm{c}^p \mathrm{d}c \\ &= \sum_{j=1}^{N}\int_{c_{j-1}}^{c_j} (-1)^j \sqrt{1-c^2}\, c^{n+1/2} dc, \end{aligned} \tag{3-21}$$

which can be evaluated numerically for a given system.

3.3.4 Azimuthal polarization with spiral phase

An incident wave of AziSpi is depicted by $\mathbf{E}^i = \left(-\sin\varphi,\ \cos\varphi,\ 0\right)\exp\left(in\varphi\right)$ with n an integer number. The field in the focal region is given by

$$\mathbf{E}^f\left(P\right)=Ak\begin{bmatrix} i^{n+1}e^{i(n+1)\varphi_p}I_{n+1}^a - i^{n-1}e^{i(n-1)\varphi_p}I_{n-1}^a \\ -i\left(i^{n+1}e^{i(n+1)\varphi_p}I_{n+1}^a + i^{n-1}e^{i(n-1)\varphi_p}I_{n-1}^a\right) \\ 0 \end{bmatrix}, \tag{3-22}$$

with

$$I_n^a = \int_0^\alpha \sqrt{\cos\theta}\sin\theta J_n\left(kr_p\sin\theta\right)\exp\left(ikz_p\cos\theta\right)d\theta. \tag{3-23}$$

The azimuthally polarized light encoding by the first-order spiral phase ($n=1$) introduces a tight focus spot [67], whereas with spiral phase of other orders it causes donut-shaped focal intensity distributions. Here only the light encoding by the first-order spiral phase is considered for FMM application, and the field in the focal region is expressed explicitly as

$$\mathbf{E}^f\left(P\right)=-Ak\begin{bmatrix} I_0^a + I_2^a e^{i2\varphi_p} \\ i\left(I_0^a - I_2^a e^{i2\varphi_p}\right) \\ 0 \end{bmatrix}. \tag{3-24}$$

Similar to previous process for radial polarization, Eq. (3-23) can be rewritten as

$$I_n^a = \int_{-\infty}^{+\infty} Q(c) J_n\left(kr_P\sqrt{1-c^2}\right)\exp\left(ikz_P c\right)\mathrm{d}c, \tag{3-25}$$

where the pupil function *Q(c)* is given by

$$Q(c)=\sqrt{c}P(c)T(c), \tag{3-26}$$

with *T(c)* the transmission function of the phase aperture described by Eq. (2-18). For uniform illumination, the pupil moment can be described explicitly as

$$\begin{aligned} q_p &= \int Q(c)\mathrm{c}^p\mathrm{d}c \\ &= \frac{1}{p+3/2}\sum_{j=1}^{n}(-1)^j\left(c_j^{p+3/2}-c_{j-1}^{p+3/2}\right). \end{aligned} \tag{3-27}$$

Similar to the circular polarization, the transverse field in Eq. (3-24) can also be decomposed into two circular waves: one with constant phase (I_0^a) and the other with spiral phase ($I_2^a e^{i2\varphi_p}$). Therefore, the intensity distribution is rotationally symmetric:

$$I(P)=\left|E_x\right|^2+\left|E_y\right|^2+\left|E_z\right|^2=2A^2k^2\left(\left|I_0^a\right|^2+\left|I_2^a\right|^2\right). \tag{3-28}$$

3.4 Comparison of different polarizations in FMM

In the simulations, the illumination and emission wavelengths are assumed the same for convenience, i.e. 0.633μm, the objective lenses for illumination and collection have the same NA, and $NA=0.95$ is chosen if not specified. In previous simulation based on scalar diffraction theory (section 2.4.3), the pinhole diameter is 0.8μm, about 0.6 times of the diameter of Airy disk, which is 1.35 times of the FWHM of the Airy disk. In vector diffraction, the size of the focal intensity distribution changes with various NA even in optical coordinates, so the pinhole size based Airy disk diameter does not have comparable sectioning effect or efficiency. Therefore, the pinhole size based on the illumination PSF, i.e., 1.35 times of the FWHM of the PSF, is chosen instead.

3.4.1 Annular aperture design

The aperture design for the circular polarization is expected the same as that for linear polarization, since they share the same definition of pupil moment. Figure 3.2 shows the aperture designs for different polarizations, where the radius is normalized by the size of the aperture. For a given number of sub-apertures, the MFC design shows large area in the outer annular region for the circular polarization, while relatively smaller area for the radial polarization. This may be attributed to the decreasing factors, i.e. $\left(1+c\right)$, 1, $\sqrt{1-c^2}$, in the expressions of the pupil functions (Eqs. (2-17), (3-26) and (3-20), respectively), which affect the integrands in the definition of the pupil moment. For all the polarizations, the areas of the middle sub-apertures become relatively larger than the inner and outer parts as the number of the sub-apertures increases.

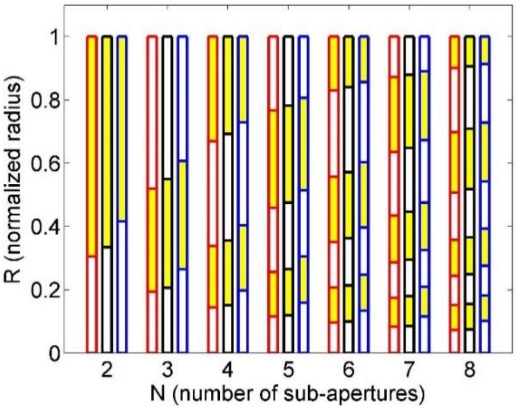

Figure 3.2 The normalized radius of the annular phase apertures for circular polarization (red), AziSpi (black) and radial polarization (blue). The yellow and white bars denote the modulated and unmodulated parts, respectively.

3.4.2 Intensity distribution in focal region

The intensity distributions of both in-phase and anti-phase are investigated here to compare different polarizations. Figure 3.3 (a) and (d) show the in-phase intensity distributions for circular polarization (blue line), radial polarization (red point dashed line) and AziSpi (black dashed line) with $NA = 0.75$ along transverse and axial directions, respectively. The optical coordinates are defined as $v = kr\sin\alpha$,

$u = 4kz\sin^2(\alpha/2)$, where k is the wave number, α is the angular semi-aperture of the objective lens, and r, z are the physical distances from the focal point in cylindrical coordinates. The AziSpi shows the narrowest FWHM in both transverse and axial directions, while the transverse FWHM of the radial polarization is significantly wider. When NA increases to 0.95, the transverse FWHM of the radial polarization shrinks close to the other polarizations (Figure 3.3 (b)), which means the radial polarization benefits in high NA system. In addition, the axial FWFM of the radial polarization is a little wider than the other polarizations (Figure 3.3 (d) and (e)).

Figure 3.3 (c) and (f) show the anti-phase intensity distributions of the aperture with 4 sub-apertures. In the transverse plane, the energy in the circular polarization is pushed further away than the other polarizations, which is expected to lead to less anti-phase signal and thus larger modulation depth. In the axial direction, the side-lobe is shifted a little further away in the radial polarization.

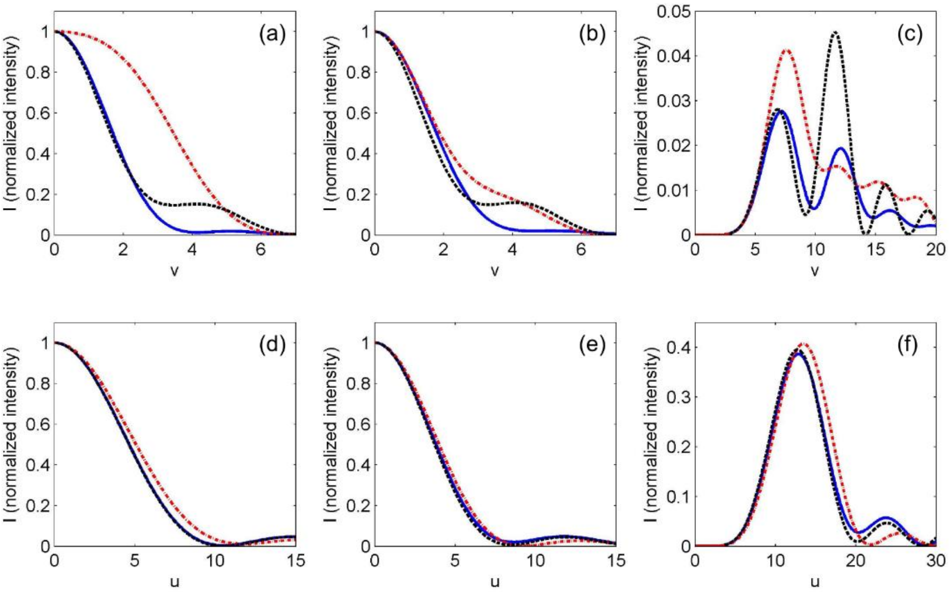

Figure 3.3 Normalized intensity profiles of in-phase apertures ((a), (b), (d) and (e)) and anti-phase apertures with 4 sub-apertures ((c) and (f)) for circular polarization (blue line), radial polarization (red point dashed line) and AziSpi (black dashed line) along transverse direction (u=0) ((a) ~ (c)) and axial direction (v=0)((d) ~ (f)). NA=0.75 in (a) and (d), while NA=0.95 in the other figures.

3.4.3 Modulation depth

Figure 3.4 shows the modulation depth of annular apertures designed by MFC with different polarizations. In general, the modulation depth increases as the number of the sub-apertures increases, because the volume of the ‘flat-crater’ increases and then the anti-phase signal decreases.

For a given number of the sub-apertures, the modulation depth decreases in the circular polarization and the AziSpi as the numerical aperture (NA) increases (Figure 3.4 (a) and (c)), whereas it increases in the radial polarization (Figure 3.4 (b)). This is attributed to that the pinhole size, which is based on the FWHM of the illumination PSF, decreases in the radial polarization when the NA increases. Actually the radial polarization benefits the high NA system, where it can produce a tight focusing spot [58, 65, 66], but results in broad focusing spot in the low NA system.

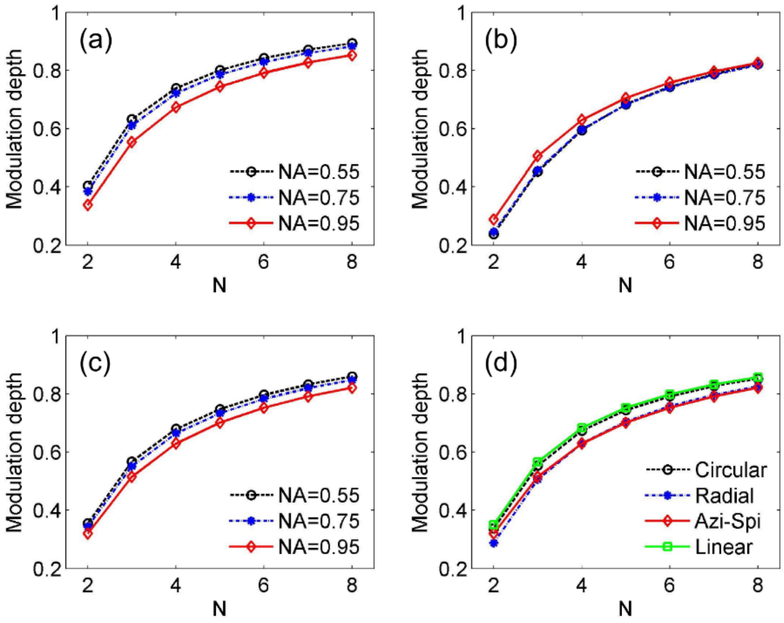

Figure 3.4 Modulation depth of apertures designed by MFC using different numbers of sub-apertures with (a) circular polarization, (b) radial polarization and (c) AziSpi. (d) Comparison of modulation depth with different polarizations for high NA system (NA=0.95).

Figure 3.4 (d) compares the modulation depth for different polarizations in the high NA system ($NA = 0.95$). The modulation depth in the circular and linear polarizations is greater than that in the radial polarization and AziSpi, because in the former cases the energy of the anti-phase is pushed further away from the focus (see Figure 3.3 (c)).

3.4.4 Resolution

Figure 3.5 shows the transverse FWHM of the in-phase PSF with different NA and different polarizations. The unit of FWHM is based on optical coordinates which is given by $v = \frac{2\pi}{\lambda} x \cdot NA$ with λ the wavelength and x the physical distance. The PSF of the linear polarization is not rotationally symmetric, so the averaged FWHM is employed for comparison. The averaged FWHM is given by

$$FWHM_{average} = \sqrt{FWHM\left(x\right) \times FWHM\left(y\right)}, \tag{3-29}$$

where $FWHM\left(x\right)$ and $FWHM\left(y\right)$ are the FWHM along x- and y- axes.

The FWHM of radial polarization is very large when the NA is small, which implies that the radially polarized illumination is only suitable for high NA imaging system. The FWHM of linear and circular polarizations increases as the NA increases, whereas the FWHM of radial polarization and AziSpi decays monotonically. For a given NA, the AziSpi illumination is expected to provide the best resolution as the FWHM of AziSpi is the narrowest.

It seems counterintuitive that The FWHM of linear and circular polarizations increases for larger NA. It is true that, for larger NA, more high frequency components are involved, and consequently, the FWHM (evaluated in physical coordinates) and imaging result become better. However, the FWHM in Figure 3.5 is evaluated in optical coordinates rather than physical coordinates. The optical coordinates were introduced to exclude the influences of NA and wavelength in evaluating the field in the focal region based on scalar diffraction theory (Eq. (2-8)). Here the optical coordinates are used to show the effect of NA for different polarizations in vector diffraction theory. In this case, the intensity contributions from all the transverse and longitudinal (x-, y-

and z-) fields are included in the evaluation of the FWHM. The change of NA introduces the change of the relative strengths of the transverse and longitudinal fields, which causes the variation of the FWHM. For example, for an incident wave linearly polarized in x-direction, the fields along y- and z- directions in the focal region increase when the NA increases. The increase of the fields along y- and z- directions makes the FWHM (evaluated in optical coordinates) worse due to the characteristics of the first (J_1) and second (J_2) Bessel functions of the first kind (Eq. (3-12) and (3-13)).

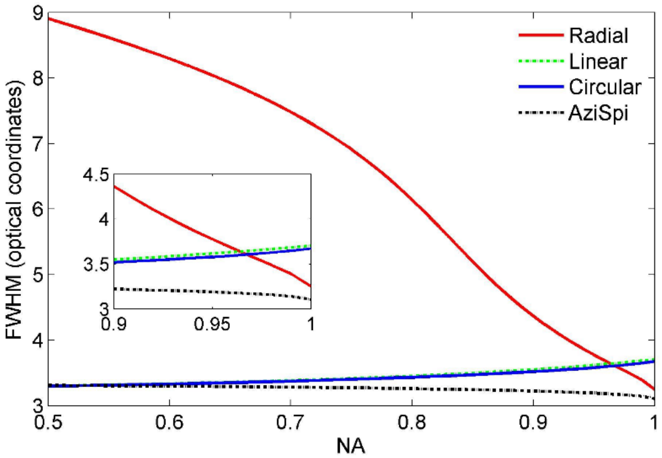

Figure 3.5 FWHM of different polarizations. The inserted figure shows the FWHM at the range of NA from 0.9 to 1. The unit of FWHM is in optical coordinates.

3.5 Apodization

Various apodization designs for cylindrically polarized light have been proposed to improve the resolution [56, 58, 65, 66, 124-127] or focal depth [78, 127]. The apodization techniques can be employed in FMM by directly overlapping the apodization pattern and the MFC pattern to improve the resolution and sectioning capability simultaneously. In such a way, the total number of the sub-apertures would be the sum of the apodization pattern and the MFC pattern, so the complexity of the aperture fabrication must be considered in practice. Note that the possibly increased focal depth introduced by apodization would be missing because FMM employs a pinhole to implement 'depth sectioning'.

Here, as an example, the inner-blocked apodization was investigated to apply in FMM, since this apodization pattern is so simple that we can focus on the influence of the apodization on the performance of FMM. The inner-blocked apodization can be considered as the simplest configuration of the shaded-mask filter [76], leaky filter [57] or three-level filter [75]. To combine it in FMM, the MFC design was implemented in the unblocked region of the aperture. We define the ratio of the radii of the inner-blocked and the outer unblocked aperture as the annular factor, which is described as

$$\eta = \frac{r_{inner-blocked}}{r_{outer}}. \tag{3-30}$$

An inner-blocked annular aperture with 3 sub-apertures is shown in Figure 3.6 to illustrate the configuration more clearly, where the inner black part is blocked, the grey annular parts are phase-modulated parts and the white annular part is unmodulated.

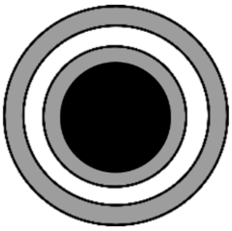

Figure 3.6 An inner-blocked annular aperture with 3 sub-apertures.

3.5.1 Resolution

The resolution of FMM is determined by the illumination PSF, detection optics and the pinhole size, where the latter two factors are not affected by the inner-blocked apodization. Therefore, the full width at half maximum (FWHM) of the illumination PSF can be used to evaluate the transverse resolution, because here we focus on the influence of the apodization which is irrelevant to the detection optics and the pinhole size. Furthermore, the FWHM of the in-phase PSF can be employed to substitute the illumination PSF, since the MFC design produces a ‘flat crater’ in the focus which makes the main-lobe of the illumination PSF almost not affected by the anti-phase PSF. In such a way, the transverse resolution can be evaluated without any influence of the number of the sub-apertures. On the other hand, the axial resolution is mainly affected by the detection optics and the pinhole size, because the axial size of the illumination PSF in inner-blocked apodization for cylindrical polarization is usually larger than the size of the detection optics. So the overall axial resolution is determined by the detection optics and the pinhole size (see the integrand in Eq. (2-6)). Thus, we focus on investigating the transverse resolution here.

Figure 3.7 shows the transverse FWHM of the in-phase PSF with different annular factors and different polarizations. The unit of FWHM is based on optical coordinates, and the averaged FWHM of the linear polarization (Eq. (3-29)) is employed for comparison.

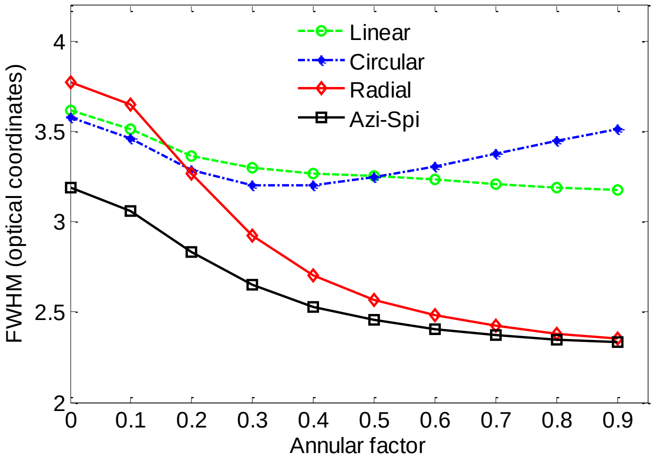

Figure 3.7 The transverse FWHM of the in-phase PSF with different annular factors for linear (green circle), circular (blue star) and radial (red diamond) polarizations, and AziSpi (black square, Azi-Spi). The unit of FWHM is based on optical coordinates.

In Figure 3.7, the FWHM of radial polarization and AziSpi decreases significantly as the annular factor increases. When the annular factor reaches 0.9, the FWHM of the both polarizations approaches 2.34, which is $\lambda/2.55$ equivalently. The resolution of radial polarization benefits the most from the inner-blocked apodization, since the FWHM decreases the most quickly as the annular factor increases. In addition, the AziSpi gives the best resolution when there is no apodization. Thus, the performance of the AziSpi is the best from the view point of resolution enhancement.

On the other hand, when the annular factor increases, the FWHM of linear polarization decreases slowly, while the FWHM of circular polarization decreases a little at the beginning and then increases to its initial value. In general, the resolution of linear and circular polarizations is little affected by the inner-blocked apodization. Thus, they would not be considered in the following investigations, since the apodiation here is expected to improve the resolution and performance of FMM simultaneously.

3.5.2 Modulation depth

Figure 3.8 shows the modulation depth of FMM with different annular factors and different numbers of sub-apertures for radial polarization and AziSpi. In general, the modulation depth increases as the annular factor increases, which will ease the fabrication of the aperture significantly. For example, the modulation depth of 8 sub-apertures without apodization is about 0.82, which value can be exceeded by proper inner-blocked apodization applied on 2 sub-apertures ($\eta \geq 0.8$), 3 sub-apertures ($\eta \geq 0.6$) and 4 sub-apertures ($\eta \geq 0.4$) in radial polarization, or 2 sub-apertures ($\eta \geq 0.8$), 3 sub-apertures ($\eta \geq 0.7$) and 4 sub-apertures ($\eta \geq 0.5$) in the AziSpi. Obviously the aperture with less number of sub-apertures is much easier to fabricate. One may concern about the light efficiency in the inner-blocked configuration, which will be discussed later.

For a given number of sub-apertures and a given annular factor, the modulation depth of the radial polarization is similar to that of the AziSpi, whereas the former is a little greater than the latter in most cases. In general, the performance of the radial polarization is the best from the view point of the improvement of modulation depth.

The improvement of modulation depth benefited from the inner-blocked apodization can be attributed to side-lobe shift in the anti-phase PSF. Figure 3.9 shows the normalized intensity profiles of binary phase apertures using different annular factors. As the annular factor increases, the side-lobes in transverse plane decrease and the envelope of the side-lobes moves further away from the focus. Along the axial direction, the amplitudes of the side-lobes change very little, but the profiles are broadened are shifted further away, when the annular factor increases. All these changes reduce the intensity of the anti-phase PSF in the focal volume, and thus decrease the anti-phase signal and improve the modulation depth.

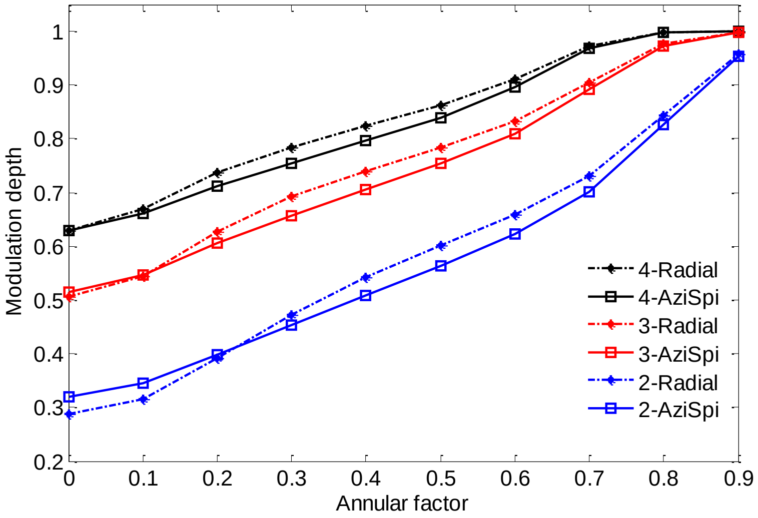

Figure 3.8 The modulation depth of FMM with different annular factors using 2- (blue), 3- (red) and 4- (black) sub-apertures for radial polarization (dashed star, Radial) and AziSpi (solid square, Azi-Spi).

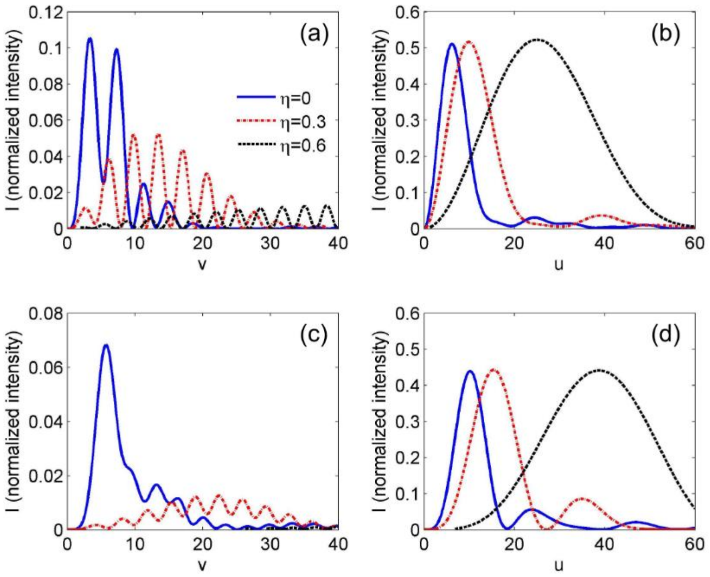

Figure 3.9 Normalized intensity profiles of binary phase apertures with 2 sub-apertures for AziSpi ((a) and (b)), and 3 sub-apertures for radial polarization ((c) and (d)), with the annular factors 0 (blue), 0.3 (red) and 0.6 (black).

There is no significant difference between the radial polarizationt and AziSpi when we investigated effects of inner-blocked apodization on the intensity distribution. The apodization enlarges the volume of the ‘flat crater’ by shifting the side-lobes far away from the focus, and this is little affected by polarization.

3.5.3 Strehl ratio

Here we define the ratio of the focal intensities of the in-phase PSF with the apodization and that without aposization as the Strehl ratio, which is a measure of the energy efficiency in the apodization rather than its usual application of evaluating the quality of image formation [128]. If the points on the aperture contribute equally to the focus, the relationship of the Strehl ratio and the annular factor would be parabolic, as the green line shown in Figure 3.10. The Strehl ratio is less than the parabolic values in most cases in Figure 3.10, which means the outer part of the aperture contributes less to the focal intensity. With small NA and small annular factor, the Strehl ratio of the radial polarization is greater than the parabolic values, because the peak of the PSF without apodization locates away from the origin.

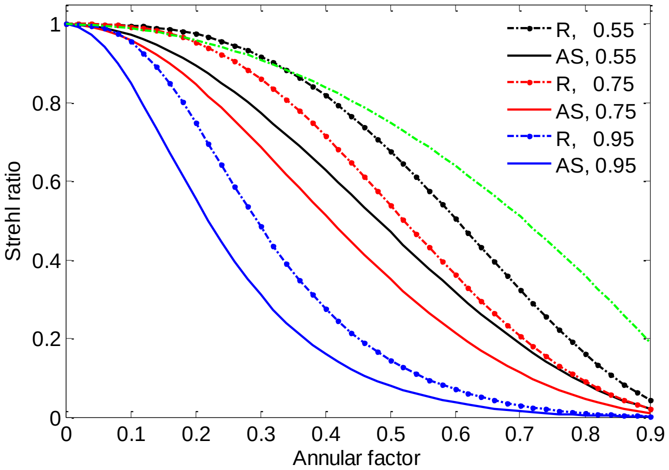

Figure 3.10 The Strehl ratio of radial polarization (dot-dashed lines, R) and AziSpi (solid lines, AS) using different annular factors with NA of 0.55 (black), 0.75 (red) and 0.95 (blue). The parabolic profile due to the annular factor is also shown (green).

For a given NA, the Strehl ratio of the AziSpi decays more quickly than that of the radial polarization when the annular factor increases, which means in the former case the outer aperture contributes less to the focal intensity than in the latter case. Thus, the apodization is more preferred in the radial polarization when the energy efficiency is more of concern.

3.5.4 Focusing efficiency

In an aplantic imaging system, the focused power is proportional to [59, 129]

$$W_{total} = \int \left| \sqrt{c} T\left(c\right) \right|^2 dc = c_{inner}^2 - c_{outer}^2, \tag{3-31}$$

where *T(c)* is the transmission function, c_{inner} and c_{outer} are corresponding to the inner-blocked and outer radii with the expression of $c = \cos\theta$. The normalized power efficiency can be defined as

$$F_{power} = \frac{I_{focus}}{2W_{total}}, \tag{3-32}$$

where I_{focus} is the normalized intensity at the focus which is unity for a free aperture of $\alpha = \pi/2$ with linearly polarized illumination. With the factor $1/2$ in Eq. (3-32), the total normalized power efficiency (electric and magnetic) at the focus for $\alpha = \pi/2$ ($NA = 1$) is unity for linearly polarized illumination with free aperture. The power efficiencies of $NA = 0.95,\ 0.75,\ 0.55$ for linear polarization are 0.42, 0.25 and 0.13, respectively.

Figure 3.11 shows the power efficiencies using different annular factors. For a given NA, the power efficiencies are less than the corresponding values in linear polarization, which means the power of linearly polarized light can be concentrated to the focus more efficiently. For AziSpi, the power efficiency decays monotonically as the annular factor increases. The same trend appears in the radial polarization when the NA is small. As the NA increases to 0.95, the power efficiency reaches a peak of 0.28 at the location $\eta = 0.16$.

The power efficiency of AziSpi is always greater than that of the radial polarization when NA is small, whereas the latter becomes greater when NA reaches 0.95 with proper apodization ($\eta > 0.11$). Thus, the radial polarization benefits more from high NA and the inner-blocked apodization.

In addition, the power efficiency increases in general as the NA increases, which means, as expected, a high NA can concentrate more power to the focus.

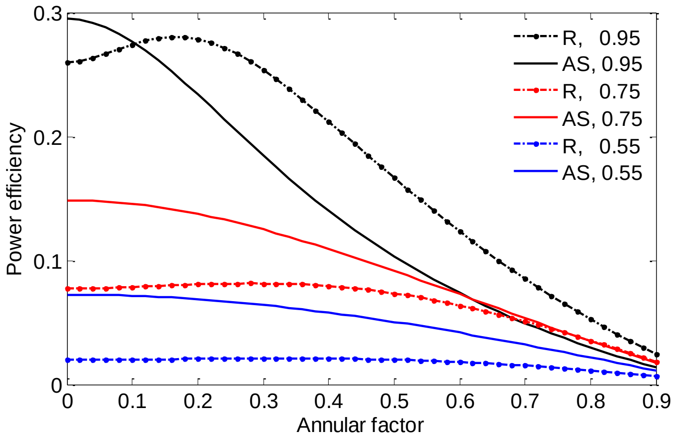

Figure 3.11 The power efficiency of radial polarization (dot-dashed lines, R) and AziSpi (solid lines, AS) using different annular factors with NA of 0.95 (black), 0.75 (red) and 0.55 (blue).

In a high NA system, the integral of the intensity in the focal plane is not proportional to the power across the focal plane [59, 129]. The integral of the intensity is proportional to

$$I_{total} = \int |T(c)|^2 \, dc = c_{inner} - c_{outer}, \tag{3-33}$$

where the parameters have the same definition as in Eq. (3-31). The normalized intensity efficiency can be defined simply as

$$F_i = \frac{I_{focus}}{I_{total}}, \tag{3-34}$$

and this is unity for a free aperture of $\alpha = \pi/2$ with linearly polarized illumination. The intensity efficiencies of $NA = 0.95,\ 0.75,\ 0.55$ for linear polarization are 1.10, 0.83 and 0.49, respectively.

Figure 3.12 shows the intensity efficiencies using different annular factors. Similar to power efficiency, the intensity efficiencies are less than the corresponding values in linear polarization for a given NA, which means the energy of linearly polarized light is distributed more at the focus. Thus, the side-lobes on the focal plane in the radial polarization and AziSpi contain more energy than that in the linear polarization, though the former have narrower main-lobes.

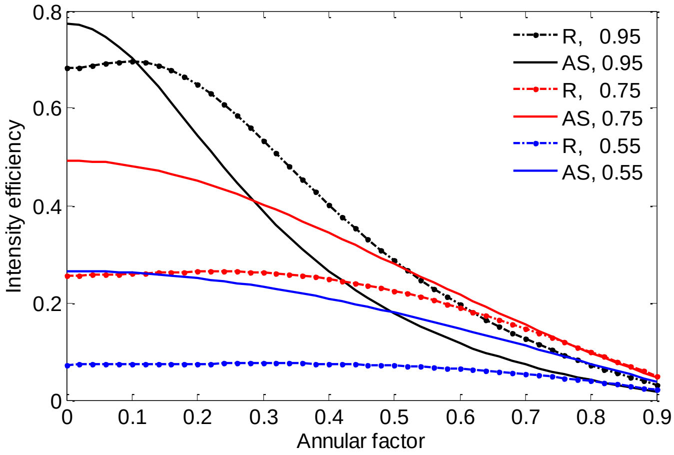

Figure 3.12 The intensity efficiency of radial polarization (dot-dashed lines, R) and AziSpi (solid lines, AS) using different annular factors with NA of 0.95 (black), 0.75 (red) and 0.55 (blue).

The relationship of the intensity efficiency and the annular factor and the NA is similar to that of power efficiency. However, the intensity efficiency of AziSpi with $NA = 0.95$ decays so quickly that it is less than the intensity efficiency with low NA when the annular factor increases to a certain level ($\eta > 0.28$ for $NA = 0.75$, $\eta > 0.50$ for $NA = 0.55$). For the radial polarization with $NA = 0.95$, the intensity efficiency reaches a peak of 0.70 at the location $\eta = 0.10$.

3.5.5 Discussion

In a high NA imaging system with considerable annular factor in the inner-blocked apodization, radial polarization performs better in Strehl ratio and light efficiency than AziSpi, and the former performs as well as the latter in resolution improvement when the annular factor is large. On the other hand, AziSpi has relatively better performance in Strehl ratio and light efficiency in the low NA system, and the resolution is little affected by NA if measured in optical coordinates. As for the modulation depth, radial polarization and AziSpi behave very similar when given the same number of sub-apertures and annular factor.

In a high NA FMM system, the incident light in the outer part of the aperture propagates through longer path length than the light in the inner part, so the former decays more due to absorption and scattering before reaching the focus. The effective illumination will be nonuniform but approximately as a Gaussian beam when the incident light is uniform. Thus, the modulation depth of the radial polarization will degrades because the Gaussian beam effectively decreases the NA. One solution is to compensate for absorption and scattering by applying nonuniform illumination, e.g. Bessel–Gauss beam [125]. Another one is to employ an inner-blocked apodization with a large annular factor, so only the light in the outer part of the aperture, which is approximately uniform, is focused. The latter solution also provides improved resolution and modulation depth, although it sacrifices more light efficiency. From this point of view, AziSpi performs better than radial polarization since it is not affected much by NA.

In general, the inner-blocked apodization improves the performance, e.g. modulation depth and resolution, of annular apertures in FMM by sacrificing light efficiency. However, this apodization may not be universally benefited for other configurations of apertures. For example, in the fan-shaped aperture (Figure 3.13 (a)), which was already used in FMM [20], the modulation depth decays as the annular factor of the inner-blocked apodization increases (Figure 3.13 (b)). In this configuration, the apodization enhances the side-lobes of the anti-phase PSF and shifts them close to the focal point (Figure 3.13 (c) and (d)), so the anti-phase signal creases and thus the modulation depth degrades. Here the simulation parameters are the same as in the scalar case in section 2.4.3 for convenience.

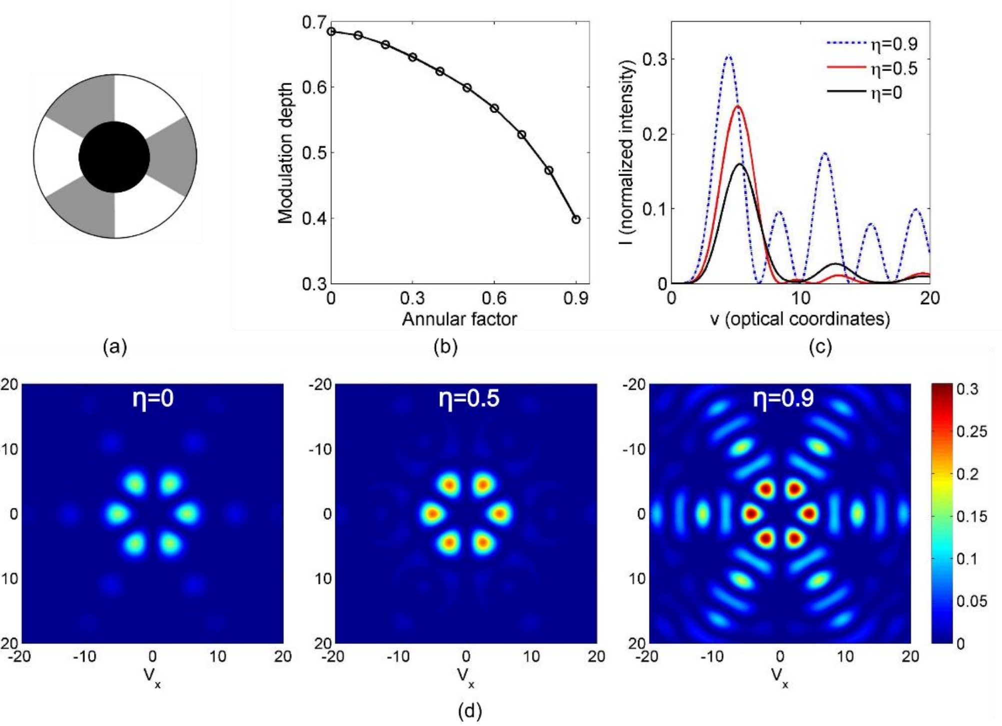

Figure 3.13 (a) An inner-blocked fan-shaped aperture with 6 sub-apertures. (b) Modulation depth of fan-shaped aperture with different annular factors. (c) Normalized intensity profiles of anti-phase PSF. (d) Normalized transverse intensity distribution of anti-phase PSF.

3.6 Conclusion

In this chapter, the representations of field in the focal region for different polarizations are derived, and then expressed in a 1D integral, which is convenient to implement calculation and define pupil moment. Then we investigated the performance of circular and radial polarizations and AziSpi used in FMM, where the annular phase apertures were optimized by MFC. The energy in the circular polarization is pushed further away than the other polarizations in the transverse plane, which leads to less anti-phase signal and thus larger modulation depth. The AziSpi gives the best resolution for any given NA; whereas the radial polarization provides better resolution than linear and circular polarizations only in the high NA system.

The effects of inner-blocked apodization were investigated by comparing the resolution, modulation depth, Strehl ratio and focusing efficiency. Radial polarization performs better in Strehl ratio and light efficiency than AziSpi only in a high NA system with considerable annular factors. On the other hand, the modulation depth and resolution of AziSpi are affected very little by NA, which makes it robust in practical implementation. In general, for radial polarization and AziSpi, both the modulation depth and resolution are improved by the inner-blocked apodization, especially when the annular factor increases. Thus, a proper inner-blocked apodization could simplify the aperture design by sacrificing light efficiency. It is noted that the apodization must be applied carefully for different configurations of the apertures. For example, the inner-blocked apodization degrades the modulation depth of fan-shaped apertures.

Chapter 4

Diverse structured-illumination imaging

4.1 Introduction

Wide-field optical microscopy is efficient and robust for imaging dynamic real-time process, but it has no depth sectioning capability due to lack of axial high frequency components in the 3D optical transfer function (OTF). Thus, a stack of wide-field images is not real 3D image but every slice contains out-of-focus background. To overcome this limitation, HiLo microscopy uses one more image with structured illumination to introduce sectioning capability. Rather than rejecting the out-of-focus photons in HiLo approach, here we apply diverse imaging approach to reconstruct images from the structured-illumination images by rearranging the photons to the emission origins, which utilizes the photons more efficiently. Furthermore, sparsity priors of the sample were incorporated in the reconstruction process to improve the sectioning capability and image fidelity.

4.2 Diverse imaging with sparsity priors

Diversity scheme has been widely used in telecommunications to alleviate signal fading by using multiple antenna channels with different characteristics [130-133]. In general, diverse imaging can be defined as that satisfying the following conditions [22]:

1) Measure an object with two or more imaging systems which have different input-output relationship.
2) The multiple imaging systems must provide different information of the object, e.g. different frequency components.
3) Exploit the persistence of the unknown information among the raw images by

signal processing and/or statistical tools to recover the desired image.

For most microscopy technologies, the imaging process can be approximated as linear and shift invariant. We denote the object as a function of position $f(\mathbf{r})$ and its optical images as $g_j(\mathbf{r})$ ($j = 1,\ldots,N$), where N images are obtained via different imaging systems with its point spread function (PSF) $h_j(\mathbf{r})$. Mathematically, the image is the convolution of the object and the PSF,

$$g_j(\mathbf{r}) = f(\mathbf{r}) \otimes h_j(\mathbf{r}). \tag{4-1}$$

Thus, the object estimate f_r can be obtained by combining the diverse images by [1]

$$f_r = \arg\min_f \sum_j \alpha_j \left\| g_j - f \otimes h_j \right\|^2 + \beta \Phi(f), \tag{4-2}$$

where the position vector **r** is omitted for convenience, α_j is weight factor denoting the confidence of the corresponding imaging, β is the regularization coefficient which is usually determined by *ad hoc* knowledge or is optimized empirically, and $\Phi(f)$ is the regularization function.

The most commonly used regularization function is the Tikhonov function, which prefers the solutions with smaller norms:

$$Tikhonov = \sum_i \left\| f(\mathbf{r}) \right\|^2, \tag{4-3}$$

where the subscript *i* denotes the pixel numbers. Sparsity priors have been widely used in compressive sensing to recover information from undersampled data [23, 91]. However, sparsity priors are also applicable when there are abundant measurements, but the signal is degraded by noise and low- or band-pass filters. With the help of sparsity priors, diverse imaging often results in better reconstruction fidelity. Here we applied total variation (TV) as the regularization representing sparsity. TV is evaluated

---

[1] Most recently, another diverse imaging modality using expectation maximization was proposed by *M. Ingaramo, et al, ChemPhysChem 15, 794-800 (2014).*

by

$$TV = \sum_i \sqrt{\left[\nabla_i^x f(\mathbf{r})\right]^2 + \left[\nabla_i^y f(\mathbf{r})\right]^2 + \left[\nabla_i^z f(\mathbf{r})\right]^2}. \tag{4-4}$$

TV represents sparsity for a piece-wise constant image, so a good reconstruction is expected for such an object. In both numerical reconstruction and experiments in this thesis, all the images are considered piecewise constant when TV is applied. The algorithm TwIST [134] was used to solve Eq. (4-2) for TV regularization. When we employed the Tikhonov regularization, in principle we could solve this convex problem analytically. However, the resulting matrix in 3D simulation is too huge to be manipulated in our work station. Thus we used Landweber algorithm [135] to solve this problem.

4.3 Mathematical model of structured-illumination imaging

In a structured-illumination imaging system based on wide-field fluorescence microscope, the emission intensity is proportional to the product of excitation illumination and the density of fluorescent sample [36, 136], where the latter is the object for recovery. Thus, the imaging process in Eq. (4-1) requires modification to reveal the property of the illumination. For a sample $f(x,y,z)$ located at the axial position z_0, the emission intensities corresponding to uniform and structured illuminations are described by

$$F_u(x,y,z,z_0) = f(x,y,z,z_0) \times I_u(x,y,z), \tag{4-5}$$

$$F_s(x,y,z,z_0) = f(x,y,z,z_0) \times I_s(x,y,z), \tag{4-6}$$

where $I_u(x,y,z)$ and $I_s(x,y,z)$ are the intensity distributions of the uniform and structured illuminations, respectively, and $I_{u,s}(x,y,z) = \left|E_{u,s}(x,y,z)\right|^2$ with the electric field in 3D space calculated by Fresnel propagation [137]

$$E_{u,s}\left(x,y,z\right)=\frac{\exp\left(ik_i z\right)}{i\lambda_i z}\iint E_{u,s}^{o}\exp\left[\frac{ik_i}{2z}\left(\left(x-\xi\right)^2+\left(y-\eta\right)^2\right)\right]d\xi d\eta, \quad (4\text{-}7)$$

where k_i and λ_i are wave number and wavelength of the illumination light, respectively. Normally we can assume the fields of uniform and structured illuminations at the object plane $\left(\xi,\eta\right)$ are unity and sinusoid, respectively, i.e. $E_u^o=1$, $E_u^o=\left(1+\cos\left(k_g\xi\right)\right)/2$, where k_g is the spatial frequency of the structured illumination.

The intensities of measured images for uniform and structured illuminations can be expressed as

$$g_u\left(x,y,z_0\right)=\left[F_u\left(x,y,z,z_0\right)\otimes h\left(x,y,z\right)\right]|_{z=0}, \quad (4\text{-}8)$$

$$g_s\left(x,y,z_0\right)=\left[F_s\left(x,y,z,z_0\right)\otimes h\left(x,y,z\right)\right]|_{z=0}, \quad (4\text{-}9)$$

where the 3D convolution is implemented first, and then the results on the focal plane ($z=0$) is selected to form a 2D image as measured. The intensity PSF $h\left(x,y,z\right)$ can be calculated by square of Eq. (2-8) for low NA, or by Eq. (2-21) for high NA, with the wavelength of emission light. The full 3D image stacks is obtained by moving the object in axial direction. This imaging process can be used to substitute for Eq. (4-1) to implement the diverse imaging shown in Eq. (4-2). Here the image formation model does not account for the multiple-scattering background light, which is often considered as low frequency and thus eliminated by image preprocessing in many cases.

4.4 Reconstruction fidelity

To study the performance of the diverse imaging reconstruction with sparsity priors, we compared different reconstruction schemes: HiLo reconstruction [21], single image reconstruction (only one image corresponding to uniform illumination) with Tikhonov and TV regularizations, and diverse imaging reconstruction (two images corresponding to uniform and structured illuminations, respectively) with Tikhonov and TV regularizations. We used a spoke-wheel as the object in the simulation (Figure 4.1 (a)). Figure 4.1 (b) shows cross-sections of the object in *x-z* and *x-y* plane. The thickness (*y*-axis) of the spoke-wheel is 8 µm, the inner and outer radii of the wheel are 4 µm and 6 µm, respectively, and the thickness of the spoke is 1.6 µm. The transverse and axial pixel sizes are 0.2 µm and 0.4 µm, respectively. The wavelengths of the excitation light and emission light are 488nm and 530nm, respectively. The NA of the collection objective lens is 0.5. The spatial frequency of the structured illumination is 600 *line pairs / mm*, if not specified. We added Gaussian noise with signal-to-noise ratio (SNR) of 20dB to the simulated raw images, which are shown in Figure 4.1 (c) and (d).

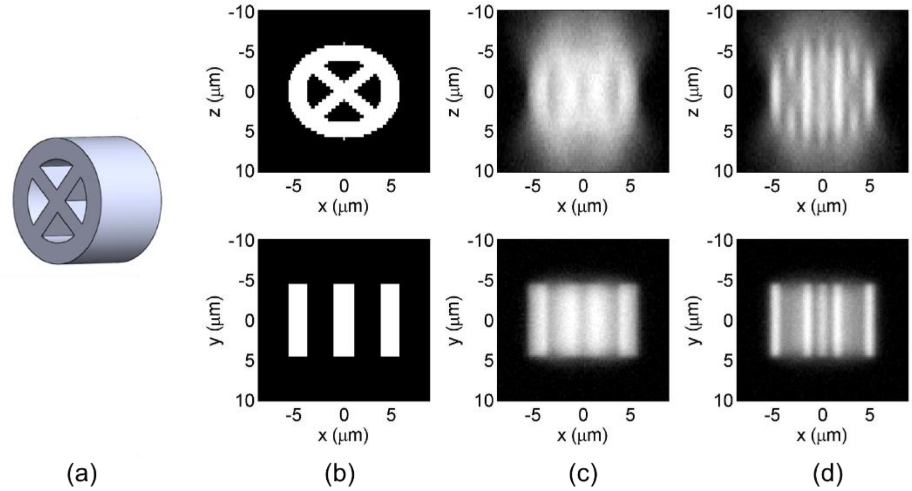

Figure 4.1 The object (a) used in simulation and its cross-sections in x-z and x-y plane (b). The images corresponding to uniform (c) and structured (d) illuminations.

4.4.1 Comparison of single image and diverse imaging reconstructions

Figure 4.2 shows the image reconstructed by HiLo algorithm, where the out-of-focus background is partly rejected. However, there is still significant residual background, because the HiLo algorithm only utilizes low-frequency components of the structured-illumination image which is not sufficient to reject background for such an object with fine structures. In addition, the effect of PSF elongation in axial direction is not considered in HiLo reconstruction, so the hub in the reconstructed image looks darker than adjacent regions where a lot of photons come from the spoke rods. This phenomenon makes the observer confused if there are two hubs in the center. The effect of PSF elongation may result in artefacts in HiLo reconstruction.

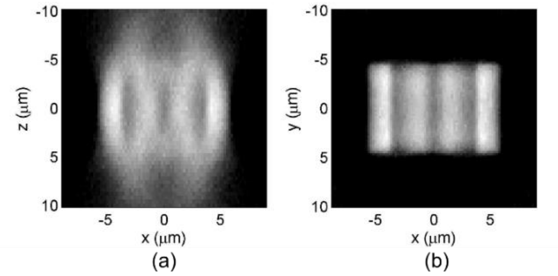

(a) (b)

Figure 4.2 Image reconstructed by HiLo algorithm.

The image reconstruction can be improved by proper utility of sparsity priors, which can be verified by comparison of Figure 4.3 (a) and (b) where the images are obtained by single image reconstruction. There is significant noise in the Tikhonov reconstruction, while the image is very smooth in the TV reconstruction. However, the central region in the hub is still missed in both reconstructions, which is attributed to the ‘missing cone’ (Figure 1.1 (a)) problem in wide-field imaging. The inverse reconstruction approach can rearrange most of the out-of-focus photons back to their origins, but normally they cannot completely recover the frequency components in the ‘missing cone’ region. Similar to compressive sensing recovery from incomplete data, here TV regularization challenges the ‘missing cone’, as the missed intensity in the central hub in TV reconstruction is less than that in Tikhonov construction. However, it is far from sufficient to recover ‘missing cone’ with only uniform illumination image. Here the missing of central hub is different from the darkness of central hub in Figure 4.2, which can be discriminated by comparing the width of the hub to the original object. The sparsity priors, i.e. TV regularization here, can suppress the noise effectively, but it cannot restore the missed frequency components in axial axis in wide-field imaging.

The structured-illumination data provides the missed frequency components, so the hub in the simulation can be well reconstructed by using the uniform and structured illumination data (Figure 4.3 (c) and (d)). Again, the reconstructed image with TV regularization is smoother and of much less noise than Tikhonov reconstruction. Comparison of Figure 4.3 (b) and (d) demonstrates that the diverse imaging improves the performance of reconstruction, especially the sectioning capability.

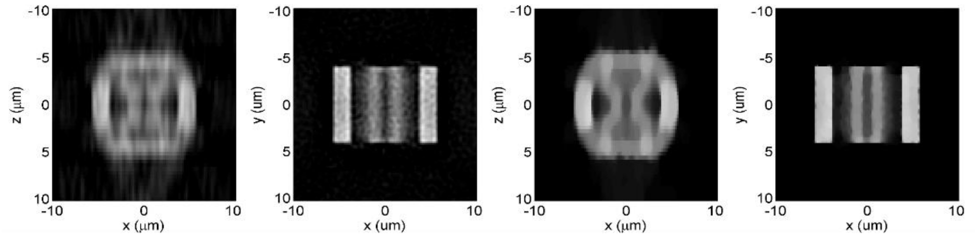

(a) Tikhonov, Uni (b) TV, Uni

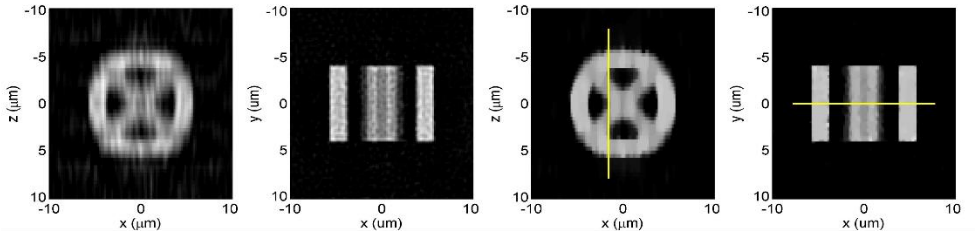

(c) Tikhonov, Uni + Str (d) TV, Uni + Str

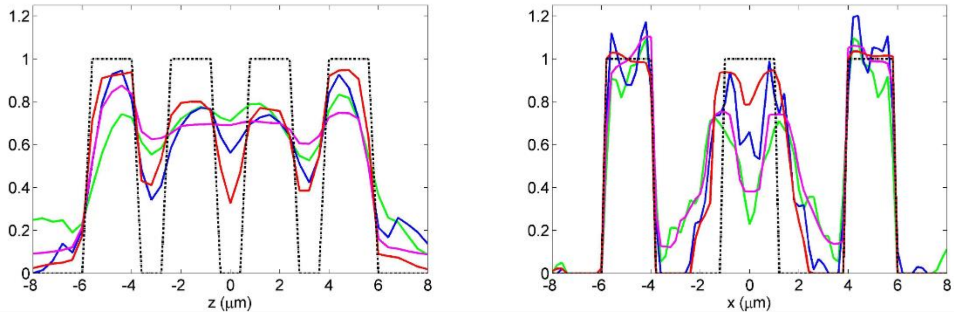

(e) Axial direction (f) Transverse direction

Figure 4.3 Images reconstructed by only uniform illumination data (Uni) with (a) Tikhonov (Tik, green) and (b) TV (magenta) regularizations, and diverse imaging by uniform and structured illumination data (Uni + Str) with (c) Tikhonov (Tik, blue) and (d) TV (red) regularizations. Normalized line profiles at position of the yellow lines in Figure (d) in (e) axial and (f) transverse directions, where the black dashed lines denote the profiles of the object.

Figure 4.3 (e) and (f) show the normalized line profiles at position of the yellow lines in Figure 4.3 (d) in axial and transverse directions, respectively, where the difference between different reconstruction schemes can be revealed in detail. Along axial direction, the two spokes in the middle can be resolved by diverse imaging, while the TV reconstruction (red line) performs much better contrast than Tikhonov reconstruction (blue line). On the other hand, they cannot be resolved in the single image reconstruction with either TV (magenta line) or Tikhonov (green line) regularization, although the TV regularization smoothes the profile. In the transverse direction (Figure 4.3 (f)), the hub reconstructed by diverse imaging with TV regularization is the closest to the profile of original object. The central point in the hub is darker than adjacent points in all the reconstruction schemes, because the missed frequency components are not fully compensated by the structured illumination data in this simulation. It is expected to completely correct the 'missing cone' problem by a structured illumination with higher spatial frequency and/or more structured illuminations in different directions. If we use the contrast in the hub to evaluate the reconstruction performance, the diverse imaging is better than single image reconstruction, and the TV reconstruction is better than Tikhonov reconstruction. Thus, the diverse imaging with TV regularization performs the best.

4.4.2 Effect of contrast of the structured illumination

In practice, the contrast of the structured illumination is usually degraded by strong scattering in imaging thick samples. If the contrast is very low, the structured illumination will be approximately equivalent to the uniform one and hence fail to provide high frequency information. Thus, it is crucial to investigate the influence of the contrast in diverse imaging scheme. The relative mean square error (MSE) is used to quantify the effects. The MSE is given by

$$MSE = \frac{\sum_i \left\| f_r(\mathbf{r}) - f_o(\mathbf{r}) \right\|^2}{\sum_i \left\| f_o(\mathbf{r}) \right\|^2}, \tag{4-10}$$

where the subscript *i* denotes the pixel number, $f_r(\mathbf{r})$ and $f_o(\mathbf{r})$ are the reconstructed image and the original objects, respectively.

Figure 4.4 shows the MSE of diverse imaging using structured illuminations of different contrasts. The MSE decreases as the contrast of the structured illumination increases, and TV reconstruction generally performs better than Tikhonov approach. For TV reconstruction, the MSE is greater than 20% for the contrast no more than 0.4, it is less than 13% for the contrast no less than 0.8, and at the contrast 0.6 the MSE fluctuates across 13% and 20%. Thus, the value 0.6 can be considered as a threshold of contrast.

In addition, the variance of MSE in TV regularization is larger than Tikhonov regularization for a given NA, because an iterative algorithm TwIST [134] was employed to solve this non-convex inverse problem. On the other hand, the solution of Tikhonov regularization essentially corresponds to a unique result which can be obtained explicitly [22], although TwIST was used in our simulation due to huge matrices in 3D calculation.

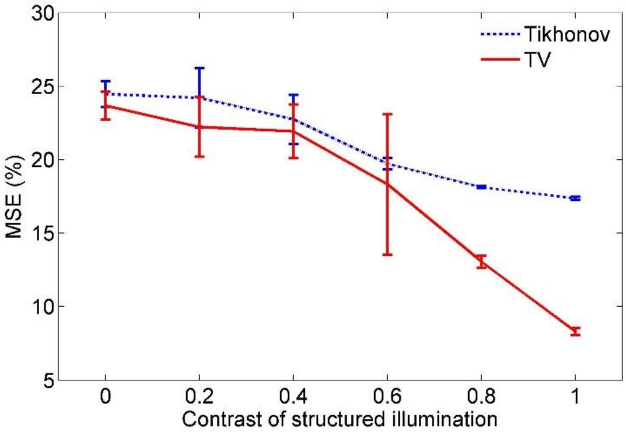

Figure 4.4 The MSE of diverse imaging using structured illuminations of different contrasts.

To visually evaluate the performance of diverse imaging around the threshold, Figure 4.5 compares the images reconstructed by Tikhonov and TV regularizations, where the contrasts of the structured illumination are 0.4 (upper figures) and 0.8 (bottom figures). The central part of the hub is missed in both Tikhonov and TV reconstructions when the contrast is 0.4, while it is well recovered when the contrast is

0.8. For the TV reconstruction, the capability of noise suppression is also improved when the contrast increases.

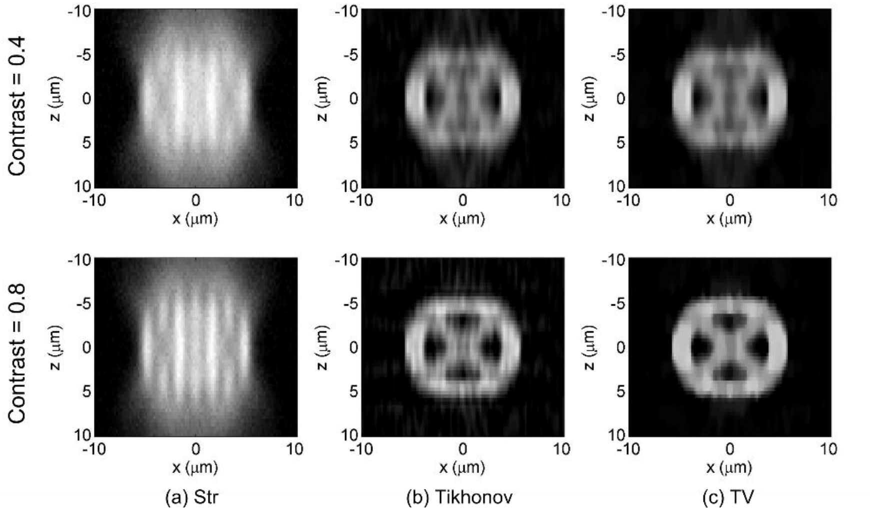

Figure 4.5 Raw structured illumination data (a) and Images reconstructed by diverse imaging with Tikhonov (b) and TV (c) regularizations, where the contrasts of the structured illumination are 0.4 (upper) and 0.8 (bottom).

4.4.3 Effect of frequency of the structured illumination

The spatial frequency of the structured illumination determines how much frequency components in the 'missing cone' can be compensated, so it affects the sectioning capability of diverse imaging. Figure 4.6 shows the MSE of diverse imaging using structured illuminations of different spatial frequencies, where the mean values for different frequencies are similar for the same reconstruction scheme. However, the frequency 500 *line pairs / mm*, where the fluctuation of the MSE is much larger than other frequencies, may be considered as a threshold.

Figure 4.7 (a) and (b) show images reconstructed by diverse imaging with the frequency of 200 *line pairs / mm*. For the TV reconstruction, although the image looks piecewise smooth, it is not as uniform as the image reconstructed with the frequency of 600 *line pairs / mm* (Figure 4.3 (d)). This phenomenon is consistent with comparison of their MSE values.

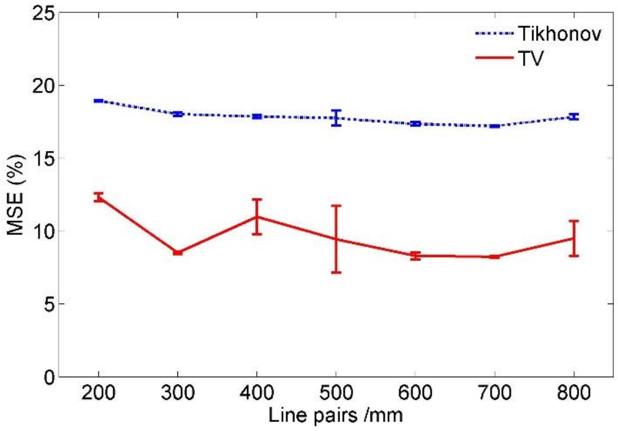

Figure 4.6 The MSE of diverse imaging using structured illuminations of different spatial frequencies.

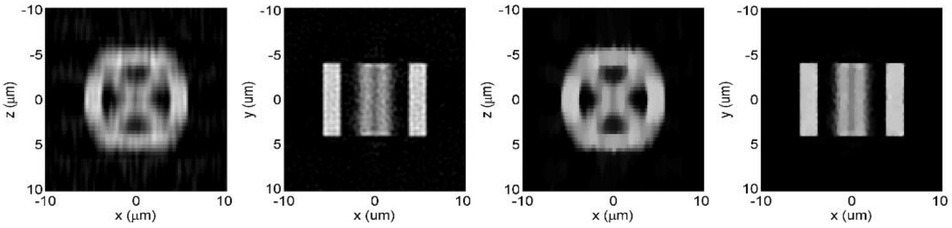

(a) Tikhonov

(b) TV

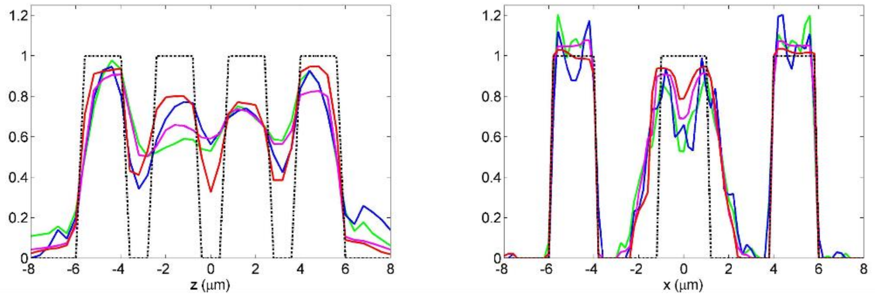

(c) Axial direction

(d) Transverse direction

Figure 4.7 Images reconstructed by diverse imaging with (a) Tikhonov (green) and (b) TV (magenta) regularizations, where the frequency of the structured illumination is 200 line pairs / mm. Normalized line profiles at position of the yellow lines in Figure 4.3 (d) along (c) axial and (d) transverse directions, where the blue and red lines denote reconstructions using structured illumination data with frequency 600 line pairs / mm by Tikhonov and TV regularizations, respectively.

Figure 4.7 (c) and (d) compare the normalized line profiles at position of the yellow lines in Figure 4.3 (d) in axial and transverse directions, respectively. In the axial direction, the two spokes in the middle can be resolved by diverse imaging with the frequency of 600 line pairs /mm, while the TV reconstruction (red line) performs much better contrast than Tikhonov reconstruction (blue line). On the other hand, they cannot be resolved in the single image reconstruction with either TV (magenta line) or Tikhonov (green line) regularization, though the TV regularization smoothes the profile.

4.5 Resolution

The structured illumination data includes high frequency information by shifting the frequency components in transverse direction, so the transverse resolution is expected to be improved by proper reconstruction. To recover the high frequency components, usually more than one structured illumination raw images are required to shift the high frequency components back to their original positions in Fourier space, e.g. reconstruction by Wiener filter in conventional SIM [9]. As for HiLo microscopy, the high frequency components cannot be identified by one structured illumination raw image, so they are filtered out and only low frequency components are left for compensating for the ‘missing cone’ [21]. Thus, the resolution of HiLo microscopy remains the same as the wide-field microscopy, but only the sectioning capability is obtained. However, as the reconstruction is considered as an inverse problem in diverse imaging, it is possible to restore the high frequency components with only one structured illumination raw data.

To study the resolution of diverse imaging, a spoke-wheel object with 8 spokes but without the outer ring as shown in Figure 4.8 was used in simulation. The radius of the spoke-wheel is 1.5 µm, and its thickness (*z*-axis) is 5 µm. The transverse and axial pixel sizes are 0.025 µm and 0.5 µm, respectively. The wavelengths of the excitation light and emission light are 488nm and 530nm, respectively. The NA of the collection objective lens is 0.5. The spatial frequency of the structured illumination is 800 *line pairs / mm*. Noise was added to the simulated images with SNR of 20dB.

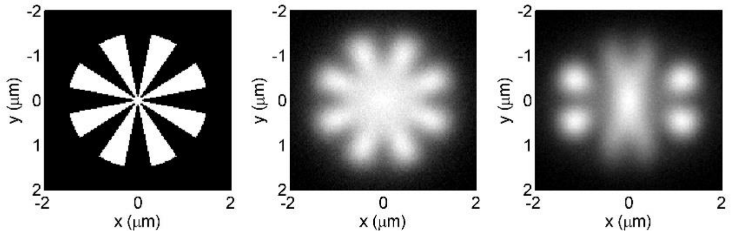

Figure 4.8 The object (left) used in simulation, and the raw images with uniform (middle) and structured (right) illumination.

Figure 4.9 shows the images reconstructed by only uniform illumination data (one image, *1i*) and by diverse imaging (*2i*), with Tikhonov and TV regularizations. In the diverse imaging results, the resolution along *x*- axis looks better than that along *y*- axis, and the latter seems similar to the reconstruction by only uniform illumination data. This phenomenon is clearer in TV reconstruction, where the width of the central hub is narrower in *x*- direction.

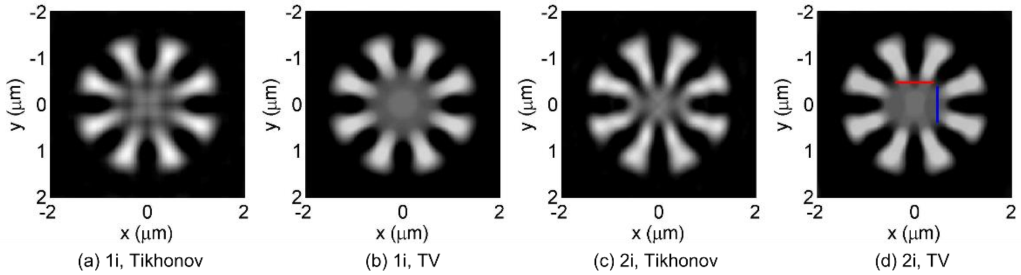

Figure 4.9 Images reconstructed by only uniform illumination data (1i) with Tikhonov (a) and TV (b) regularizations, and those reconstructed by diverse imaging (2i) with Tikhonov (a) and TV (b) regularizations.

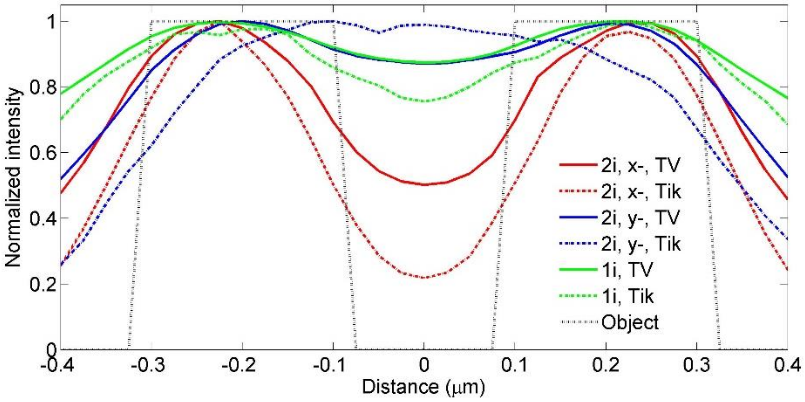

Figure 4.10 Normalized intensity line profiles at position of the red and blue lines in Figure 4.9 (d) for different reconstruction schemes. The black dashed line denotes the profile of the spoke.

To compare the resolution quantitatively, we took the resolution limit as the distance between the centers of adjacent spokes for which the ratio of the intensity at the central dip to that at the maxima of the corresponding intensity line profile is equal to one-half. This definition is different from the conventional two-point resolution [138], because the geometry of the object is different and the conventional two-point resolution is for raw image. Here the resolution limit is introduced to quantitatively compare the resolutions of different reconstruction schemes.

Figure 4.10 shows the normalized intensity line profiles for different reconstruction schemes at position of the red and blue lines in Figure 4.9 (d), where the resolution in *x*-axis of the image reconstructed by diverse imaging with TV regularization reaches the resolution limit. Obviously, only the spokes separated along *x*-axis are resolved in diverse imaging reconstruction, since only the high frequency components in Fourier domain corresponding to *x*-axis in space are included in the structured illumination data. The contrast of the image reconstructed by Tikhonov regularization is superior to that by TV regularization, as TV regularization always tries to smooth the image and thus decrease the contrast. Therefore, it is more appropriate to select different thresholds of resolution limit for evaluation of Tikhonov and TV reconstructions. On the other hand, the contrast along *y*-axis in diverse imaging reconstruction is very close to that in construction with only uniform illumination data by the same regularization, which means the resolution in *y*-axis is little affected by the structured illumination.

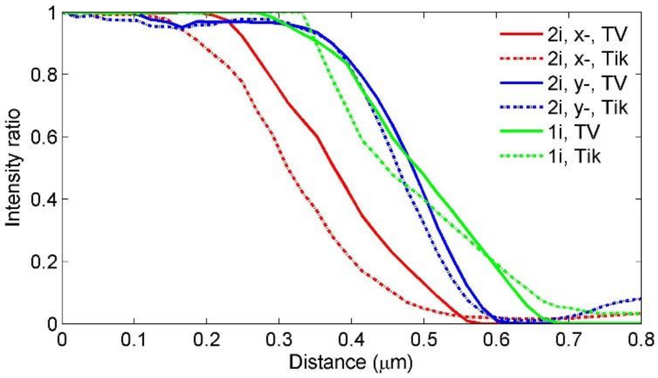

Figure 4.11 The intensity ratio of images reconstructed by different schemes with respect to the distance of adjacent spokes.

Figure 4.11 shows the intensity ratio of images reconstructed by different schemes with respect to the distance of adjacent spokes. According to the resolution limit criterion of one-half, the resolution in *x*-axis in diverse imaging with Tikhonov (0.31 µm) and TV (0.38 µm) regularizations is improved by 31% and 22%, respectively, compared to the corresponding regularizations with only uniform illumination data (0.45 µm for Tikhonov and 0.49 µm for TV). In the transition region around unity or zero, the intensity ratio in TV reconstruction changes faster than that in Tikhonov reconstruction especially in diverse imaging, which means the capability of resolving in TV reconstruction is more sensitive. TV regularization prefers a determined answer to resolving with less ambiguity, which phenomena is similar to the sparsity priors used in compressive sensing.

Furthermore, we evaluated the resolution of diverse imaging using one uniform and two perpendicular structured illumination data (three raw images in total, *3i*). Figure 4.12 shows the images reconstructed by Tikhonov and TV regularizations, where both of them are symmetric. The TV regularization not only smoothes the reconstructed image, but also eliminate the possible illusion, which can be found in the central region of the image reconstructed by Tikhonov regularization.

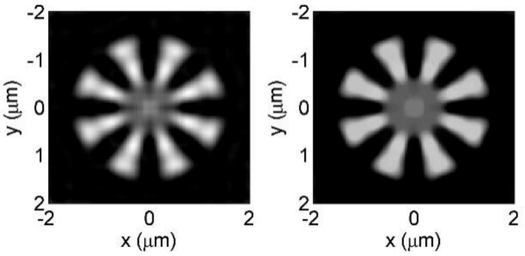

Figure 4.12 Images reconstructed by diverse imaging using one uniform and two structured illumination data with Tikhonov (left) and TV (right) regularizations.

Figure 4.13 compares the intensity ratio of reconstructed images, where the intensity ratio in diverse imaging along *x*-axis is the same as that along *y*-axis. The transition from ‘resolving’ to ‘unresolving’ in TV regularization is much sharper than that in Tikhonov regularization. As before, TV regularization prefers a determined answer to resolving, which is much significant when more than one structured illumination data are used.

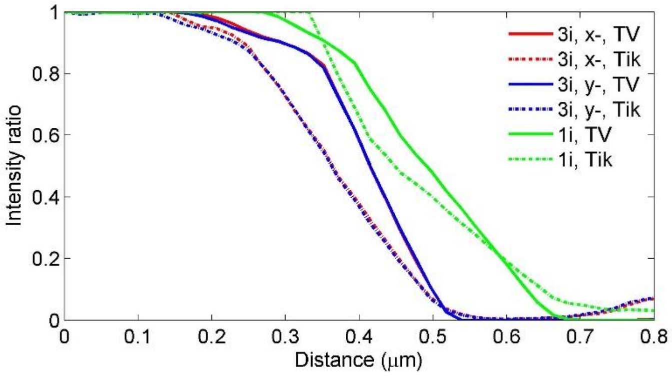

Figure 4.13 The intensity ratio of images reconstructed using only uniform illumination data (1i) and one uniform and two structured illumination data (3i) with respect to the distance of adjacent spokes.

4.6 Experiment results

The performance of the diverse imaging with TV regularization was preliminarily evaluated with wide-field images of fluorescence beads. The sample has an excitation wavelength of 480nm and an emission wavelength of 530nm. A Ronchi ruling was used to produce the structured illumination, where the resultant spatial frequency at the focal plane is 320 *line pairs / mm*. The effective pixel size on the sample is 0.266 μm, and the axial step size is 0.6 μm. The NA of the collection objective lens is 0.55. The theoretically calculated PSF was employed in diverse imaging reconstruction.

Figure 4.14 shows the raw structured illumination data and images reconstructed by HiLo algorithm and diverse imaging with TV regularization. The noise and out-of-focus background is well suppressed in TV reconstruction, and the boundary of the bead is sharp. The tilt elongation in axial axis is attributed to the error of PSF. The image quality is expected to be improved by using an accurately measured PSF in reconstruction.

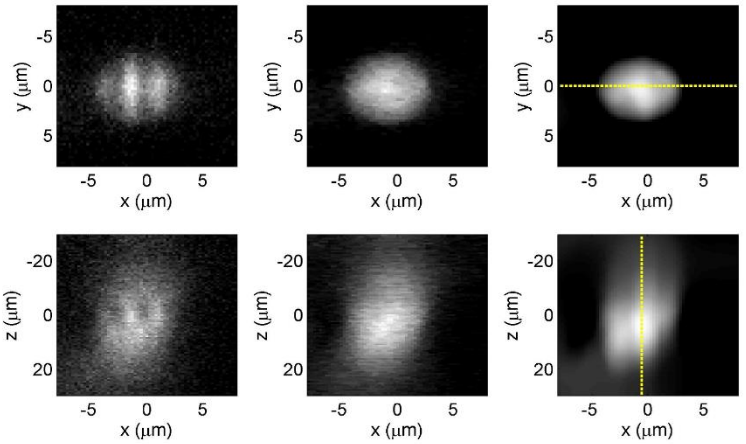

(a) Strutured illumination (b) HiLo (c) TV

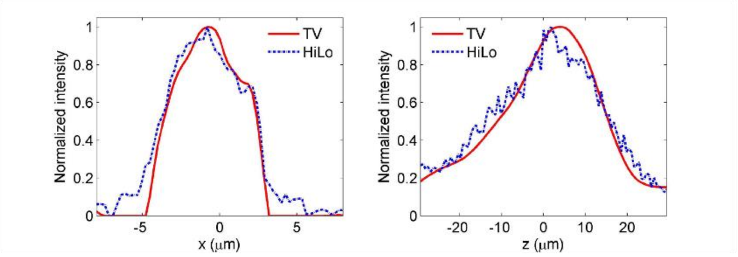

(d) Normalized intensity profiles

Figure 4.14 Structured illumination raw data (a), and images reconstructed by HiLo algorithm (b) and diverse imaging with TV regularization (c). (d) Normalized intensity profiles in transverse (left) and axial (right) directions at the position of the yellow dashed lines shown in (c).

4.7 Conclusion

In this chapter, diverse imaging with sparsity priors was introduced to reconstruct an image from two images: one with uniform illumination and the other with structured illumination. By rearranging the photons to the emission origins, diverse imaging performs much better than HiLo approach in background rejection and noise suppression. Since the high frequency components are introduced by structured illumination data to compensate for the missed components in the ‘missing cone’, the sectioning capability is well developed in diverse imaging. The image fidelity, which is evaluated by MSE and contrast, of diverse imaging is much better than single image reconstruction. The sparsity priors, i.e. TV regularization in our case, was demonstrated to further improve the reconstruction fidelity.

The effects of the contrast and spatial frequency of the structured illumination were investigated. The image quality degrades when the contrast decreases, which often happens in imaging deep in highly scattering samples. As the spatial frequency increases, the image quality is improved because of more compensation of high frequency components from the structured illumination.

The resolution in the direction perpendicular to the structured illumination fringes can be improved by diverse imaging, which is not reachable in HiLo method. However, the resolution in the other transverse direction is little improved, because the corresponding bandwidth cannot be extended by only one structured illumination image. Two perpendicular structured illuminations can help to improve the transverse resolution. Compared to Tikhonov regularization, TV reconstruction prefers a determined answer to resolving with less ambiguity.

Chapter 5

Hybrid imaging with focal modulation microscopy and wide-field microscopy

5.1 Introduction

Scanning microscopy techniques, e.g. CM, FMM and MPM, have depth sectioning ability, but they require temporal and spatial scanning which will take a long time, and thus are not very suitable for dynamic real-time imaging. If the image acquisition process is intentionally speeded up beyond its requirement, the image quality will be definitely degraded due to information loss. On the other hand, wide-field optical microscopy is efficient and robust for imaging dynamic real-time process but lack of depth sectioning capability. Therefore, if the sectioning information is still in the image captured by scanning microscopy, the other lost information may be compensated by a wide-field image. In this chapter, we proposed several hybrid imaging approaches to combine scanning microscopy with wide-field microscopy. In different modalities, the image is reconstructed by different algorithms implementing in space, or in Fourier domain, or in sequence. Specifically, we chose FMM as an example of scanning microscopy to study the performance of hybrid imaging. However, the methods can be straightforward implemented with other scanning microscopy techniques.

5.2 Hybrid imaging in spatial domain

In spatial domain, the hybrid imaging can be implemented conveniently *via* diverse imaging scheme proposed in section 4.2. Specifically, Eq. (4-2) can be rewritten as

$$f_r = \arg\min_f \left\| g_{FMM} - f \otimes h_{FMM} \right\|^2 + \eta \left\| g_{WF} - f \otimes h_{WF} \right\|^2 + \beta \Phi\left(f \right), \qquad (5\text{-}1)$$

where f and f_r denote the object and reconstructed image, respectively, g_{FMM} and g_{WF} are images obtained by FMM and wide-field microscopy, respectively, h_{FMM} and h_{WF} describe the point spread functions (PSF) of FMM and wide-field microscopy, respectively, η is the weight factor for the two images, β is the regularization coefficient, and $\Phi\left(f\right)$ is the regularization function. The wide-field PSF h_{WF} can be calculated by square of Eq. (2-8) for low NA, or by Eq. (2-21) for high NA, with the wavelength of emission light. The FMM PSF h_{FMM} is equivalent to the integrand in Eq. (2-6) with effective illumination, which can be written as

$$h_{FMM} = h_{illu}\left(x,y,z\right)\left[h_{de}\left(x,y,z\right)\otimes_2 D\left(x,y\right)\right], \tag{5-2}$$

where $\otimes_2$ denotes the 2D convolution operation, $D\left(x,y\right)$ is the sensitivity function for the pinhole detector. The effective illumination PSF h_{illu} is the difference of in-phase and anti-phase illuminations, which is dependent on the aperture design. An annular aperture of 2 sub-apertures designed by MFC (section 2.5) was used in our simulation. The detection PSF h_{de} was calculated by square of Eq. (2-8) for low NA and by Eq. (2-21) for high NA.

Consider the shot noise caused by the quantum effect of light, which is the most important source of noise when the number of detected photons is small, the relationship of signal-to-noise ratio (SNR) and the average number of photons N is given by [112]

$$SNR = \frac{N}{\sqrt{N}} = \sqrt{N}. \tag{5-3}$$

If the required SNR of FMM images can be reduced from 20 dB to 5 dB, we can decrease the number of collected photons to only $1/32$. Thus, we can speed up the image acquisition process by 32 times, given that the wide-field imaging time is negligible. Meanwhile, the wide-field images are used to improve SNR through diverse imaging scheme. Therefore, we can obtain the advantages of FMM, sectioning capability and high resolution, and the advantage of wide-field microscopy, fast imaging speed with high SNR, at the same time.

The object used in simulation is shown in Figure 5.1, which is the same as previous in Figure 4.1. The wavelengths of the excitation light and emission light are 488nm and 530nm, respectively, and for convenience we assumed the excitation wavelengths in FMM and wide-field imaging are the same. The NA of the illumination and collection objective lenses is assumed the same, with the value of 0.5 if not specified. Gaussian noise is added to the simulated raw images, with SNR 20dB for wide-field (WF) images and 5dB for FMM images.

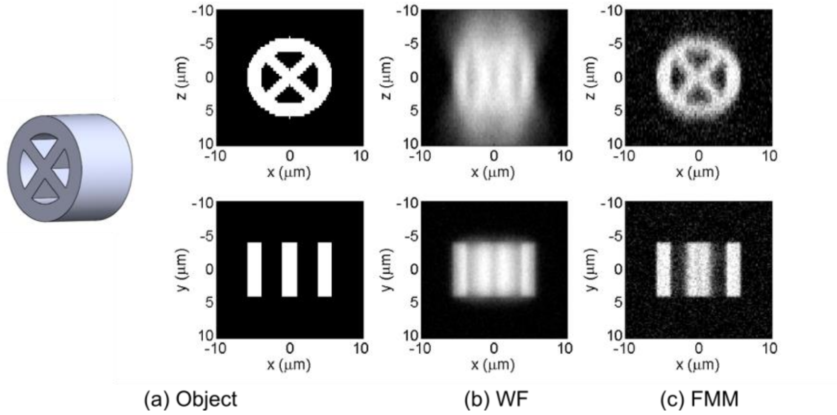

(a) Object (b) WF (c) FMM

Figure 5.1 The object used in simulation and its cross-sections in x-z and x-y plane (a). The images are corresponding to wide-field imaging (b) and FMM (c).

5.2.1 Reconstruction with Tikhonov regularization

Figure 5.2 shows the images reconstructed with Tikhonov regularization by only wide-field (a, green) and FMM (b, blue) data, and by diverse imaging (c, red). Although the image reconstructed by wide-field data has much less background than the raw image (Figure 5.1 (c)), there is significant out-of-focus background left. Furthermore, in the line profiles shown in Figure 5.2 (d), the contrast of the central two spokes in the wide-field reconstruction is significantly lower than the other two due to lower resolution in wide-field image. In addition, the central part of the hub is missed due to lack of sectioning capability.

The image reconstructed by diverse imaging looks similar to that reconstructed by

FMM data, and both of them has much less noise than the raw image (Figure 5.1 (d)). To quantify their performance, MSE was applied to evaluate the reconstruction fidelity, where the MSE is calculated by Eq. (4-10). As shown in Figure 5.3 (a), The MSE of reconstruction with diverse imaging is smaller than that with only FMM data, which demonstrates the benefit of high SNR from wide-field data. As expected, the MSE decreases as the NA increases, since the resolutions of both wide-field microscopy and FMM are improved. However, the MSEs of reconstructions with diverse imaging and only FMM change much less than the reconstruction with wide-field data. In the former case, the MSEs are mainly determined by noise (very low SNR in FMM data), so they are just less affected by the resolution of the microscopies. In the latter case, the out-of-focus background is the dominant source of MSE, so the reconstruction is remarkably improved by resolution enhancement. When the NA increases to 0.9, the MSE of reconstruction with only wide-field data is very close to that with diverse imaging. Nonetheless, the feature of the object is better covered by diverse imaging, as the joints are brighter than other parts in the image reconstructed by wide-field data (Figure 5.3 (c)). In addition, there is still residual out-of-focus background in the gap regions between spokes in the latter reconstruction.

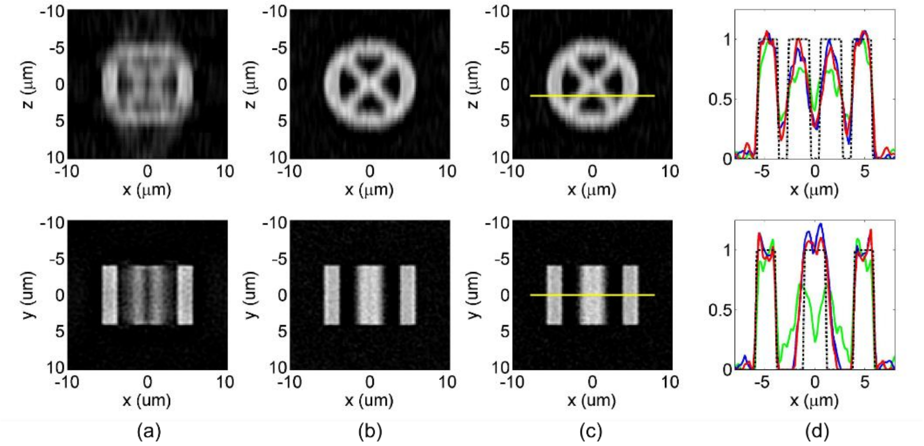

Figure 5.2 Images reconstructed using Tikhonov regularization by only wide-field (a, green) and FMM (b, blue) data, and by diverse imaging (c, red). Intensity line profiles at position of the yellow lines in (c), where the dashed line denotes the object.

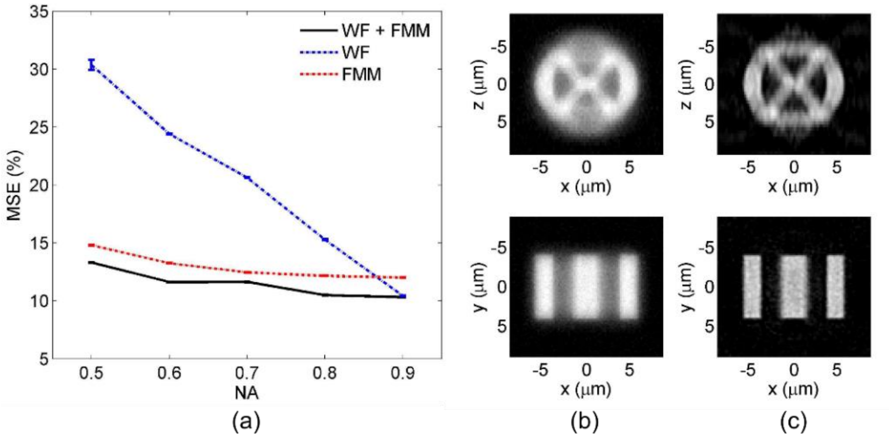

Figure 5.3 (a) The MSE of images reconstructed by diverse imaging (black solid line) and only wide-field (blue dashed line) and FMM (red dashed line) using different NA. Raw (b) and reconstructed (c) images of wide-field data with NA of 0.9.

5.2.2 Reconstruction with total variation (TV) regularization

Figure 5.4 shows the images reconstructed with TV regularization by only wide-field (a, green) and FMM (b, blue) data, and by diverse imaging (c, red). All the reconstructed images are smooth, but the contrast of the central two spokes in the image reconstructed by wide-field data is still lower than the other two, and the central part of the hub is missed.

Figure 5.5 compares the MSE of different reconstruction schemes with TV regularization. For a given NA, the MSE of reconstruction with diverse imaging is the smallest, which benefits from the capability of out-of-focus rejection in FMM and the high SNR in wide-field data. Here with TV regularization, the advantage of high SNR in wide-field data is utilized more effectively, so the MSE in diverse imaging is remarkably smaller than the reconstruction with only FMM data. Although the MSE of reconstruction with wide-field data decreases more quickly than the other two, it is always greater than the diverse imaging.

In addition, the MSE of reconstruction with wide-field data is less than that with FMM when the NA is high ($NA = 0.8,\ 0.9$). In this situations, the intensity level of noise in the low-SNR FMM raw images (Figure 5.1 (d)) is comparably greater than that of the out-of-focus background in the wide-field raw images (Figure 5.3 (b)), so the latter one is easier to be suppressed by the TV regularization.

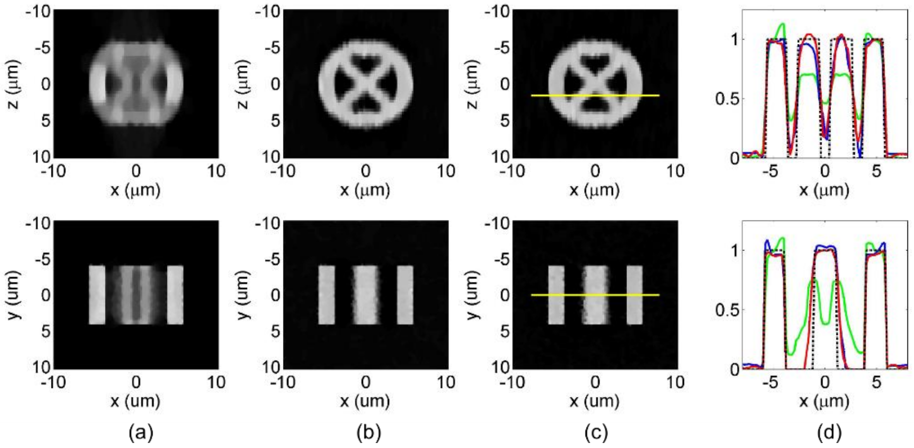

Figure 5.4 Images reconstructed with TV regularization by only wide-field (a, green) and FMM (b, blue) data, and by diverse imaging (c, red). Intensity line profiles at position of the yellow lines in (c), where the dashed line denotes the object.

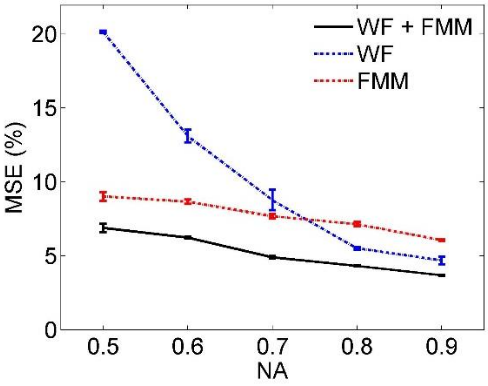

Figure 5.5 The MSE of images reconstructed by diverse imaging (black solid line) and only wide-field (blue dashed line) and FMM (red dashed line) with TV regularization using different NA.

5.2.3 Comparison of Tikhonov and TV regularizations

Figure 5.6 compares the MSE of images reconstructed by diverse imaging with Tikhonov and TV regularizations, where the MSE of the latter is remarkably less than the former one. Comparing to Tikhonov regularization, the MSE of TV regularization is reduced by 48% at $NA = 0.5$ and 64% at $NA = 0.9$, which demonstrates the benefit of proper application of sparsity priors.

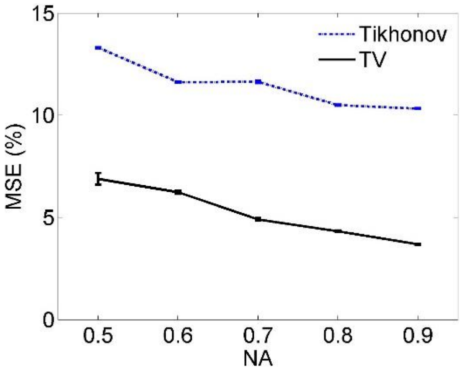

Figure 5.6 The MSE of images reconstructed by diverse imaging with Tikhonov (blue dashed line) and TV (black solid line) regularizations.

5.3 Hybrid imaging in Fourier domain

Wide-field images include not only the in-focus photon contribution, but also the out-of-focus and scattering photon contributions. The latter two types of photon contributions are usually considered as exhibiting only low frequency spatial structures [21]. Here we substitute the low frequency components of wide-field images by the corresponding frequency components of undersampled FMM images to eliminate the out-of-focus and scattering photon contributions. The benefit of this hybrid technique is that we can speed up the FMM image acquisition process by reducing the sampling rate.

In brief, the images acquired by FMM and wide-field microscopy can be written, respectively, as:

$$I_{WF}(\mathbf{r}) = I_{in}(\mathbf{r}) + I_{out}(\mathbf{r}), \tag{5-4}$$

$$I_{FMM}(\mathbf{r}) = \eta I_{in}(\mathbf{r}), \tag{5-5}$$

where $I_{in}(\mathbf{r})$ and $I_{out}(\mathbf{r})$ are the image contributions from in-focus and out-of-focus, respectively (spatial coordinates $\mathbf{r}$), and η is the weight factor of intensities due to different signal gains of FMM and wide-field microcopy systems. The low frequency components of the in-focus image can be obtained by applying a low-pass filter (LP) to $I_{FMM}(\mathbf{r})$ with a cut-off frequency smaller than the sampling rate of FMM image, i.e.

$$LP\left[I_{in}(\mathbf{r})\right] \approx LP\left[I_{FMM}(\mathbf{r})\right]. \tag{5-6}$$

As mentioned before, the out-of-focus image contribution contains only low frequency spatial structures. Therefore, with a complementary high-pass filter (HP) applied to wide-field image $I_{WF}(\mathbf{r})$ we can recover the high frequency components in $I_{in}(\mathbf{r})$,

$$HP\left[I_{in}(\mathbf{r})\right] \approx HP\left[I_{WF}(\mathbf{r})\right], \tag{5-7}$$

while $HP\left[I_{out}(\mathbf{r})\right] \approx 0$. Finally we obtain a full bandwidth representation of $I_{in}(\mathbf{r})$ by combining Eqs. (5-6) and (5-7) through

$$I_{in}(\mathbf{r}) = \frac{1}{\eta} LP\left[I_{FMM}(\mathbf{r})\right] + HP\left[I_{WF}(\mathbf{r})\right]. \tag{5-8}$$

Ideally, η can be determined by the systematic parameters, e.g. illumination intensity and pinhole size. However, here we treat it as an unknown parameter and adjust to smooth the transition from low frequency to high frequency components.

Figure 5.7 illustrates the whole process, where the Fourier transform and inverse Fourier transform can be implemented in either 2D or 3D frequency domains. In the following sub-sections we evaluate the performance of 2D and 3D manipulations, respectively.

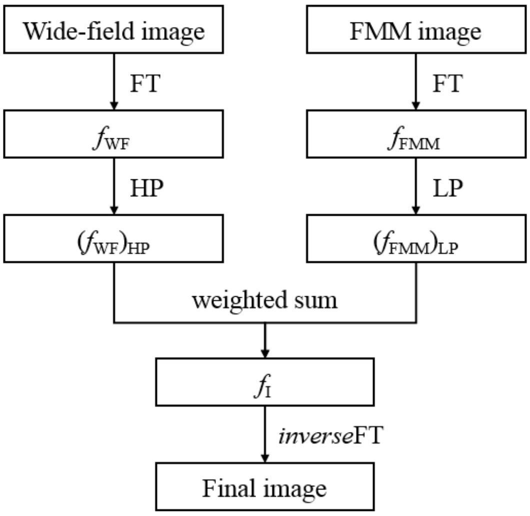

Figure 5.7 Flow chart of hybrid imaging in Fourier domain. FT represents Fourier transform, HP and LP represent high-pass and low-pass filters respectively, and f_I is Fourier transform of the final image.

5.3.1 Reconstruction in 2D Fourier domain

The images are reconstructed slice by slice to form a 3D image. We followed the process in Figure 5.7 to retrieve each slice, where the Fourier transform (FT) and inverse FT are implemented in 2D domain. The same object as in Figure 5.1 was used in simulation. The wavelengths of the excitation and emission light are 488nm and 530nm, respectively. The NA is 0.5 for both illumination and detection objective lens. The pixel size in wide-field images is $\Delta x = \Delta y = 0.1\mu m$, and the axial step size is $\Delta z = 0.2\mu m$. Gaussian noise was added to the simulated raw images with $SNR = 20dB$ for FMM images and $SNR = 30dB$ for wide-field images, if not specified.

To quantify the undersampling process, the pixel ratio N is defined as at which one pixel from every N pixels along the transverse directions in the fully sampled FMM image (which has the same sampling number as the wide-field image) was selected to form the undersampled image. Thus, the sampling number of FMM images is only $1/N^2$ as that of the wide-field images. If we mainly consider the influence of FMM imaging speed in the hybrid imaging system, we can speed up the image acquisition process by N^2 times through the undersampling approach.

To combine the low and high frequency components in 2D Fourier domain, we investigated two types of filters, the rectangular filter (R) and modified Gaussian filter (G), which are defined as

$$LP_R = \begin{cases} 1\,, & f_r \le f_{R,cut-off} \\ 0, & f_r > f_{R,cut-off} \end{cases}, \tag{5-9}$$

$$LP_G = \begin{cases} \exp\left[-\dfrac{\ln 2}{2}\dfrac{f_r^2}{f_{G,cut-off}^2}\right], & f_r \le f_{BW,FMM} \\ 0, & f_r > f_{BW,FMM} \end{cases}, \tag{5-10}$$

where $f_r = \sqrt{f_x^2 + f_y^2}$ is the frequency in transverse axis. Obviously the cut-off frequency, $f_{R,cut-off}$ and $f_{G,cut-off}$, should not larger than the bandwidth of the undersampled FMM image ($f_{BW,FMM}$). All the frequency components of undersampled FMM image will be used in reconstruction if we choose the cut-off frequency the same as the bandwidth of the undersampled FMM image. However, this may not be optimal due to frequency overlapping in the Fourier spectrum of the undersampled FMM image. Therefore, the cut-off ratio was introduced as

$$\tau = \frac{f_{cut-off}}{f_{BW,FMM}}. \tag{5-11}$$

The complementary high-pass filter is given by $HP = 1 - LP$. On the other hand, we select the weight factor η in Eq. (5-8) in a way that the FMM image and wide-field image have the same average spectral power at the cut-off frequency.

Since the image reconstruction is processed in 2D slice by slice, proper weight coefficients for combination of different slices must be selected. Here we apply the total intensity of the undersampled FMM image as the total intensity of the reconstructed image, because FMM image excludes the out-of-focus background. Therefore, the sampling rate of FMM image must exhibit a good estimation of the total intensity of the reconstructed image; otherwise the contrast between different slices may be inaccurate. Based on this principle, it is reasonable to expect a more accurate contrast for processing larger images, where the undersampled FMM images have more chance to reveal accurate intensity ratio for different slices. This can be considered as another advantage of our method since it often requires a huge image size in observing live biological processing.

To evaluate the reconstruction fidelity quantitatively, we calculate the MSE based on the fully sampled FMM image, i.e.

$$MSE = \frac{\sum \left| I_{reconstruct} - I_{full-FMM} \right|^2}{\sum \left| I_{full-FMM} \right|^2}. \tag{5-12}$$

Figure 5.8 shows the MSE of images reconstructed with Gaussian and rectangular filters using different pixel ratios and cut-off ratios. Given the same values of pixel ratio and cut-off ratio, the Gaussian filter outperforms rectangular filter in most cases, which can be contributed to the smoother transition from low frequency to high frequency in Gaussian filter. In general, the MSE increases as the pixel ratio increases, because higher pixel ratio (less sampling number of FMM image) gives less capability of background rejection and less accuracy of the low frequency components. As for the cut-off ratio, the minimal MSE appears at the range of $\tau = 0.4 \sim 0.8$, which can be considered as a good compromise between the effect of background rejection and the frequency overlapping of the undersampled FMM images.

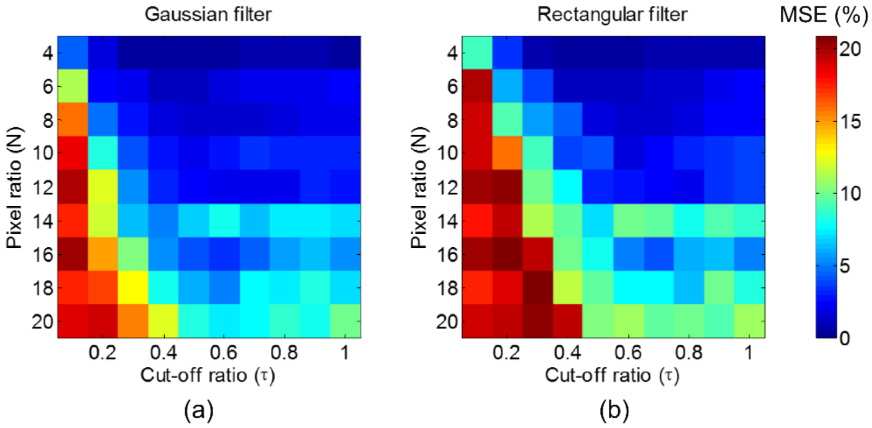

Figure 5.8 The MSE of images reconstructed with Gaussian (a) and rectangular (b) filters using different pixel ratios and cut-off ratios.

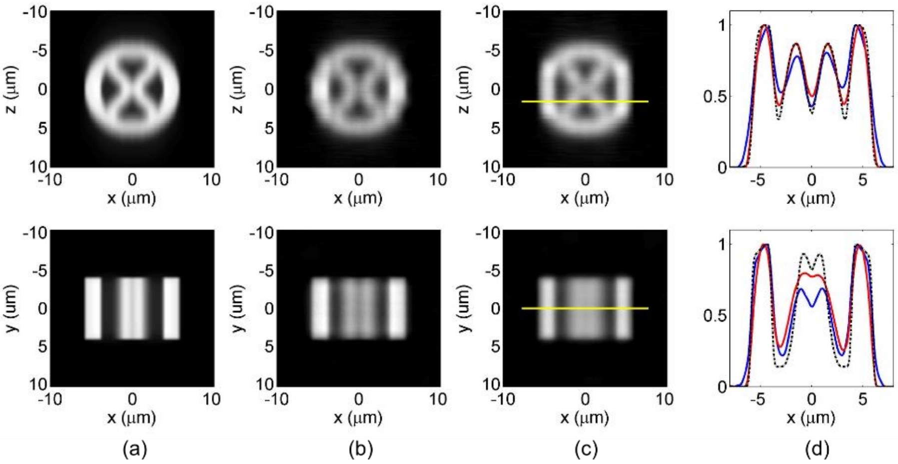

Figure 5.9 (a) The cross-section of original fully sampled FMM image in x-z and x-y plane. The reconstructed images with cut-off ratio τ=0.6 and pixel ratios (b) N=14 and (c) N=16. (d) Normalized intensity profiles of full sampled FMM (black dashed line) and the reconstructed images with the pixel ratios N=14 (blue line) and N=16 (red line) along the yellow lines in (c).

An interesting phenomenon is that the MSE at $N = 14$ is greater than that at $N = 16$

in both Gaussian and rectangular filters when the cut-off ratio is larger than 0.4. Anyway, both of the reconstructed images conserve the main features of the sample very well (Figure 5.9 (a ~ c)). The less MSE of the latter is attributed to better contrast conservation (Figure 5.9 (d)). It seems counterintuitive that the less sampling number conserves a better contrast. However, for a small image, such as the example here with the diameter 12 μm and feature size about 1.5 μm, a high pixel ratio ($N \geq 14$) may produce a grid pattern which does not reveal the low frequency as it could be. Although the MSE is greater at $N = 14$, comparison of the line profiles of the central hubs shows that it outperforms that $N = 16$ in recovering the fine structures (Figure 5.9 (d)). Nevertheless, the MSE of the reconstructed image with Gaussian filter is less than 10% when the pixel ratio is no more than 20 and the cut-off ratio is between 0.5 and 0.9.

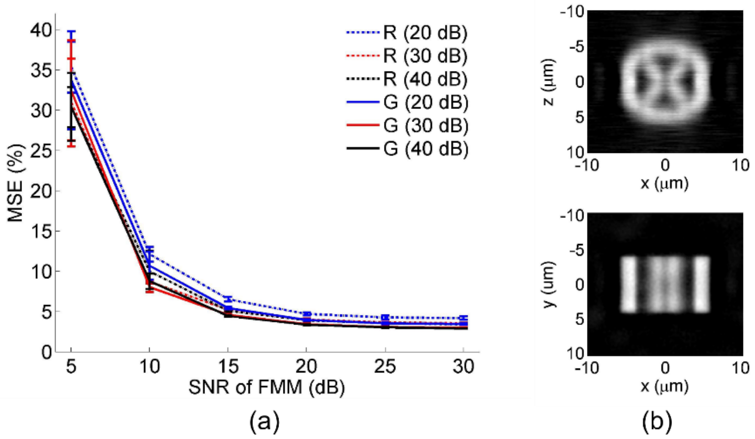

Figure 5.10 (a) The MSE of images reconstructed by rectangular (R) and Gaussian (G) filers with different SNRs, where the numbers in the legend indicate the SNR of wide-field images. (b) The image reconstructed by Gaussian filter with SNR=10dB for FMM image and SNR=20dB for wide-field image.

The influence of the noises in wide-field image and FMM image in reconstruction was investigated (Figure 5.10), where we chose the pixel ratio $N = 16$ and cut-off ratio $\tau = 0.6$. As expected, the MSE decreases as the SNRs of FMM and/or wide-field images increase for both the rectangular and Gaussian filters. The Gaussian filter performs much better than the rectangular filter when they are applied to the images with the same SNR of FMM image or wide-field image. Especially, the MSE is less than 12% when a Gaussian filter is applied to the image reconstruction with a FMM image with SNR no less than 10dB. The reconstructed image well rejects the out-of-focus background and maintain the features of the object (Figure 5.10 (b)), although the performance is not as good as that with high SNR. Thus, the noise level $SNR \geq 10dB$ for FMM images can be considered as a criterion for successful reconstruction, and Gaussian filter is preferred.

5.3.2 Reconstruction in 3D Fourier domain

The reconstruction process can be implemented via Eqs. (5-6) ~ (5-8) in 3D Fourier domain. The effects of pixel ratio and cut-off ratio were first investigated in transverse axes in Fourier domain, while the FMM image was fully sampled in axial axis.

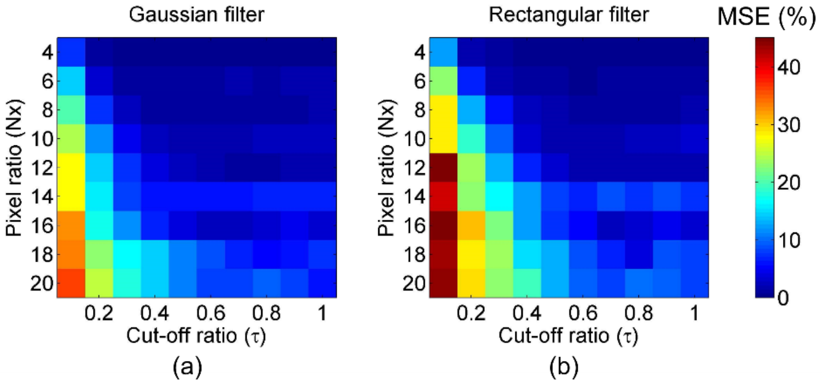

Figure 5.11 The MSE of images reconstructed with Gaussian (a) and rectangular (b) filters using different pixel ratios and cut-off ratios in transverse axes.

Figure 5.11 shows the MSE of images reconstructed with Gaussian and rectangular filters using different pixel ratios and cut-off ratios in transverse axes. Similar to the reconstruction in 2D Fourier domain, the Gaussian filter performs much better than the rectangular filter in most cases for given the same values of pixel ratio and cut-off ratio. The MSE generally increases as the pixel ratio increases. For the cut-off ratio, both filters give the minimal MSE at the range of $\tau = 0.6 \sim 0.8$. We chose $N = 16$ and $\tau = 0.7$ to explore the optimal values in axial axis in the following simulation. The corresponding MSE is 2.2% and 2.3% for Gaussian and rectangular filters, respectively.

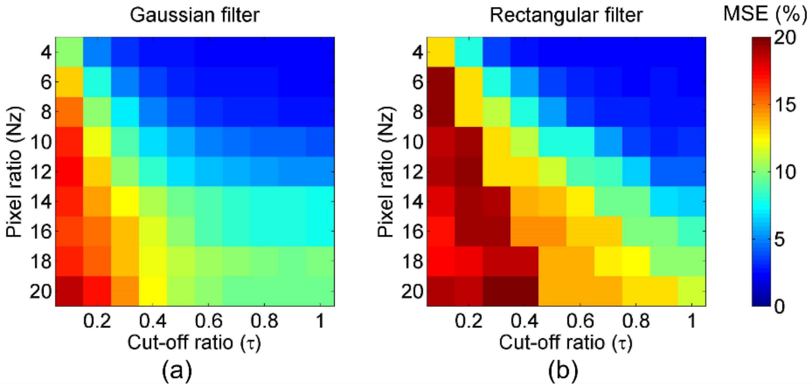

Figure 5.12 The MSE of images reconstructed with Gaussian (a) and rectangular (b) filters using different pixel ratios and cut-off ratios in axial axis.

Figure 5.12 shows the MSE of images reconstructed with Gaussian and rectangular filters using different pixel ratios and cut-off ratios in axial axis. In general, the Gaussian filter performs much better than the rectangular filter, which indicates the importance of smooth transition from low frequency to high frequency in axial axis in 3D reconstruction. For a given pixel ratio, the MSE decreases monotonically as the cut-off ratio in axial axis increases, which is different from that in transverse axes. This phenomenon can be attributed to that the frequency transition is not required in axial axis because there is no axial frequency in the 'missing cone' region in wide-field images. Thus, we can choose the axial cut-off ratio as unity, as long as the pixel ratio satisfies the reconstruction requirements.

Figure 5.13 shows the images reconstructed by Gaussian filter with different axial pixel ratios. The features of the object can be well recovered when the axial pixel ratio is small (Figure 5.13 (a)). The main features can still be distinguished as the axial pixel ratio increases to 12, but the out-of-focus background increases, which means the sectioning capability of FMM is weakened by undersampling at such a level. When the axial pixel ratio decreases further to 20, the top and bottom arcs of the spoke-wheel becomes hardly to see. Therefore, the axial pixel ratio $N_z = 12$ may be considered as a criterion of axial undersampling. The specific values could change in other situations, depending on the specific requirements of sectioning effect.

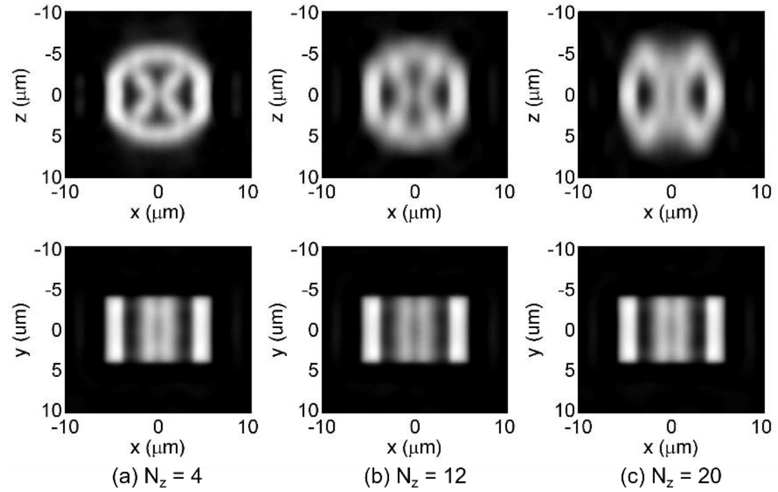

(a) $N_z = 4$ (b) $N_z = 12$ (c) $N_z = 20$

Figure 5.13 Images reconstructed using different axial pixel ratios, where the transverse pixel ratio is 16, the transverse and axial cut-off ratios are 0.7 and 1.0, respectively.

In addition, the reconstructed image at $N_z = 20$ looks similar to the HiLo image shown in Figure 4.2, but with a better background rejection. One reason is attributed to better sectioning capability of FMM. The other reason may be attributed to the difficulty in proper selection of weight factors for different slices in HiLo algorithm, while in our reconstruction method the intensity distribution in 3D space can be conveniently retrieved from FMM images.

5.3.3 Preliminary Experiment result

To test the proposed hybrid imaging in Fourier domain, we used a wide-field image and an undersampled image acquired by a confocal microscope (CM). As mentioned before, the principle of hybrid imaging in Fourier domain is applicable to any scanning microscopy as long as it has sectioning capability.

A silk sponge stained by fluorescent dye rhodamine 6G was imaged in the experiment. The peak emission wavelength is 559nm. The sample was imaged by a commercial microscope (Olympus IX81) with a wide-field mode and then a confocal mode, where they share the same objective lens with the NA of 0.25. The pixel size of the wide-field image is 0.32 μm, while it is 2.76 μm in the original CM image. Before reconstruction, the CM image was undersampled again by a factor of 2, so the effective pixel size of CM image is 5.52 μm. Here only one slice of wide-field image and one slice of CM image are used, so only reconstruction in 2D Fourier domain was tested.

Figure 5.14 compares the wide-field image, undersampled CM image and the reconstructed image. The undersampled CM image looks like mosaic pattern, so we rendered the image by zero-padding in Fourier domain. Although the contrast of rendered CM image looks good, no details of the sample can be observed because of highly undersampling rate. The fine features are revealed in the wide-field image, but the contrast is very low due to strong out-of-focus background. On the other hand, the reconstructed image conserves high contrast from CM image and high resolution from wide-field image (Figure 5.14 (d)).

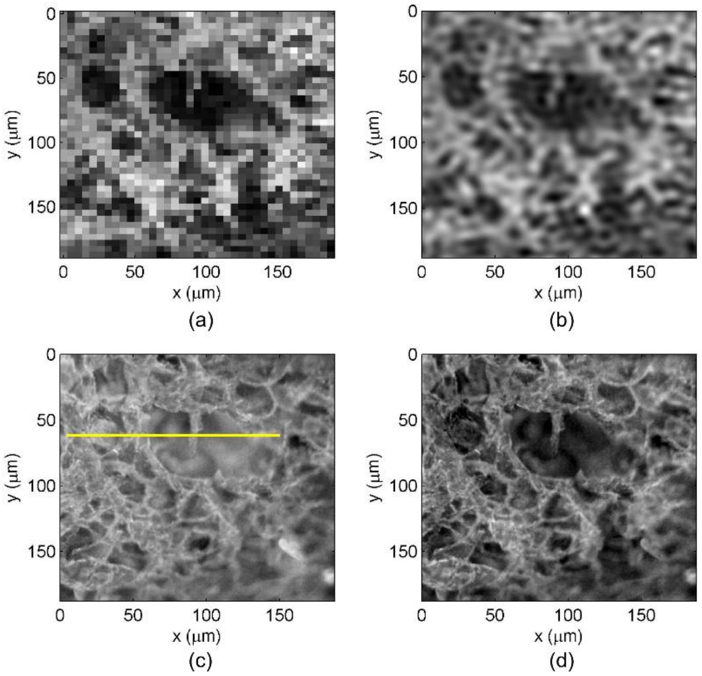

Figure 5.14 Raw data of (a) undersampled CM image and (c) wide-field image. (b) Rendered CM image by zero-padding in Fourier domain. (d) Image reconstructed by hybrid imaging in 2D Fourier domain.

Figure 5.15 shows the normalized line profiles of wide-field image, rendered CM image and image reconstructed by hybrid imaging along the yellow line in Figure 5.14 (c). It can be clearly observed that the hybrid imaging effectively reject the out-of-focus background and maintain the fine structural features which cannot be seen in the CM image.

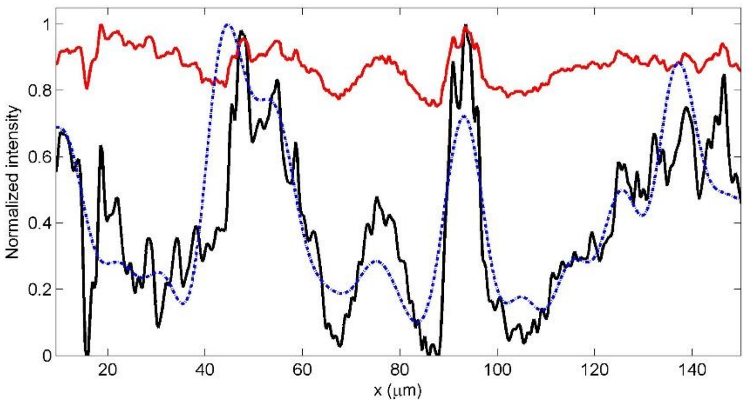

Figure 5.15 Normalized line profiles of wide-field image (red solid), rendered CM image (blue dashed) and image reconstructed by hybrid method (black solid) along the yellow line in Figure 5.14 (c).

5.4 Hybrid imaging in sequence

The quality of wide-field image can be improved by iterative reconstruction using the corresponding wide-field PSF, which has been shown in Figure 5.3 (c). Ideally, the PSF can be determined by parameters of the imaging system, e.g. illumination source, light path, objective, and so on. However, it depends on many factors that are difficult to be accurately obtained, for example, aberrations and optical properties of the samples. Small spherical beads, usually with diameter less 1 micron, are often introduced to mimic a point object for measurement of PSF, which is suitable for calibrating PSF of the imaging system but not applicable for the errors introduced by the sample itself. Here we proposed to use FMM to retrieve the wide-field PSF, and then reconstruct the image from wide-field raw data. Since the volume of PSF is usually much smaller than the sample, we can use a small volume of FMM images to retrieve PSF. Thus, the imaging time of FMM in this case is negligible compared to the time of scanning the whole sample by FMM. This hybrid imaging technique consists two sequent steps in reconstruction:

1) Retrieve PSF from FMM and wide-field raw images in a small volume;
2) Reconstruct images from the whole wide-field raw images using retrieved PSF.

In the following sub-sections, the PSF retrieval and image reconstruction using the retrieved PSF are studied. In the simulation, the wavelengths of the excitation and emission light are 488nm and 530nm, respectively. The transverse and axial pixel sizes are $\Delta x = \Delta y = 0.2\mu m$ and $\Delta z = 0.4\mu m$. Gaussian noise was added to the simulated raw images with $SNR = 20dB$ for both FMM and wide-field images, if not specified.

5.4.1 PSF retrieval

For wide-field microscopy, the image is the convolution of the object and the PSF, which can be written by recalling Eq. (4-1)

$$g(\mathbf{r}) = f(\mathbf{r}) \otimes h(\mathbf{r}), \tag{5-13}$$

where $g(\mathbf{r})$ is the recorded image, $f(\mathbf{r})$ denotes the object, and $h(\mathbf{r})$ is the PSF. Since FMM has sectioning capability and performs better resolution than wide-field microscopy, we can approximate FMM image as the object and retrieve the PSF with known FMM and wide-field images. In this way, the quality of the reconstructed image is expected close to the FMM image rather than the original object.

Due to inevitable noise in the raw images, the PSF cannot be retrieved by direct inversing Eq. (5-13) in Fourier domain. We adopted following steps to retrieve the PSF:

1) Calculate an initial PSF by a modified Wiener filter,

$$H = \frac{1}{F} \cdot \frac{|F|^2}{|F|^2 + \eta_1} \cdot \frac{|G|^2}{|G|^2 + \eta_2}, \tag{5-14}$$

where *G*, *F* and *H* are Fourier transform of $g(\mathbf{r})$, $f(\mathbf{r})$ and $h(\mathbf{r})$, respectively, *H* is also called optical transfer function (OTF), and η_1 and η_2 are parameters related to SNR of raw FMM and wide-field images.

2) Pass the amplitude and phase of *H* through a 3D median filter.

3) Adopt iterative constraints on PSF in spatial domain and Fourier domain.

The constraint in spatial domain is the effective volume of the intensity distribution of PSF, which is described as an hourglass with radius of Airy disk and radiation angle $\alpha = \text{asin}(NA)$ with respect to axial angle [139].

Rather than only bandwidth constraint used in Fourier domain [139], we derived a more specific boundary condition for OTF. The OTF is a convolution of 3D complex pupil function, which is nonzero only on a spherical cap related to the NA and wavelength [140]. Thus, the support region of OTF in Fourier domain was derived as

$$\begin{cases} k_r^2 - 2k_r k_0 \sin\alpha + k_z^2 + 2k_z k_0 \cos\alpha \le 0 \\ k_r^2 - 2k_r k_0 \sin\alpha + k_z^2 - 2k_z k_0 \cos\alpha \le 0 \end{cases}, \tag{5-15}$$

where k_r and k_z are spatial frequency in transverse and axial axes, k_0 is the wave number determined by the wavelength and $k_0^2 = k_r^2 + k_z^2$, α is the angular semi-aperture of the objective lens given by $\alpha = \operatorname{asin}(NA)$.

A spherical shell with inner radius 3 μm and outer radius 6 μm was simulated for PSF retrieval. Figure 5.16 (a) and (b) show the raw FMM and wide-field images, respectively, where the NA used is 0.5. As shown in Figure 5.16 (c) and (d), the retrieved PSF is very close to the theoretical one, while the error mainly comes from side-lobes due to noise effect. We tested for NA from 0.5 to 0.9 for PSF retrieval, and the results showed that the PSF with MSE ranging from 2% to 10% can be obtained with about 10 iterations of the constraints in spatial domain and Fourier domain.

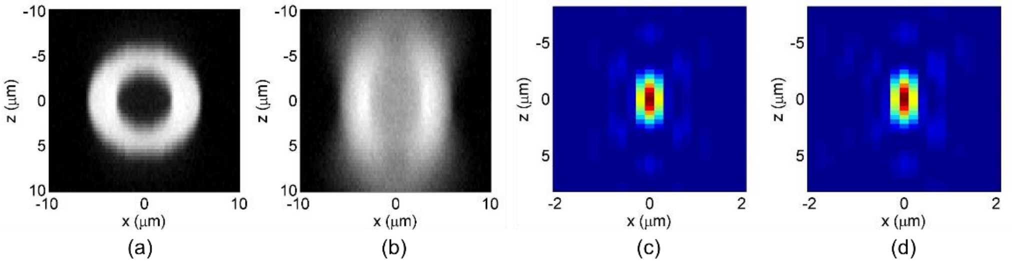

Figure 5.16 FMM (a) and wide-field (b) images used in PSF retrieval. The theoretical (c) and retrieved (d) PSF.

5.4.2 Image reconstruction

To avoid possible duality in reconstruction, we adopted the spoke-wheel as shown in Figure 5.1 for image reconstruction, but not the spherical shell used in PSF retrieval.

The MSE was used to quantitatively evaluate the performance of reconstruction by retrieved PSF. Normally the original object is used as the standard in MSE calculation. However, here it is more suitable to apply the FMM image as the standard, since the

FMM image is approximated as the object in PSF retrieval. As shown in Figure 5.17, the MSE based on the object is remarkably greater than that based on FMM images. In general, the MSE decreases as the NA increases because of resolution improvement. The TV regularization outperforms the Tikhonov regularization.

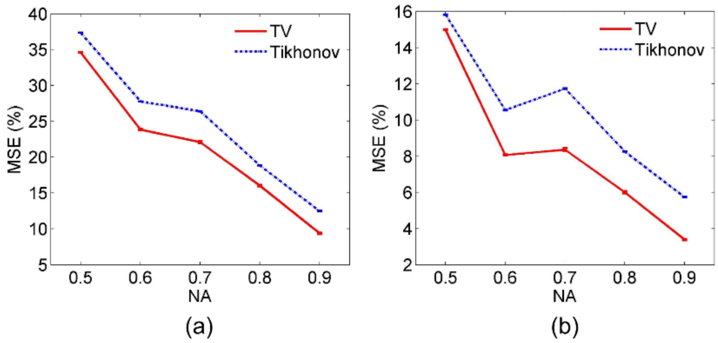

Figure 5.17 The MSE of reconstruction using raw wide-field data with different NA, where the object (a) and corresponding FMM images (b) are used as standards in MSE calculation.

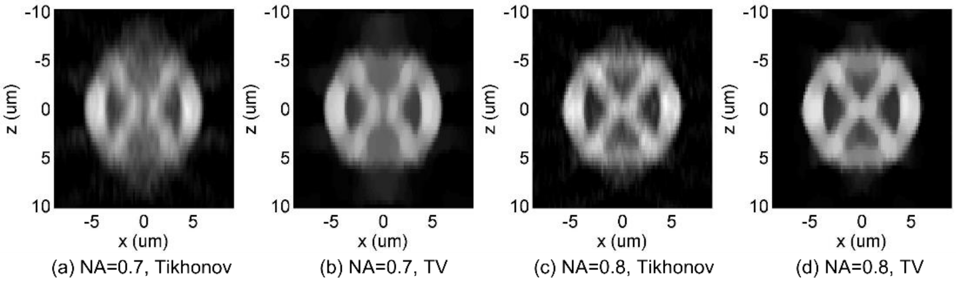

(a) NA=0.7, Tikhonov (b) NA=0.7, TV (c) NA=0.8, Tikhonov (d) NA=0.8, TV

Figure 5.18 Images reconstructed from raw wide-field images using Tikhonov (a, c) and TV (b, d) regularizations with NA=0.7 (a, b) and NA=0.8 (c, d).

To visually compare the performance using different NA, Figure 5.18 shows the images reconstructed by $NA = 0.7$ and $NA = 0.8$ with Tikhonov regularization and TV regularization. The top and bottom arcs are suppressed by background in both Tikhonov and TV reconstruction for $NA = 0.7$, due to lack of enough resolution. On the other hand, the main features are recovered for $NA = 0.8$, although there is residual background in the gap regions between the spokes. Thus, the $NA = 0.8$ may be considered as a criterion in reconstruction of images with feature size similar to that in our simulation. In addition, the TV regularization can suppress noise and smooth the reconstructed images, the same as previous results.

Comparing the MSE in Figure 5.17 to that of reconstruction by theoretical PSF

(Figure 5.3 (a) and Figure 5.5 (a)), the MSE of reconstruction by retrieved PSF is greater, as expected. However, the reconstruction by theoretical PSF also fails to reveal some features when the NA is small, as shown in Figure 5.2 (a). So, the error in reconstruction with retrieved PSF is partially from the error in PSF retrieval, and partially due to the resolution limitation of the imaging system. The criterion of the NA could vary for samples with different feature sizes.

5.5 Discussion and conclusion

In this chapter, we proposed hybrid imaging modalities in spatial domain, in Fourier domain and in sequence, for different scenarios. If we compare the performance of these approaches, e.g. by MSE, we will find the diverse imaging (in spatial domain) outperforms the other two, and the sequential hybrid imaging performs the worst. However, accurate PSFs of FMM and wide-field microscopy are required in diverse imaging, while the other two do not need PSF. As for the image acquisition process, a very small scanning volume for PSF retrieval in sequential hybrid imaging usually contains smaller sampling number than undersampling the whole volume in the Fourier hybrid imaging. If the PSF is mainly affected by the imaging system itself rather than samples, the sampling number in sequential hybrid imaging can be highly reduced since only one scanning image is enough. Thus, the reconstruction technique with higher performance requires more information of the imaging system and/or more measurements, which often introduces more cost of setup and challenges in implementation. A proper choice of hybrid imaging techniques depends on the practical requirements and feasibility.

In conclusion, hybrid imaging methods in spatial domain, in Fourier domain and in sequence are proposed and evaluated in this chapter. The diverse imaging (in spatial) performs the best reconstruction by using accurate PSFs of the imaging systems. Rather than iterative reconstruction, the Fourier hybrid imaging can be implemented directly in Fourier domain. Although the sequential hybrid imaging does not reconstruct images as good as the other two, the resulted images have better quality than wide-field images, and this technique requires the least information of the imaging system and the least measurements.

Chapter 6

Classical imaging theory of a micro-lens

6.1 Introduction

A long-standing issue of traditional microscopy is that its resolution is limited to about half of the illumination wavelength as a result of the loss of evanescent waves during wave propagation. To break this resolution limit and achieve super-resolution, researchers have developed various approaches. One approach is to recover the evanescent waves in far-field by using negative refractive index metamaterials, which could achieve unlimited resolution in theory [141]. However, because of practical difficulties such as loss, this approach has not been practically used. Another approach is to deliberately create a specific situation where only a single light emitting spot (or sparsely distributed spots) will locate in the field of view, such that the overlapping of Point Spread Function (PSF) will not occur in principle. Typical examples include Stimulated Emission Depletion (STED) microscopy, Stochastic Optical Reconstruction Microscopy (STORM) [12] and photo activated localization microscopy (PALM) [14]. Although being very successful in practice, these microscopy technologies share an inherent drawback: they generally require temporal and spatial scanning which will take a long time, and thus are not very suitable for dynamic real-time imaging.

Achieving super-resolution without utilizing either evanescent waves or scanning is obviously in great demand. Recently, the phenomenon of photonic nano-jet with a subwavelength focus formed by a transparent micro-lens has been considered as a potential approach to beat the diffraction limit [142-144]. A remarkable record of 50nm lateral resolution has been reported for real-time imaging through a dielectric micro-lens with white light illumination [145]. This significant progress undoubtedly will bring out a profound impact on related disciplines in biology, chemistry, medicine, and semiconductor industry. However, the previous attribution of this high resolution [145] to the photonic nano-jet focusing phenomenon [142-144] remains elusive in the sense that imaging and focusing are two distinctive physical phenomena that do not always have necessary connection in resolution. While most previous literatures adopted focusing analysis [145], a direct imaging calculation through a micro-lens with vectorial electromagnetic analysis can provide more physical insights. Here we apply the classical Mie scattering theory to simulate the real imaging process by placing light emitters behind the micro-lens and observing them in the far field.

6.2 Model of wide-field micro-lens imaging

As shown in Figure 6.1, two incoherent dipoles pointing in the *z* direction are placed on the object plane just beside the micro-lens (diameter D = 4.74 μm, refractive index n = 1.46), similar to the experimental setup of the micro-lens imaging system [145]. The waves radiated from the dipoles propagate through the micro-lens and are collected on the collecting plane in the far-field. The interaction between the dipole radiation and the micro-lens is calculated by multipole expansion based on spherical harmonics and Mie scattering theory. The Numerical Aperture (NA) with respect to the origin of the object plane is 0.9, the same as in [145]. According to angular spectrum representation, the collected waves are decomposed into plane waves, which will then numerically propagate backward in the negative *x* direction to form a virtual image on the image plane.

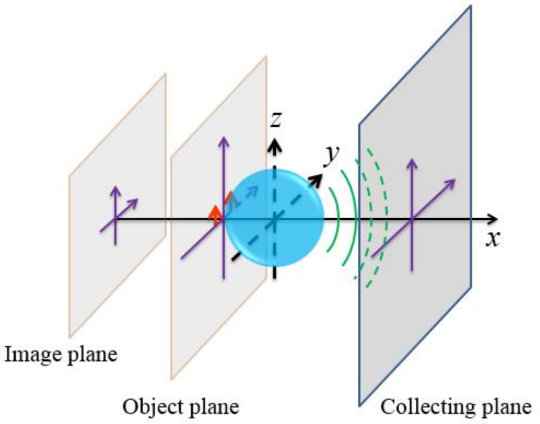

Figure 6.1 Configuration of image reconstruction of two incoherent dipoles. The origin of the coordinates (x,y,z) coincides with the center of the micro-lens.

6.3 Multipole and plane wave expansions for micro-lens scattering

To calculate the field distribution in the whole space, the electric field ($\bar{E}$) and magnetic field ($\bar{H}$) is decomposed into TE and TM modes (with respect to the direction of $\hat{r}$) in free space by introducing the scalar potentials ψ_{TM} and ψ_{TE} , respectively [146],

$$\begin{aligned}
\bar{H}_{TM} &= \frac{1}{\mu}\nabla\times\left(\hat{r}\psi_{TM}\right), \\
\bar{E}_{TM} &= -\frac{1}{i\omega\varepsilon}\left[\nabla\times\left(\frac{1}{\mu}\nabla\times\left(\hat{r}\psi_{TM}\right)\right)\right], \\
\bar{H}_{TE} &= -\frac{1}{i\omega\mu}\left[\nabla\times\left(\frac{1}{\varepsilon}\nabla\times\left(\hat{r}\psi_{TE}\right)\right)\right], \\
\bar{E}_{TE} &= -\frac{1}{\varepsilon}\nabla\times\left(\hat{r}\psi_{TE}\right),
\end{aligned} \tag{6-1}$$

where ε and μ are the permittivity and the permeability, respectively, and ω is the temporal frequency of the field.

By substituting Eq. (6-1) into Green's function in the spherical coordinates $\left(r,\theta,\varphi\right)$ and using the method of separation of variables, we can obtain the expressions of the two scalar potentials for the dipole located at $\bar{r}_p$ as

$$\begin{aligned}\psi_{TM} &= \sum_{n=1}^{\infty}\sum_{m=-n}^{n} C_{nm}^{TM}\hat{\zeta}_n(kr)P_n^{|m|}(\cos\theta)e^{im\varphi},\\ \psi_{TE} &= \sum_{n=1}^{\infty}\sum_{m=-n}^{n} C_{nm}^{TE}\hat{\zeta}_n(kr)P_n^{|m|}(\cos\theta)e^{im\varphi},\end{aligned} \tag{6-2}$$

where C_{nm}^{TM} and C_{nm}^{TE} are constant coefficients which are determined by the function of the specific dipole used in study, $\hat{\zeta}_n(kr)$ denotes the spherical Bessel function of first kind ($\hat{J}_n(kr)$) for $r < r_p$ or the spherical Hankel function of first kind ($\hat{H}_n(kr)$) for $r > r_p$, $P_n^{|m|}$ denotes associated Legendre polynomials, and k is the wave number in free space.

Similarly, the potentials of internal fields inside the micro-lens (ψ_{TM}^{int} and ψ_{TE}^{int}) and the potentials of scattering fields (ψ_{TM}^{S} and ψ_{TE}^{S}) can be expressed as

$$\begin{aligned}\psi_{TM}^{\text{int}} &= \frac{1}{\eta_0\omega}\sum_{n=1}^{\infty}\sum_{m=-n}^{n} a_{nm}^{TM}\hat{J}_n(k_{\text{int}}r)P_n^{|m|}(\cos\theta)e^{im\varphi},\\ \psi_{TE}^{\text{int}} &= \frac{1}{\eta_0\omega}\sum_{n=1}^{\infty}\sum_{m=-n}^{n} a_{nm}^{TE}\hat{J}_n(k_{\text{int}}r)P_n^{|m|}(\cos\theta)e^{im\varphi},\\ \psi_{TM}^{S} &= \frac{1}{\eta_0\omega}\sum_{n=1}^{\infty}\sum_{m=-n}^{n} b_{nm}^{TM}\hat{H}_n(kr)P_n^{|m|}(\cos\theta)e^{im\varphi},\\ \psi_{TE}^{S} &= \frac{1}{\eta_0\omega}\sum_{n=1}^{\infty}\sum_{m=-n}^{n} b_{nm}^{TE}\hat{H}_n(kr)P_n^{|m|}(\cos\theta)e^{im\varphi}.\end{aligned} \tag{6-3}$$

where k_{int} represents the wave number inside the micro-lens.

Now, all the electromagnetic fields can be expanded in terms of the corresponding scalar potentials by Eq. (6-1). Given that the multipole functions form an orthogonal basis, we can obtain all the coefficients in Eq. (6-3) by applying the boundary conditions at the surface of the micro-lens. The coefficients are given by

$$
\begin{aligned}
a_{nm}^{TM} &= \frac{-i}{\sqrt{\frac{\mu_0 \epsilon_0}{\mu_{int}\epsilon_{int}}}\hat{J}_n^{'}\left(k_{int}R\right)\hat{H}_n\left(kR\right)-\frac{\mu_0}{\mu_{int}}\hat{J}_n\left(k_{int}R\right)\hat{H}_n^{'}\left(kR\right)} C_{nm}^{TM}, \\
a_{nm}^{TE} &= \frac{-i}{\frac{\epsilon_0}{\epsilon_{int}}\hat{H}_n^{'}\left(kR\right)\hat{J}_n\left(k_{int}R\right)-\sqrt{\frac{\mu_0 \epsilon_0}{\mu_{int}\epsilon_{int}}}\hat{H}_n\left(kR\right)\hat{J}_n^{'}\left(k_{int}R\right)} C_{nm}^{TE}, \\
b_{nm}^{TM} &= \frac{\sqrt{\frac{\mu_0 \epsilon_{int}}{\mu_{int}\epsilon_0}}\hat{J}_n^{'}\left(kR\right)\hat{J}_n\left(k_{int}R\right)-\hat{J}_n^{'}\left(k_{int}R\right)\hat{J}_n\left(kR\right)}{\sqrt{\frac{\mu_0 \epsilon_{int}}{\mu_{int}\epsilon_0}}\hat{H}_n^{'}\left(kR\right)\hat{J}_n\left(k_{int}R\right)-\hat{J}_n^{'}\left(k_{int}R\right)\hat{H}_n\left(kR\right)} C_{nm}^{TM}, \qquad (6\text{-}4) \\
b_{nm}^{TE} &= \frac{\sqrt{\frac{\mu_0 \epsilon_{int}}{\mu_{int}\epsilon_0}}\hat{J}_n^{'}\left(k_{int}R\right)\hat{J}_n\left(kR\right)-\hat{J}_n^{'}\left(kR\right)\hat{J}_n\left(k_{int}R\right)}{\sqrt{\frac{\mu_0 \epsilon_{int}}{\mu_{int}\epsilon_0}}\hat{H}_n\left(kR\right)\hat{J}_n^{'}\left(k_{int}R\right)-\hat{H}_n^{'}\left(kR\right)\hat{J}_n\left(k_{int}R\right)} C_{nm}^{TE},
\end{aligned}
$$

where the subscript *int* (internal) denotes the corresponding variables inside the micro-lens. With these coefficients, the scattering field can be obtained by Eq. (6-1).

According to angular spectrum representation, the collected field in the far-field can be decomposed into plane waves as

$$\mathbf{E}\left(k_y, k_z; x_c\right) = \frac{1}{2\pi}\iint_{NA} \bar{\mathbf{E}}\left(y, z; x_c\right)\exp\left[-i\left(k_y y + k_z z\right)\right]dydz, \qquad (6\text{-}5)$$

where $\mathbf{E}\left(k_y, k_z; x_c\right)$ is the Fourier transform of the field $\bar{\mathbf{E}}\left(y, z; x_c\right)$ at the position x_c, and *NA* represents the numerical aperture of the collecting plane which restricts the domain of integration in space. Here the axial axis is *x*-axis (Figure 6.1), which is different from that in optics where the *z*-axis is often defined as the axial axis. However, this representation is often used in representation of dipole radiation in electromagnetics.

Then the collected field can numerically propagate in space, which, according to angular spectrum representation, is given by

$$\bar{\mathbf{E}}\left(y, z, x\right) = \frac{1}{2\pi}\iint_{NA} \mathbf{E}\left(k_y, k_z; x_c\right)\exp\left[i\left(k_y y + k_z z + k_x x\right)\right]dk_y dk_z. \qquad (6\text{-}6)$$

The *E* field on the left-hand side of Eq. (6-6) represents the field polarized in either direction (*x*-, *y*-, or *z*-), which depends on the corresponding polarization of the field in the integrand. The reconstructed images are obtained by adding the intensities of all the corresponding fields together, i.e.,

$$I = |E_x|^2 + |E_y|^2 + |E_z|^2 , \tag{6-7}$$

which represents the virtual image produced by the micro-lens.

6.4 Whispering gallery mode in micro-lens

Whispering gallery mode (WGM) excited in a spherical micro-lens has been reported to enhance the resolution [147] since WGM enhances coupling evanescent waves into the micro-lens and converting to propagating waves [148]. To investigate the WGM of the micro-lens in the visible spectrum, we first numerically scan the backscattering cross section [147] of the micro-lens from wavelength 400nm to 700nm (Figure 6.2). The first WGM appears at the wavelength 401.64nm. Another wavelength 403.07nm without WGM is chosen for comparison.

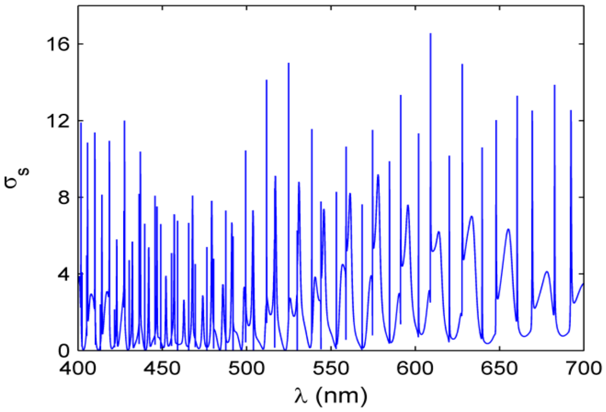

Figure 6.2 Backscattering cross-section in visible spectrum.

By placing a single dipole just beside the micro-lens (Figure 6.3), we find that the fields at wavelength 401.64nm with WGM (Figure 6.3 (a)) are enhanced significantly compared to that at wavelength 403.07nm without WGM (Figure 6.3 (b)). The strong surface wave in the case of WGM improves the wave coupling and conversion (Figure 6.3 (c)). On the other hand, the wave conversion by only refraction is very weak when there is no WGM (Figure 6.3 (d)).

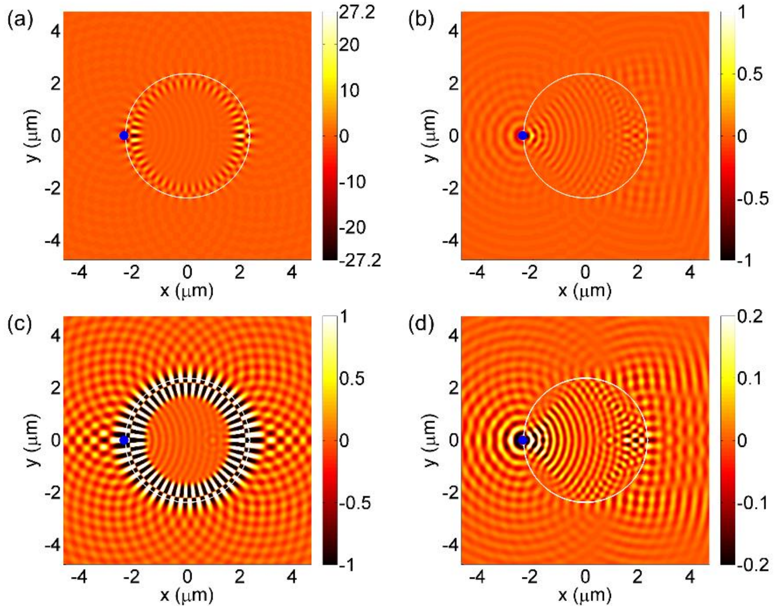

Figure 6.3 Snapshots of wave propagation in x-y *plane for* $\lambda = 401.64\text{nm}$ *(a, c) and* $\lambda = 403.07\text{nm}$ *(b, d). The color maps in (c) and (d) are truncated to reveal the pattern of weak fields. The white circle denotes the contour of the micro-lens. The small blue dot denotes the position of the dipole.*

6.5 Resolution of monochromatic light

To determine the position of the image plane, we examine the reconstructed intensity distribution in the *x*-*y* plane, as shown in Figure 6.4 (a) and (c) for wavelengths 401.64nm and 403.07nm, respectively, with the single dipole behind the micro-lens. From the view of geometrical optics, the focus of a micro-lens is at $R \times n/(n-2)$ (*R* is the radius of the micro-lens and *n* is its refractive index), i.e. at $x = -6.41\mu\text{m}$. This estimation may be applicable to the wavelength 403.07nm without WGM (Figure 6.4 (c)), but not appropriate for the wavelength 401.64nm with WGM (Figure 6.4 (a)). Alternatively, the maximum intensity position in the *x*-axis ($x = -4.40\mu\text{m}$ for wavelength 401.64nm and $x = -6.84\mu\text{m}$ for wavelength 403.07nm) can be considered as the focus, since the dipole is known to be on the *x*-axis. However, at $x = -4.40\mu\text{m}$ for the wavelength 401.64nm, the maximum side-lobes are 40% of the main-lobe

(Figure 6.4 (b)), which will cause distortion and poor contrast in wide-field imaging [149]. To reduce side-lobes, the focus $x = -4.87\mu\mathrm{m}$ adopted from [145] is also considered, where the maximal side-lobes decrease to about 22% of the main-lobe. Note that at the position $x = -3.94\mu\mathrm{m}$, the side-lobes are even higher than the main-lobe, which may introduce artifacts in practice.

The Full Width at Half Maximum (FWHM) is a widely used evaluation of resolution. To compare FWHM at different image planes, the magnification of the micro-lens must be considered, although the resolution is not necessarily related to magnification but rather wave coupling and conversion. The magnification can be estimated by shifting the dipole 50nm away from its original position along the *y*-axis and observing the corresponding shift of the virtual image. After being normalized by the magnification (1.82 for 401.64nm at $x = -4.40\mu\mathrm{m}$ and 2.84 for 403.07nm at $x = -6.84\mu\mathrm{m}$), the corresponding effective FWHMs are 107nm (with 40% side-lobes) for wavelength 401.64nm and 214nm for wavelength 403.07nm. The effective FWHM without WGM is close to the diffraction limit in air, while the one with WGM is much narrower, similar to the conclusion in [147]. Note that the effective FWHM with WGM is much smaller than 157nm, the FWHM achievable with an oil immersion lens of the same refractive index 1.46 and angular aperture ($\sin\alpha = 0.9$), which is mainly attributed to apodization. However, significant side-lobes may lead to large distortion and poor contrast in wide-field imaging. The side-lobes caused by apodization may be suppressed in confocal microscopy, where the resolution of a micro-lens can be enhanced by WGM to beat the diffraction limit. In the following text for monochromatic light, only waves with WGM will be considered to explore the possibly highest resolution.

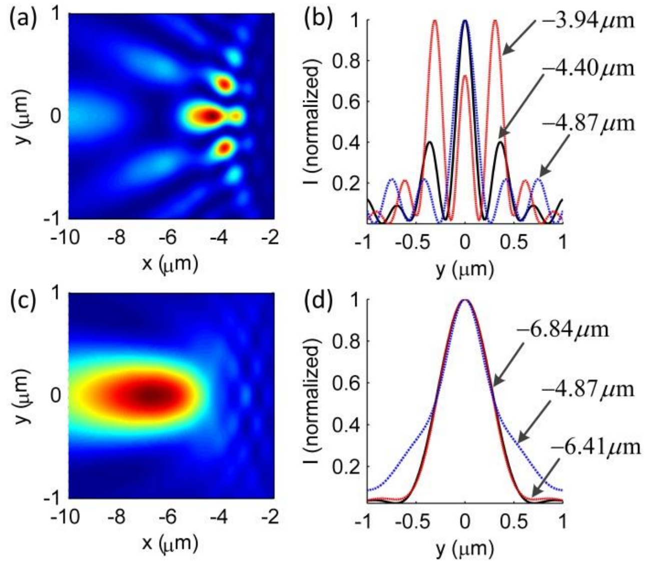

Figure 6.4 Reconstructed intensity distribution in x-y plane for (a) $\lambda = 401.64\text{nm}$ *and (c)* $\lambda = 403.07\text{nm}$. *Normalized intensity profile of (b)* $\lambda = 401.64\text{nm}$ *focused at* $x = -4.87\mu\text{m}$ *(blue dash-dot line),* $x = -4.40\mu\text{m}$ *(black solid line) and* $x = -3.94\mu\text{m}$ *(red dashed line), and (d)* $\lambda = 403.07\text{nm}$ *focused at* $x = -6.84\mu\text{m}$ *(black solid line),* $x = -6.41\mu\text{m}$ *(red dashed line) and* $x = -4.87\mu\text{m}$ *(blue dash-dot line).*

Another notable phenomenon is that different modes of WGM have different resolution enhancement. Here we compare the first TE mode and the first TM mode appearing at the wavelengths 401.64nm and 405.55nm, respectively. The analysis in Figure 6.5 demonstrates that the effective FWHM, after normalized by magnification, of wavelength 405.55nm is 186nm focused at $-8.17\mu\text{m}$ (maximum intensity position), 271nm focused at $-4.25\mu\text{m}$ (the other peak intensity position), 195nm focused at $-6.41\mu\text{m}$ (geometrical focus) and 413nm focused at $-4.87\mu\text{m}$ (position adopted from [145]). Compared with the TE mode, the TM mode has a much larger FWHM for the given radius and refractive index in our model. We tested other larger wavelengths with TE and TM modes and found that the narrowest effective FWHM is achieved by the shortest wavelength with TE mode of WGM, which is 401.636 nm.

To better evaluate resolution with the golden criterion of two-point resolution, we put two emitters behind the micro-lens with illumination wavelength 401.64 nm. Figure

6.6 (a) and (c) show the intensity distribution in *x*-*y* plane formed by two incoherent dipoles separated by distances of 150nm and 100nm, respectively. The dipoles separated by 150nm are clearly resolved (Figure 6.6 (a) and (b)). However, the dipoles separated by 100nm are hardly resolved (Figure 6.6 (c) and (d)). One may argue that two peaks can be resolved at the position $x = -3.94\mu\text{m}$ in the case of 100nm separation. However, the position $x = -3.94\mu\text{m}$ is not the true focus ($x = -4.40\mu\text{m}$), and the peaks are because of side-lobes, as illustrated in Figure 6.4 (a).

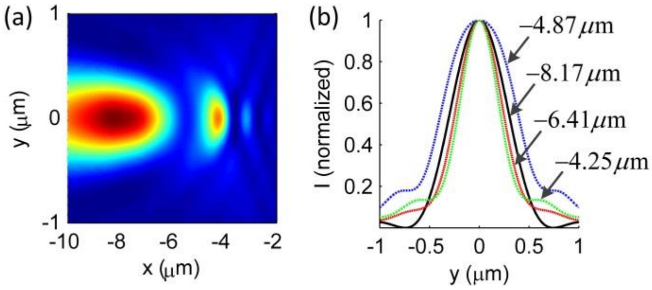

Figure 6.5 (a) Reconstructed intensity distribution in x-y plane for $\lambda = 405.55\text{nm}$ *. (b) Normalized intensity profile focused at* $x = -8.17\mu\text{m}$ *(black solid line),* $x = -6.41\mu\text{m}$ *(red dashed line),* $x = -4.87\mu\text{m}$ *(blue dash-dot line) and* $x = -4.25\mu\text{m}$ *(green dashed line).*

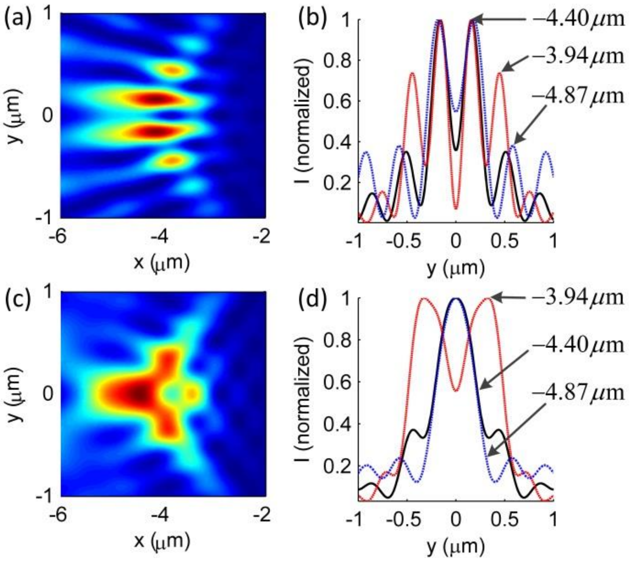

Figure 6.6 Reconstructed intensity distribution in x-y plane for two incoherent dipoles separated by (a) 150nm and (c) 100nm. Normalized intensity profile for two incoherent dipoles separated by (b) 150nm and (d) 100nm at the focus of $x = -4.87\mu\text{m}$ *(blue dash-dot line),* $x = -4.40\mu\text{m}$ *(black solid line) and* $x = -3.94\mu\text{m}$ *(red dashed line).*

6.6 Resolution of white light

To further explore the resolution of white light illumination, we chose 110 wavelengths including all WGMs in the spectrum 400nm~700nm to mimic white light. With such white light illumination, the micro-lens can resolve two dipoles separated 150nm apart (Figure 6.7 (a)), but cannot for those separated 100nm apart (Figure 6.7 (b)). Moreover, we have further tested images formed in various focuses, and got almost the same result. Actually, the effective FWHM of the combined white light cannot be smaller than the narrowest effective FWHM of monochromatic light, which is 107nm (with 40% side-lobes) at the wavelength 401.64nm. Thus, the resolution of a spherical micro-lens with white light illumination cannot reach sub-100nm.

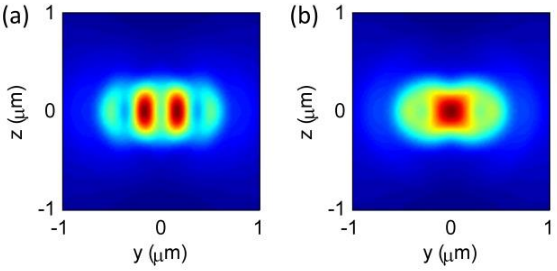

Figure 6.7 Images formed by two dipoles separated by (a) 150nm and (b) 100nm. The focus is chosen at $x = -4.40\mu\mathrm{m}$*, where the intensity of the white light is maximal.*

6.7 Discussion and conclusions

If the effective FWHM is adopted as the evaluation of resolution, the highest resolution of the micro-lens studied here is 107nm at the wavelength 401.64nm, which is $\lambda/3.75$ with λ the wavelength in free space. Compared to the FWHM (157nm) achieved with an oil immersion lens of the same refractive index 1.46 and angular aperture, it is narrowed by 32%, which is comparable to the improvement by apodization in pupil engineering. The micro-lens can be considered as a special case of pupil engineering: it is put on top of the sample to modify the amplitude and phase of the light, while in normal pupil engineering an amplitude and/or phase mask is put on the pupil plane.

However, the effective FWHM cannot be claimed as the same as resolution of micro-lens in wide-field imaging, because significant side-lobes (40% of the main-lobe) may result in remarkable distortion and even artifacts. Given non-negligible side-lobes in a point spread function (PSF), the FWHM may be claimed as resolution by specifying a limited field-of-view where the superposition of side-lobes is not greater than the main-lobe, which is beyond the scope of this chapter. On the other hand, the side-lobes may be suppressed in confocal microscopy, where the resolution of a micro-lens can be further improved by the selectivity of pinhole.

It should be emphasized that in our calculation some realistic factors that have been ignored may offer real reasons for the experimentally observed high resolution in the record. For example, our model only considers perfect spherical shape, while in reality surface roughness may play an important role in near-field imaging. Moreover, the gold-coated fishnet anodic aluminum oxide (AAO) sample was used in experiment [145], but the possible surface plasmon resonance and quantum or nonlocal effects induced by the periodic metallic sample are completely ignored in our calculation.

In conclusion, the direct imaging process through a micro-lens is calculated with Mie scattering theory. A micro-lens can achieve resolution beyond diffraction limit, but significant side-lobes may cause distortions, poor contrast and even artifacts in wide-field imaging. The resolution of a spherical micro-lens with visible light illumination is between 100nm and 150nm measured with two-point resolution criterion, or around 107nm evaluated by FWHM for the shortest wavelength with WGM. Therefore, some important physical mechanisms that have not been revealed (probably surface roughness enhanced surface plasmon resonance, nonlocal effects, or quantum effects) are expected to be involved in the previous successful experiments of ultra-high resolution.

Chapter 7

Conclusions and future work

7.1 Conclusions

This work is dedicated to imaging techniques with capabilities of optical sectioning, scattering rejection and noise suppression for 3D imaging in thick samples with high resolution in real-time. Optical modalities, including focal modulation, structured illumination, wide-field imaging and micro-lens, are investigated. Computational image reconstruction with sparsity priors is explored to improve the performance of such optical modalities or their combinations.

First, new approaches of aperture optimization for FMM were introduced and extended to cylindrically polarized illumination. The requirement of destructive interference occurring at the focus for anti-phase PSF motivated the methods of equal-ZPM and zero-sum ZPM based on the concept of pupil moment. The zero-sum ZPM provides the optimal aperture design for given conditions, but it requires optimization algorithms which are usually complicated and time consuming. With the help of series expansion by pupil moment, the method MFC introduces a simple analytic approach to optimize annular phase apertures. The modulation depth from MFC is very close to the optimal value, with a small difference less than 3%. MFC is also applicable to illuminations of circular and radial polarizations and AziSpi used in FMM, among which the circular polarization results in the largest modulation depth. AziSpi gives the best resolution for any given NA; whereas the radial polarization provides better resolution than linear and circular polarizations only in high NA cases. The inner-blocked apodization was found to simultaneously improve the modulation depth and resolution for radial polarization and AziSpi, but light efficiency is sacrificed. In a high NA system with considerable apodization, radial polarization is superior to AziSpi in maintaining Strehl ratio and light efficiency. However, the modulation depth and resolution of AziSpi are little affected by NA, which makes it robust in practical implementation. In addition, the apertures with more sub-apertures are more resistant to wavefront aberrations, although aberrations degrade modulation depth in general.

Second, diverse imaging with sparsity priors was investigated in the reconstruction of HiLo and SIM images. By rearranging the photons to their emission origins, diverse imaging outperforms conventional HiLo method in rejecting out-of-focus background. The image fidelity of diverse imaging is much better than the reconstruction from only uniform illumination data, as the missed frequency components in ‘missing cone’ are compensated by structured illumination. TV regularization was used to improve the reconstruction fidelity. The image quality degrades if the contrast of the structured illumination pattern decreases, which often happens in imaging deep inside highly scattering samples. This is attributed to relative weak compensation of high frequency components introduced by low contrast structured illumination. The image quality is improved as the spatial frequency of structured illumination pattern increases, because more compensation of high frequency components are shifted by structured illumination and then captured by detection OTF. The resolution in the direction perpendicular to the structured illumination fringes can be improved by diverse imaging, which is not reachable in HiLo method. However, the resolution in the other transverse direction is little improved, because the corresponding bandwidth cannot be extended by only one structured illumination image. Anyway, the transverse resolution can be improved by two structured illuminations via diverse imaging.

Third, to obtain high-speed image acquisition with sectioning capability, hybrid imaging modalities combining FMM and wide-field microscopy are introduced to implement in spatial domain, in Fourier domain and in sequence for different scenarios.

The diverse imaging approach was borrowed to hybrid image reconstruction in spatial domain, in which fast-scanning FMM images provide sectioning information and wide-field images offer high SNR. TV regularization remarkably improves reconstruction fidelity by reducing the MSE to about one-half of the Tikhonov regularization. Rather than iterative reconstruction, the Fourier hybrid modality directly recovers the image by combining Fourier components of undersampled FMM images with sectioning and wide-field images with high resolution (compared to undersampled images). This approach is efficient and robust, but the possibly best reconstruction result is just close to fully sampled FMM images. Nevertheless, the optical sectioning is obtained and it successfully rejects the out-of-focus background in wide-field images. The sequential hybrid scheme first explores the PSF from FMM and wide-field images in a small volume, and then reconstruct the whole volume of interest from wide-field images. The volume of scanning images is highly reduced, and the reconstruction process rearranges the out-of-focus background photons back to their emission origins. However, optical sectioning cannot be fully recovered due to lack of high frequency components in the 'missing cone'. From the point view of reconstruction fidelity, the diverse imaging performs superior to the other two, but it requires accurate PSFs of both FMM and wide-field imaging systems.

In addition, a theoretical model of direct imaging process through a micro-lens is established with vectorial electromagnetic analysis. The simulation results show that a micro-lens can achieve resolution beyond diffraction limit, but significant side-lobes may cause distortions, poor contrast and even artifacts in wide-field imaging mode. The resolution of a spherical micro-lens with visible light illumination is between 100nm and 150nm measured with two-point resolution criterion, or around 107nm evaluated by FWHM for the shortest wavelength with WGM. Therefore, some important physical mechanisms that have not been revealed (probably surface roughness enhanced surface plasmon resonance, nonlocal effects, or quantum effects) are expected to be involved in the ultra-high resolution imaging in literature.

7.2 Recommendations for future work

In this thesis, various optical imaging modalities are investigated to enhance optical sectioning, scattering rejection and noise elimination to improve resolution. The efforts are extensive but not exhaustive. Except for applications of these microscopic imaging techniques, some recommendations for future work are as follows.

In FMM, the imaging depth can be improved by increasing the modulation depth. However, currently the relationship of imaging depth and modulation depth is qualitative rather than quantitative. The effects of multiple scattering on the imaging depth for apertures with the same value of modulation depth but different geometric configurations are possibly different, especially if the polarization of illumination is under consideration. Thus, a model directly including multiple scattering, aperture configuration and light polarization, will be helpful to quantitatively evaluate the effect of modulation depth on the imaging depth.

A proper apodization can improve the modulation depth and resolution at the same time, but light efficiency, e.g. power efficiency and intensity efficiency, is sacrificed. The decreased power efficiency will degrade the signal level for a given power of illumination. As the intensity efficiency decreases, the possibility of photobleaching in the out-of-focus region will increase. So it is important to find a balance between these advantages and disadvantages. Experimental study on apodization in FMM is expected to identify the optimal apodization for specific kinds of samples.

In current FMM, subtraction of two PSFs is adopted to obtain the effective PSF, where the main objective is to reject multiple scattering background and thus improve imaging depth. On the other hand, the resolution can be improved by subtraction of two PSFs in focal modulation technique. Therefore, it would be of interest to explore manipulation of more than two PSFs to improve the penetration depth and resolution of FMM simultaneously but without sacrificing of light efficiency.

In current diverse imaging, multiple scattering background is not considered in the image formation model (Eq. (4-1)). A high-pass filter may be employed in the objective function (Eq. (4-2)) to eliminate the influence of multiple scattering, since the photon contribution of multiple scattering is usually considered as exhibiting only low frequency components. This is also applicable to diverse imaging by combining FMM and wide-field microscopy, where a high-pass filter is applied to the wide-field image.

In current study, the weight factors for different images are chosen as unity in diverse imaging, which is tunable by considering confidence of image acquisition process, e.g. SNR. Nevertheless, different choices of weight factors will result in emphasis on different information of the reconstructed image. Possibly the effects are different for different diverse modalities and regularizations. An investigation of the effects of weight factors in various diverse modalities is an interesting direction for future work.

The undersampling ratio and cut-off ratio in Fourier hybrid imaging were optimized by simulations in our study. The optimal values may be affected by specific properties of the sample, for example, feature size and concentration. A statistical model would be a good guidance for the parameter choice and experimental exploration for some specific types of samples.

Our simulation results show limited resolution for a micro-lens in wide-field imaging. A confocal mode would be applied to improve its resolution and suppress the significant side-lobes. As a special case of pupil engineering, super-resolution induced by super-oscillation may be achieved by a well-designed wavefront of illumination employed in a micro-lens. Furthermore, other polarizations, e.g. radial polarization and azimuthal polarization, may introduce more benefits in resolution improvement.

Bibliography

1. C. J. Sheppard, "Scanning confocal microscopy," Encyclopedia of Optical Engineering, 22-41 (2003).
2. D. A. Agard, Y. Hiraoka, P. Shaw, and J. W. Sedat, "Fluorescence Microscopy in Three Dimensions," in *Methods in Cell Biology*, D. L. Taylor, and W. Yu-Li, eds. (Academic Press, 1989), pp. 353-377.
3. J. Bewersdorf, R. Pick, and S. W. Hell, "Multifocal multiphoton microscopy," Opt. Lett. **23**, 655-657 (1998).
4. F. Helmchen, and W. Denk, "Deep tissue two-photon microscopy," Nat Meth **2**, 932-940 (2005).
5. A. Aguirre, P. Hsiung, T. Ko, I. Hartl, and J. Fujimoto, "High-resolution optical coherence microscopy for high-speed in vivo cellular imaging," Opt. Lett. **28**, 2064-2066 (2003).
6. J. Huisken, J. Swoger, F. Del Bene, J. Wittbrodt, and E. H. Stelzer, "Optical sectioning deep inside live embryos by selective plane illumination microscopy," Science **305**, 1007-1009 (2004).
7. P. J. Keller, A. D. Schmidt, J. Wittbrodt, and E. H. K. Stelzer, "Reconstruction of Zebrafish Early Embryonic Development by Scanned Light Sheet Microscopy," Science **322**, 1065-1069 (2008).
8. M. G. Gustafsson, "Surpassing the lateral resolution limit by a factor of two using structured illumination microscopy," Journal of microscopy **198**, 82-87 (2000).
9. M. G. L. Gustafsson, L. Shao, P. M. Carlton, C. J. R. Wang, I. N. Golubovskaya, W. Z. Cande, D. A. Agard, and J. W. Sedat, "Three-Dimensional Resolution Doubling in Wide-Field Fluorescence Microscopy by Structured Illumination," Biophysical Journal **94**, 4957-4970 (2008).
10. S. W. Hell, and J. Wichmann, "Breaking the diffraction resolution limit by stimulated emission: stimulated-emission-depletion fluorescence microscopy," Opt. Lett. **19**, 780-782 (1994).
11. V. Westphal, S. O. Rizzoli, M. A. Lauterbach, D. Kamin, R. Jahn, and S. W. Hell, "Video-Rate Far-Field Optical Nanoscopy Dissects Synaptic Vesicle Movement," Science **320**, 246-249 (2008).
12. H. Wang, C. J. R. Sheppard, K. Ravi, S. T. Ho, and G. Vienne, "Fighting against diffraction: apodization and near field diffraction structures," Laser & Photon. Rev. **6**, 354-392 (2012).
13. M. J. Rust, M. Bates, and X. Zhuang, "Sub-diffraction-limit imaging by stochastic optical reconstruction microscopy (STORM)," Nat Meth **3**, 793-796 (2006).
14. E. Betzig, G. H. Patterson, R. Sougrat, O. W. Lindwasser, S. Olenych, J. S. Bonifacino, M. W. Davidson, J. Lippincott-Schwartz, and H. F. Hess, "Imaging Intracellular Fluorescent Proteins at Nanometer Resolution," Science **313**, 1642-1645 (2006).
15. J. B. Sibarita, "Deconvolution microscopy," Advances in biochemical engineering/biotechnology **95**, 201-243 (2005).

16. X. Deng, and M. Gu, "Penetration depth of single-, two-, and three-photon fluorescence microscopic imaging through human cortex structures: Monte Carlo simulation," Appl. Opt. **42**, 3321-3329 (2003).
17. J. M. Murray, P. L. Appleton, J. R. Swedlow, and J. C. Waters, "Evaluating performance in three-dimensional fluorescence microscopy," Journal of microscopy **228**, 390-405 (2007).
18. M. Kempe, W. Rudolph, and E. Welsch, "Comparative study of confocal and heterodyne microscopy for imaging through scattering media," JOSA A **13**, 46-52 (1996).
19. N. Chen, C.-H. Wong, and C. J. Sheppard, "Focal modulation microscopy," Opt. Express **16**, 18764-18769 (2008).
20. N. Chen, and G. Gao, "Multi-contrast focal modulation microscopy for in vivo imaging of thick biological tissues," Opt. Express **20**, 12166-12170 (2012).
21. J. Mertz, and J. Kim, "Scanning light-sheet microscopy in the whole mouse brain with HiLo background rejection," Journal of Biomedical Optics **15**, 016027 (2010).
22. G. Barbastathis, "Diverse imaging with sparsity priors," in *Focus on Microscopy, FOM* (Sydney, Australia, 2014).
23. R. G. Baraniuk, "Compressive sensing," IEEE signal processing magazine **24** (2007).
24. U. Pietrzyk, K. Herholz, A. Schuster, H.-M. v. Stockhausen, H. Lucht, and W.-D. Heiss, "Clinical applications of registration and fusion of multimodality brain images from PET, SPECT, CT, and MRI," European Journal of Radiology **21**, 174-182 (1995).
25. R. J. Hicks, E. W. Lau, and D. S. Binns, "Hybrid imaging is the future of molecular imaging," Biomed Imaging Interv J **3**, e49 (2007).
26. L. W. Dobrucki, and A. J. Sinusas, "PET and SPECT in cardiovascular molecular imaging," Nat Rev Cardiol **7**, 38-47 (2010).
27. G. Cox, and C. J. Sheppard, "Practical limits of resolution in confocal and non‐linear microscopy," Microscopy research and technique **63**, 18-22 (2004).
28. W. Denk, J. Strickler, and W. Webb, "Two-photon laser scanning fluorescence microscopy," Science **248**, 73-76 (1990).
29. C. Xu, W. Zipfel, J. B. Shear, R. M. Williams, and W. W. Webb, "Multiphoton fluorescence excitation: new spectral windows for biological nonlinear microscopy," Proceedings of the National Academy of Sciences **93**, 10763-10768 (1996).
30. M. Gu, and C. Sheppard, "Comparison of three‐dimensional imaging properties between two‐photon and single‐photon fluorescence microscopy," Journal of microscopy **177**, 128-137 (1995).
31. C. J. R. Sheppard, and R. Kompfner, "Resonant scanning optical microscope," Appl. Opt. **17**, 2879-2882 (1978).
32. M. G. Gustafsson, "Extended resolution fluorescence microscopy," Current opinion in structural biology **9**, 627-628 (1999).
33. B.-J. Chang, L.-J. Chou, Y.-C. Chang, and S.-Y. Chiang, "Isotropic image in structured illumination microscopy patterned with a spatial light modulator," Opt.

Express **17**, 14710-14721 (2009).

34. R. Heintzmann, and M. G. L. Gustafsson, "Subdiffraction resolution in continuous samples," Nat Photon **3**, 362-364 (2009).
35. S. Abrahamsson, J. Chen, B. Hajj, S. Stallinga, A. Y. Katsov, J. Wisniewski, G. Mizuguchi, P. Soule, F. Mueller, C. D. Darzacq, X. Darzacq, C. Wu, C. I. Bargmann, D. A. Agard, M. Dahan, and M. G. L. Gustafsson, "Fast multicolor 3D imaging using aberration-corrected multifocus microscopy," Nat Meth **10**, 60-63 (2013).
36. D. Karadaglić, and T. Wilson, "Image formation in structured illumination wide-field fluorescence microscopy," Micron **39**, 808-818 (2008).
37. T. Wilson, "Optical sectioning in fluorescence microscopy," Journal of microscopy **242**, 111-116 (2011).
38. J. Mertz, "Optical sectioning microscopy with planar or structured illumination," Nat Meth **8**, 811-819 (2011).
39. D. Lim, K. K. Chu, and J. Mertz, "Wide-field fluorescence sectioning with hybrid speckle and uniform-illumination microscopy," Opt. Lett. **33**, 1819-1821 (2008).
40. D. Lim, T. N. Ford, K. K. Chu, and J. Mertz, "Optically sectioned in vivo imaging with speckle illumination HiLo microscopy," Journal of Biomedical Optics **16**, 016014-016014-016018 (2011).
41. S. Santos, K. K. Chu, D. Lim, N. Bozinovic, T. N. Ford, C. Hourtoule, A. C. Bartoo, S. K. Singh, and J. Mertz, "Optically sectioned fluorescence endomicroscopy with hybrid-illumination imaging through a flexible fiber bundle," Journal of Biomedical Optics **14**, 030502-030502-030503 (2009).
42. D. Bhattacharya, V. R. Singh, C. Zhi, P. T. C. So, P. Matsudaira, and G. Barbastathis, "Three dimensional HiLo-based structured illumination for a digital scanned laser sheet microscopy (DSLM) in thick tissue imaging," Opt. Express **20**, 27337-27347 (2012).
43. R. A. Zsigmondy, "Properties of colloids," Nobel lecture (1926).
44. C. J. Sheppard, W. Gong, and K. Si, "The divided aperture technique for microscopy through scattering media," Opt. Express **16**, 17031-17038 (2008).
45. D. Maurice, "Cellular membrane activity in the corneal endothelium of the intact eye," Cellular and Molecular Life Sciences **24**, 1094-1095 (1968).
46. M. Gu, C. Sheppard, and H. Zhou, "Optimization of axial resolution in confocal imaging using annular pupils," Optik **93**, 87-90 (1993).
47. X. Gan, S. Schilders, and M. Gu, "Combination of annular aperture and polarization gating methods for efficient microscopic imaging through a turbid medium: theoretical analysis," Microscopy and Microanalysis **3**, 495-503 (1997).
48. B. R. Masters, and A. A. Thaer, "Real-time scanning slit confocal microscopy of the in vivo human cornea," Appl. Opt. **33**, 695-701 (1994).
49. T. D. Wang, M. J. Mandella, C. H. Contag, and G. S. Kino, "Dual-axis confocal microscope for high-resolution in vivo imaging," Opt. Lett. **28**, 414-416 (2003).
50. H. Ra, W. Piyawattanametha, M. J. Mandella, P.-L. Hsiung, J. Hardy, T. D. Wang, C. H. Contag, G. S. Kino, and O. Solgaard, "Three-dimensional in vivo imaging by a handheld dual-axes confocal microscope," Opt. Express **16**, 7224-7232 (2008).

51. L. K. Wong, M. J. Mandella, G. S. Kino, and T. D. Wang, "Improved rejection of multiply scattered photons in confocal microscopy using dual-axes architecture," Opt. Lett. **32**, 1674-1676 (2007).

52. G. T. Di Francia, "Super-gain antennas and optical resolving power," Il Nuovo Cimento (1943-1954) **9**, 426-438 (1952).

53. A. Kempf, "Black holes, bandwidths and Beethoven," Journal of Mathematical Physics **41**, 2360-2374 (2000).

54. M. V. Berry, and S. Popescu, "Evolution of quantum superoscillations and optical superresolution without evanescent waves," Journal of Physics A: Mathematical and General **39**, 6965 (2006).

55. C. Sheppard, and Z. Hegedus, "Axial behavior of pupil-plane filters," J. Opt. Soc. Am. A **5**, 643-647 (1988).

56. C. J. R. Sheppard, and E. Yew, "Performance parameters for focusing of radial polarization," Opt. Lett. **33**, 497-499 (2008).

57. C. J. R. Sheppard, J. Campos, J. C. Escalera, and S. Ledesma, "Three-zone pupil filters," Opt. Commun. **281**, 3623-3630 (2008).

58. C. J. R. Sheppard, and A. Choudhury, "Annular pupils, radial polarization, and superresolution," Appl. Opt. **43**, 4322-4327 (2004).

59. C. J. R. Sheppard, and M. Martinez-Corral, "Filter performance parameters for vectorial high-aperture wave fields," Opt. Lett. **33**, 476-478 (2008).

60. D. M. de Juana, J. E. Oti, V. F. Canales, and M. P. Cagigal, "Design of superresolving continuous phase filters," Opt. Lett. **28**, 607-609 (2003).

61. S. Zhou, and C. Zhou, "Discrete continuous-phase superresolving filters," Opt. Lett. **29**, 2746-2748 (2004).

62. H. Ding, Q. Li, and W. Zou, "Design and comparison of amplitude-type and phase-only transverse super-resolving pupil filters," Optics communications **229**, 117-122 (2004).

63. M. Yun, L. Liu, J. Sun, and D. a. Liu, "Three-dimensional superresolution by three-zone complex pupil filters," J. Opt. Soc. Am. A **22**, 272-277 (2005).

64. S. Ledesma, J. C. Escalera, J. Campos, and M. J. Yzuel, "Evolution of the transverse response of an optical system with complex filters," Optics communications **249**, 183-192 (2005).

65. S. Quabis, R. Dorn, M. Eberler, O. Glöckl, and G. Leuchs, "Focusing light to a tighter spot," Optics communications **179**, 1-7 (2000).

66. R. Dorn, S. Quabis, and G. Leuchs, "Sharper focus for a radially polarized light beam," Physical review letters **91**, 233901 (2003).

67. X. Hao, C. Kuang, T. Wang, and X. Liu, "Phase encoding for sharper focus of the azimuthally polarized beam," Opt. Lett. **35**, 3928-3930 (2010).

68. J. Baumgartl, S. Kosmeier, M. Mazilu, E. T. F. Rogers, N. I. Zheludev, and K. Dholakia, "Far field subwavelength focusing using optical eigenmodes," Applied Physics Letters **98**, - (2011).

69. F. M. Huang, N. Zheludev, Y. Chen, and F. Javier Garcia de Abajo, "Focusing of light by a nanohole array," Applied Physics Letters **90**, - (2007).

70. F. M. Huang, and N. I. Zheludev, "Super-resolution without evanescent waves,"

Nano letters **9**, 1249-1254 (2009).

71. E. T. F. Rogers, and N. I. Zheludev, "Optical super-oscillations: sub-wavelength light focusing and super-resolution imaging," Journal of Optics **15**, 094008 (2013).

72. E. T. F. Rogers, J. Lindberg, T. Roy, S. Savo, J. E. Chad, M. R. Dennis, and N. I. Zheludev, "A super-oscillatory lens optical microscope for subwavelength imaging," Nat Mater **11**, 432-435 (2012).

73. H. J. Hyvärinen, S. Rehman, J. Tervo, J. Turunen, and C. J. R. Sheppard, "Limitations of superoscillation filters in microscopy applications," Opt. Lett. (2012).

74. C. J. R. Sheppard, "Binary phase filters with a maximally-flat response," Opt. Lett. **36**, 1386-1388 (2011).

75. C. J. Sheppard, and S. Mehta, "Three-level filter for increased depth of focus and Bessel beam generation," Opt. Express **20**, 27212-27221 (2012).

76. I. Escobar, G. Saavedra Tortosa, M. Martínez Corral, A. Calatayud, and A. I. Doblas Expósito, "Shaded-Mask Filtering for Extended Depth-of-Field Microscopy," Journal of information and communication convergence engineering, 2013, vol. 11, num. 2, p. 139-146 (2013).

77. H. Wang, L. Shi, G. Yuan, X. S. Miao, W. Tan, and T. Chong, "Subwavelength and super-resolution nondiffraction beam," Applied Physics Letters **89**, 171102-171103 (2006).

78. H. Wang, L. Shi, B. Lukyanchuk, C. Sheppard, and C. T. Chong, "Creation of a needle of longitudinally polarized light in vacuum using binary optics," Nat Photon **2**, 501-505 (2008).

79. E. Botcherby, R. Juškaitis, and T. Wilson, "Scanning two photon fluorescence microscopy with extended depth of field," Optics communications **268**, 253-260 (2006).

80. L. Liu, C. Liu, W. C. Howe, C. Sheppard, and N. Chen, "Binary-phase spatial filter for real-time swept-source optical coherence microscopy," Opt. Lett. **32**, 2375-2377 (2007).

81. S. Hewlett, and T. Wilson, "Resolution enhancement in three-dimensional confocal microscopy," Machine vision and applications **4**, 233-242 (1991).

82. A. Leray, K. Lillis, and J. Mertz, "Enhanced Background Rejection in Thick Tissue with Differential-Aberration Two-Photon Microscopy," Biophysical Journal **94**, 1449-1458.

83. A. Leray, and J. Mertz, "Rejection of two-photon fluorescence background in thick tissue bydifferential aberration imaging," Opt. Express **14**, 10565-10573 (2006).

84. K. Isobe, H. Kawano, T. Takeda, A. Suda, A. Kumagai, H. Mizuno, A. Miyawaki, and K. Midorikawa, "Background-free deep imaging by spatial overlap modulation nonlinear optical microscopy," Biomed. Opt. Express **3**, 1594-1608 (2012).

85. K. Isobe, H. Kawano, A. Suda, A. Kumagai, H. Mizuno, A. Miyawaki, and K. Midorikawa, "Spatial Overlap Modulation Nonlinear Optical Microscopy for High-resolution Deep Imaging," in *Novel Techniques in Microscopy*(Optical Society of America, 2013), p. NM4B. 2.

86. W.-C. Kuo, Y.-T. Shih, H.-C. Hsu, Y.-H. Cheng, Y.-H. Liao, and C.-K. Sun, "Virtual spatial overlap modulation microscopy for resolution improvement," Opt. Express **21**, 30007-30018 (2013).

87. S. P. Chong, C. H. Wong, K. F. Wong, C. J. R. Sheppard, and N. Chen, "High-speed focal modulation microscopy using acousto-optical modulators," Biomed. Opt. Express **1**, 1026-1037 (2010).

88. W. Gong, K. Si, N. Chen, and C. J. R. Sheppard, "Focal modulation microscopy with annular apertures: A numerical study," Journal of biophotonics **3**, 476-484 (2010).

89. S. Li, C. Kuang, X. Hao, Y. Wang, J. Ge, and X. Liu, "Enhancing the performance of fluorescence emission difference microscopy using beam modulation," Journal of Optics **15**, 125708-125715 (2013).

90. C. Kuang, S. Li, W. Liu, X. Hao, Z. Gu, Y. Wang, J. Ge, H. Li, and X. Liu, "Breaking the diffraction barrier using fluorescence emission difference microscopy," Scientific reports **3** (2013).

91. D. L. Donoho, "Compressed sensing," Information Theory, IEEE Transactions on **52**, 1289-1306 (2006).

92. M. Lustig, D. Donoho, and J. M. Pauly, "Sparse MRI: The application of compressed sensing for rapid MR imaging," Magnetic Resonance in Medicine **58**, 1182-1195 (2007).

93. R. G. Baraniuk, "Single-pixel imaging via compressive sampling," IEEE Signal Processing Magazine (2008).

94. D. J. Brady, K. Choi, D. L. Marks, R. Horisaki, and S. Lim, "Compressive holography," Opt. Express **17**, 13040-13049 (2009).

95. L. Tian, J. C. Petruccelli, Q. Miao, H. Kudrolli, V. Nagarkar, and G. Barbastathis, "Compressive x-ray phase tomography based on the transport of intensity equation," Opt. Lett. **38**, 3418-3421 (2013).

96. L. Zhu, W. Zhang, D. Elnatan, and B. Huang, "Faster STORM using compressed sensing," Nature methods **9**, 721-723 (2012).

97. E. Vera, P. Meza, and S. Torres, "Total variation approach for adaptive nonuniformity correction in focal-plane arrays," Opt. Lett. **36**, 172-174 (2011).

98. G. Gong, H. Zhang, and M. Yao, "Construction model for total variation regularization parameter," Opt. Express **22**, 10500-10508 (2014).

99. T. F. Chan, and C.-K. Wong, "Total variation blind deconvolution," Image Processing, IEEE Transactions on **7**, 370-375 (1998).

100. M. Laasmaa, M. Vendelin, and P. Peterson, "Application of regularized Richardson–Lucy algorithm for deconvolution of confocal microscopy images," Journal of microscopy **243**, 124-140 (2011).

101. R. N. Zahreddine, and C. Cogswell, "Total Variation Regularized Deconvolution of Extended Depth of Field Microscope Images," in *Imaging and Applied Optics 2014*(Optical Society of America, Seattle, Washington, 2014), p. IW1C.3.

102. M. Arigovindan, J. C. Fung, D. Elnatan, V. Mennella, Y.-H. M. Chan, M. Pollard, E. Branlund, J. W. Sedat, and D. A. Agard, "High-resolution restoration of 3D structures from widefield images with extreme low signal-to-noise-ratio," Proceedings of the National Academy of Sciences **110**, 17344-17349 (2013).

103. W. F. Cheong, S. A. Prahl, and A. J. Welch, "A review of the optical properties of biological tissues," Quantum Electronics, IEEE Journal of **26**, 2166-2185 (1990).

104. P. Theer, M. T. Hasan, and W. Denk, "Two-photon imaging to a depth of 1000 ?m in living brains by use of a Ti:Al2O3 regenerative amplifier," Opt. Lett. **28**, 1022-1024 (2003).

105. S. P. Chong, C. H. Wong, C. J. Sheppard, and N. Chen, "Focal modulation microscopy: a theoretical study," Opt. Lett. **35**, 1804-1806 (2010).

106. K. Si, W. Gong, N. Chen, and C. J. R. Sheppard, "Two-photon focal modulation microscopy in turbid media," Applied Physics Letters **99**, 233702-233702-233703 (2011).

107. W. Gong, K. Si, N. Chen, and C. J. R. Sheppard, "Improved spatial resolution in fluorescence focal modulation microscopy," Opt. Lett. **34**, 3508-3510 (2009).

108. K. Si, W. Gong, N. Chen, and C. J. R. Sheppard, "Enhanced background rejection in thick tissue using focal modulation microscopy with quadrant apertures," Optics Communications **284**, 1475-1480 (2011).

109. G. Gao, S. P. Chong, C. J. R. Sheppard, and N. Chen, "Considerations of aperture configuration in focal modulation microscopy from the standpoint of modulation depth," J. Opt. Soc. Am. A **28**, 496-501 (2011).

110. N. Chen, G. Gao, and S. P. Chong, "Focal Modulation Microscopy: Principle and Techniques," in *Molecular Imaging*, B. Schaller, ed. (InTech, 2012), pp. 145-182.

111. C. H. Wong, S. P. Chong, C. J. R. Sheppard, and N. Chen, "Simple spatial phase modulator for focal modulation microscopy," Appl. Opt. **48**, 3237-3242 (2009).

112. C. R. Sheppard, X. Gan, M. Gu, and M. Roy, "Signal-to-Noise Ratio in Confocal Microscopes," in *Handbook Of Biological Confocal Microscopy*, J. B. Pawley, ed. (Springer US, 2006), pp. 442-452.

113. B. Richards, and E. Wolf, "Electromagnetic Diffraction in Optical Systems. II. Structure of the Image Field in an Aplanatic System," Proc. R. Soc. Lond. A. **253**, 358-379 (1959).

114. C. Sheppard, and T. Wilson, "The image of a single point in microscopes of large numerical aperture," Proc. R. Soc. Lond. A **379**, 145-158 (1982).

115. H. T. M. van der Voort, and G. J. Brakenhoff, "Modelling Of 3-D Confocal Imaging At High Numerical Aperture In Fluorescence," Proc. SPIE 1028, Scanning Imaging **39**, 39-44 (1989).

116. A. Córdova, W. Gautschi, and S. Ruscheweyh, "Vandermonde matrices on the circle: Spectral properties and conditioning," Numer. Math. **57**, 577-591 (1990).

117. R. Kant, "An Analytical Solution of Vector Diffraction for Focusing Optical Systems," Journal of Modern Optics **40**, 337-347 (1993).

118. H. W. Choi, E. Gu, C. Liu, J. M. Girkin, and M. D. Dawson, "Fabrication and evaluation of GaN negative and bifocal microlenses," J. Appl. Phys. **97**, 063101 (2005).

119. X. Tang, R. Lu, J. Liao, H. Li, L. Zhang, and Y. Liu, "Design and simulation for the bifocal microlens in thick film lithography," Proc. SPIE **7657**, 765708-765712 (2010).

120. M. Leutenegger, R. Rao, R. A. Leitgeb, and T. Lasser, "Fast focus field calculations," Opt. Express **14**, 11277-11291 (2006).

121. S. Segawa, Y. Kozawa, and S. Sato, "Demonstration of subtraction imaging in confocal microscopy with vector beams," Opt. Lett. **39**, 4529-4532 (2014).

122. J. Lin, X. C. Yuan, S. S. Kou, C. J. R. Sheppard, O. G. Rodríguez-Herrera, and J. C. Dainty, "Direct calculation of a three-dimensional diffracted field," Opt. Lett. **36**, 1341-1343 (2011).

123. J. Lin, O. G. Rodríguez-Herrera, F. Kenny, D. Lara, and J. C. Dainty, "Fast vectorial calculation of the volumetric focused field distribution by using a three-dimensional Fourier transform," Opt. Express **20**, 1060-1069 (2012).

124. M. T. Caballero, C. Ibanez-Lopez, and M. Martinez-Corral, "Shaded-mask filtering: novel strategy for improvement of resolution in radial-polarization scanning microscopy," Optical Engineering **45**, 098003-098007 (2006).

125. E. Yew, and C. J. R. Sheppard, "Tight focusing of radially polarized Gaussian and Bessel-Gauss beams," Opt. Lett. **32**, 3417-3419 (2007).

126. G. M. Lerman, and U. Levy, "Effect of radial polarization and apodization on spot size under tight focusing conditions," Opt. Express **16**, 4567-4581 (2008).

127. Q. Zhan, "Cylindrical vector beams: from mathematical concepts to applications," Adv. Opt. Photon. **1**, 1-57 (2009).

128. T. R. M. Sales, and G. M. Morris, "Fundamental limits of optical superresolution," Opt. Lett. **22**, 582-584 (1997).

129. M. W. Kowarz, "Energy constraints in optimum apodization problems," Optics communications **110**, 274-278 (1994).

130. D. Brennan, "Linear diversity combining techniques," Proceedings of the IRE **47**, 1075-1102 (1959).

131. S. Alamouti, "A simple transmit diversity technique for wireless communications," Selected Areas in Communications, IEEE Journal on **16**, 1451-1458 (1998).

132. R. B. Ertel, P. Cardieri, K. W. Sowerby, T. S. Rappaport, and J. H. Reed, "Overview of spatial channel models for antenna array communication systems," Personal Communications, IEEE **5**, 10-22 (1998).

133. M. A. Jensen, and J. W. Wallace, "A review of antennas and propagation for MIMO wireless communications," Antennas and Propagation, IEEE Transactions on **52**, 2810-2824 (2004).

134. J. M. Bioucas-Dias, and M. A. Figueiredo, "A new TwIST: two-step iterative shrinkage/thresholding algorithms for image restoration," Image Processing, IEEE Transactions on **16**, 2992-3004 (2007).

135. H. H. Bauschke, R. S. Burachik, P. L. Combettes, V. Elser, D. R. Luke, and H. Wolkowicz, *Fixed-point algorithms for inverse problems in science and engineering* (Springer Science & Business Media, 2011).

136. V. R. Singh, H. Choi, E. Y. S. Yew, D. Bhattacharya, L. Yuan, C. J. R. Sheppard, J. C. Rajapakse, G. Barbastathis, and P. T. C. So, "Improving signal-to-noise ratio of structured light microscopy based on photon reassignment," Biomed. Opt. Express **3**, 206-214 (2012).

137. J. Goodman, *Introduction to Fourier Optics* (Roberts & Company Publishers, 2005).

138. A. Den Dekker, and A. Van den Bos, "Resolution: a survey," J. Opt. Soc. Am. A

14, 547-557 (1997).

139. T. Holmes, D. Biggs, and A. Abu-Tarif, "Blind Deconvolution," in *Handbook Of Biological Confocal Microscopy*, J. B. Pawley, ed. (Springer US, 2006), pp. 468-487.
140. B. M. Hanser, M. G. Gustafsson, D. A. Agard, and J. W. Sedat, "Phase retrieval for high-numerical-aperture optical systems," Opt. Lett. **28**, 801-803 (2003).
141. J. B. Pendry, "Negative Refraction Makes a Perfect Lens," Phys. Rev. Lett. **85**, 3966-3969 (2000).
142. X. Li, Z. Chen, A. Taflove, and V. Backman, "Optical analysis of nanoparticles via enhanced backscattering facilitated by 3-D photonic nanojets," Opt. Express **13**, 526-533 (2005).
143. J. Y. Lee, B. H. Hong, W. Y. Kim, S. K. Min, Y. Kim, M. V. Jouravlev, R. Bose, K. S. Kim, I. C. Hwang, and L. J. Kaufman, "Near-field focusing and magnification through self-assembled nanoscale spherical lenses," Nature **460**, 498-501 (2009).
144. D. R. Mason, M. V. Jouravlev, and K. S. Kim, "Enhanced resolution beyond the Abbe diffraction limit with wavelength-scale solid immersion lenses," Opt. Lett. **35**, 2007-2009 (2010).
145. Z. Wang, W. Guo, L. Li, B. Luk'yanchuk, A. Khan, Z. Liu, Z. Chen, and M. Hong, "Optical virtual imaging at 50 nm lateral resolution with a white-light nanoscope," Nat. Commun. **2**, 218 (2011).
146. W. C. Chew, "Waves and fields in inhomogenous media," Recherche **67**, 02 (1999).
147. A. Heifetz, J. J. Simpson, S. C. Kong, A. Taflove, and V. Backman, "Subdiffraction optical resolution of a gold nanosphere located within the nanojet of a Mie-resonant dielectric microsphere," Opt. Express **15**, 17334-17342 (2007).
148. B. Zhang, and G. Barbastathis, "Dielectric metamaterial magnifier creating a virtual color image with far-field subwavelength information," Opt. Express **18**, 11216-11222 (2010).
149. C. Sheppard, "The use of lenses with annular aperture in scanning optical microscopy," Optik **48**, 329-334 (1977).